Edelman,
Brian S.

Fermilab Library
0 1160 0004262 6

E-8
Cop. 1

RECEIVED
MAR 21 1979
DIRECTORS OFFICE
FERMILAB

Lambda Hyperon Polarization in Lambda-Proton Elastic Scattering in the Range $60 < P_\Lambda < 380$ GeV/c

BRIAN SCOTT EDELMAN

October, 1977

Supported in part by:
National Science Foundation

Department of Physics and Astronomy

RUTGERS
THE STATE UNIVERSITY
OF NEW JERSEY

LIBOFFCE
FERMILAB
THESIS

FERMILAB
LIBRARY

RU-78-118

LAMBDA HYPERON POLARIZATION IN LAMBDA-PROTON ELASTIC SCATTERING IN THE RANGE $60 < p_\Lambda < 380$ GeV/c

By BRIAN SCOTT EDELMAN

A thesis submitted to

The Graduate School

of

Rutgers University

in partial fulfillment of the requirements

for the degree of

Doctor of Philosophy

Written under the direction of

Professor Thomas J. Devlin

of the Department of Physics

and approved by

Allen B. Robbins

C. Lovelace

Richard J. Plano

Thomas J. Devlin

New Brunswick, New Jersey

October, 1977

FERMILAB
LIBRARY

AAB2014

ABSTRACT OF THE THESIS

LAMBDA HYPERON POLARIZATION

IN LAMBDA-PROTON ELASTIC SCATTERING

IN THE RANGE 60 < p_Λ < 380 GEV/C

By BRIAN SCOTT EDELMAN, Ph.D.

Thesis Director: Professor Thomas J. Devlin

Polarization measurements are a useful indication of the importance of spin dependent forces in an interaction. This thesis presents the first high statistics measurement of the polarization arising from the elastic scattering of two nonidentical baryons. A large data sample consisting of 162,813 Λ-p elastic scatters was analyzed for the polarization of the scattered Λ using the maximum likelihood technique. Data were seen in the momentum interval 60 < p_Λ < 380 GeV/c and in the t interval 0.03 < $|t|$ < 1.4 $(GeV/c)^2$. At 100 GeV/c the data showed a polarization of -0.14 ± 0.04 in the t interval 0.1 < $|t|$ < 0.4 $(GeV/c)^2$. The polarization decreased with increasing Λ momentum to -0.08 ± 0.03 at 140 GeV/c, -0.004 ± 0.021 at 180 GeV/c, -0.022 ± 0.018 at 230 GeV/c, and $+0.010 \pm 0.028$ at 320 GeV/c. A sample of 1367 $\bar{\Lambda}$-p elastic scatters was also seen. The observed $\bar{\Lambda}$ polarizations were $+0.20 \pm 0.14$ at 95 GeV/c and -0.08 ± 0.14 at 145 GeV/c.

GENERAL OUTLINE

Chapter 1	Introduction	1
Chapter 2	Theoretical and Experimental Background	3
Chapter 3	Experimental Techniques	42
Chapter 4	Data Analysis	61
Chapter 5	Results	83
Chapter 6	Conclusions	105
Appendix A	Reasons for Event Rejection	112
Appendix B	The Maximum Likelihood Method	117
Appendix C	The Minimum Chi-Squared Method	120
Footnotes and References		124

TABLE OF CONTENTS

1. Introduction 1

2. Theoretical and Experimental Background 3

2.1 Notation 4

2.2 Dynamical Origins of Polarization 9

2.3 Model Independent Theory 13

2.3.1 The Wolfenstein Formalism 13

2.3.2 The Helicity Amplitudes 18

2.3.3 Transversity Amplitudes 23

2.4 Theoretical Models 31

2.5 Experimental Determination of the Scattering Amplitudes 34

2.6 Experimental Background 36

3. Experimental Techniques 42

3.1 Proton Beam and Collimator 43

3.2 Neutral Beam Intensity Monitors 46

3.3 The Liquid Hydrogen Target System 47

3.4 The Pair Spectrometer 50

3.5 Recoil Proton Detector 53

3.6 Trigger Electronics 55

3.7 On-Line Program 57

3.8 Normal Running Conditions 58

4. Data Analysis 61

4.1 The Track Reconstruction Program 62

4.2 The Elastic Scattering Reconstruction Program 63

4.3 The Polarization Program 68

4.4 Bias Checks 72

5. Results 83

5.1 The Elastic Scattering Polarizations 83

5.2 Corrections to the Data 101

5.3 Bias Checks 102

6. Conclusions 105

Appendix A. Reasons for Event Rejection 112

A.1 Rejection by the Track Reconstruction Program 112

A.2 Rejection by the Elastic Scattering Program 114

A.3 Rejection by the Polarization Program 115

Appendix B. The Maximum Likelihood Method 117

Appendix C. The Minimum Chi-Squared Method 120

Footnotes and References 124

LIST OF TABLES

2.1 Notation 6

2.2 Allowed Exchanges for the Reaction $\Lambda + p \rightarrow \Lambda + p$ 6

3.1 Active Areas of the MWPC's 51

3.2 Composition of the Neutral Beam 51

3.3 Composition of a Typical Data Tape 60

4.1 Classification of Hit Topologies in the Recoil Arms 64

4.2 Monte Carlo Events Fed Directly into the Polarization Program 64

4.3 Monte Carlo Events Filtered through the Track Reconstruction Program 77

4.4 Monte Carlo Events with Track Separation Cut (p_Λ >120 GeV/c) 78

4.5 Monte Carlo Events with Track Separation Cut (p_Λ <160 GeV/c) 78

5.1 Binning Used for Elastic Scattering Data 84

5.2 Parity Allowed Polarizations for $0.1 < |t| < 0.4$ $(GeV/c)^2$ 84

5.3 Λ Polarizations 91

5.4 K_S Polarizations 97

5.5 $\bar{\Lambda}$ Polarizations 100

5.6 Data Comparisons; Bias Checks 100

LIST OF FIGURES

2.1 Illustration of Scattering by an Attractive Force 10

2.2 Positivity Restrictions on b(0), e(0) 17

2.3 Conventional Choices for Helicity Axes 19

2.4 Simple Regge Pole Exchange 32

2.5 Pi^-p, $p^{\pm}p$, and K^-p Recoil Proton Polarizations at 40 GeV/c 39

2.6 Polarization Predictions at s = 200 $(GeV/c)^2$ and s = 2800 $(GeV/c)^2$ from Ref. [32] 41

3.1 Plan View of Detection Apparatus 44

3.2 Plan View of Recoil Proton Detectors 48

3.3 Elevation View of Recoil Proton Detectors 49

4.1 a.) R^2 at the production target 66

b.) Distance of Closest Approach 66

4.2 a.) Pion X-position at C12 73

b.) Horizontal Track-seraration at C10 73

c.) Cos θ^* Distribution for Λ-p Events 73

4.3 Beam Lambda Polarizations with respect to the z-axis 80

4.4 a.) Beam Lambda Polarizations with respect to the x-axis 81

b.) Beam Lambda Polarizations with respect to the y-axis 81

5.1 Λ-p Polarizations (Parity Allowed Component) 85

5.2 Λ-p Polarizations (Parity Violating Component) 89

5.3 Λ-p Polarizations (Parity Violating Component) 90

5.4 Λ-p Elastic Scattering - t 93

5.5 Λ-p Elastic Scattering - p_{Λ} 93

5.6 Λ-p Elastic Scattering - p_{proton} 93

5.7 Λ-p Elastic Scattering - pπ Inv. Mass 93

5.8 K_sp "Polarizations" 94

5.9 K_sp Elastic Scattering - t 96

5.10 K_sp Elastic Scattering - p_{K_s} 96

5.11 K_sp Elastic Scattering - p_{proton} 96

5.12 K_sp Elastic Scattering - $\pi\pi$ Inv. Mass 96

5.13 $\bar{\Lambda}$ Polarizations 98

5.14 $\bar{\Lambda}$-p Elastic scattering - t 99

5.15 $\bar{\Lambda}$-p Elastic Scattering - $p_{\bar{\Lambda}}$ 99

5.16 $\bar{\Lambda}$-p Elastic Scattering - p_{proton} 99

5.17 $\bar{\Lambda}$-p Elastic Scattering - pπ Inv. Mass 99

6.1 pp Elastic Scattering Polarizations 108

6.2 Inclusive Lambda Polarizations 110

CHAPTER 1

INTRODUCTION

Current knowledge of the baryon-baryon interactions is derived primarily from nucleon-nucleon interactions because of the difficulty in obtaining hyperon beams. Interactions involving hyperons are of interest in completing the description of baryon forces, and in testing various symmetry schemes. The new generation of higher energy particle accelerators has made possible for the first time the construction of beams of hyperons.

Beams of hyperons with lifetimes of the order of 10^{-10} seconds are made possible by the relativistic time dilation which becomes substantial when particle velocities are near the speed of light. For example, a Λ hyperon with a lifetime of 2.6×10^{-10} seconds, a mass of 1.115 GeV, and a laboratory momentum of 200 GeV/c will travel an average distance of 14 meters before decaying.

Hyperon beams which have been constructed at the Centre Europeenne Pour La Recherche Nucleaire (CERN) and at Brookhaven National Laboratory (BNL) have yielded interesting results about various aspects of hyperon-nucleon

interactions. The data presented in this paper was taken at the neutral hyperon facility at the Fermi National Accelerator Laboratory (FNAL). The results which will be presented here include the first high statistics measurement of the lambda polarization arising from lambda-proton elastic scattering, and the first measurement of the antilambda polarization arising from antilambda-proton elastic scattering.

CHAPTER 2

THEORETICAL AND EXPERIMENTAL BACKGROUND

The two-body interaction is one of the most studied topics of high energy theorists and experimentalists, and is the source of much of our understanding of the strong interaction. Although no complete dynamical theory of strong interactions exists, the quantum mechanical formalism of scattering amplitudes gives a compact, experimentally accessible description of the various observable quantities. Amplitude analysis (whereby the experimenter measures enough parameters in a set of scattering experiments to determine the individual scattering amplitudes) seems to be the most productive avenue for the investigation of these processes. Measurements which are usually necessary for a complete amplitude analysis include differential cross sections (the incoherent sum of the absolute squares of the amplitudes) and various polarization and spin correlation parameters.

This chapter deals with various aspects of amplitude analysis with particular attention to the polarization parameter P in Λ-p elastic scattering. Section 2.1

summarizes the notation which will be used throughout the rest of the paper. Section 2.2 introduces the notion of polarization and describes briefly its dynamical origins. Section 2.3 discusses three common representations of the scattering amplitudes. It also describes what can be learned about the structure of these amplitudes without resorting to specific models of the interaction, and the way that polarization measurements fit into the overall framework of amplitude analysis. Section 2.4 lists several specific models for two body collisions. Section 2.5 describes the measurements necessary to determine the scattering amplitudes experimentally. Section 2.6 outlines previous measurements of cross sections and polarizations in Λ-p elastic scattering, and some related experiments.

2.1 NOTATION

The notation used will be that of the Landolt-Börnstein compilation [1] with some additions. The reaction of interest is the two body scattering process

$$1+2 \longrightarrow 3+4 \qquad (2.1)$$

where particle 1 = particle 3 and particle 2 = particle 4. In the laboratory system the target, particle 2, is at rest; particle 1 will be referred to as the incident (or beam) particle, 3 as the scattered particle, and 4 as the recoil

particle. The notations for various kinematical variables are listed in Table 2.1 [2].

Convenient variables for scattering processes are the s, t, u Lorentz invariant Mandelstam variables, which satisfy the relation

$$s+t+u = \sum_{i=1}^{4} (m_i^2) \qquad (2.2)$$

For elastic scattering

$$p_1^* = p_2^* = p_3^* = p_4^* = p^* \qquad (2.3)$$

and

$$E_1^* = E_3^* \quad ; \quad E_2^* = E_4^* \qquad (2.4)$$

The quantities s, t, and u, are given by the following:

Total c.m. energy squared

$$s = (E_1^* + E_2^*)^2 = m_1^2 + m_2^2 + 2E_1 m_2 \qquad (2.5)$$

Four-momentum transfer between particles 1 and 3

$$t = (P_1 - P_3)^2 = -2 m_2 (E_1 - E_3)$$
$$= -4 (p^*)^2 \sin^2(\theta_3^*/2)$$
$$= -4 p_1^2 \sin^2(\theta_3/2) \qquad (2.6)$$

Four-momentum transfer between particles 1 and 4

$$u = (P_1 - P_4)^2$$
$$=-2(p^*)^2(1+\cos(\theta_3^*)) + (m_1^2 - m_2^2)^2/s \qquad (2.7)$$

Table 2.1

Variables of Particle i [i=1,2,3,4]

	Center of mass system	Laboratory system
3-momentum	p_i^*	p_i
kinetic energy	T_i^*	T_i
total energy	E_i^*	E_i
4-momentum	$P_i^*=(E_i^*,p_i)$	$P_i=(E_i,p_i)$
scattering polar angle	θ_i^*	θ_i
scattering azimuthal angle	ϕ_i^*	ϕ_i
rest mass	m_i	m_i
solid angle	Ω_i^*	Ω_i
velocity/velocity of light	β_i^*	β_i
transverse momentum	p_t^*	p_t

We assume $c=\hbar=1$, thus $p^2=E^2-p^2=m^2$ and $T=E-m$.

Unless otherwise specified, $\theta_1=\theta^*_1=0$, $\theta_2^*=\pi$, and $p_2=0$.

Table 2.2

Allowed Exchanges for the Reaction $\Lambda + p \rightarrow \Lambda + p$

Exchange	Spin[Parity]	Naturality
P	$0^{[+]}$	+1
P'	$0^{[+]}$	+1
ω	$1^{[-]}$	+1
ρ	$1^{[-]}$	+1
A_2	$2^{[+]}$	+1
h	$4^{[+]}$	+1
π	$0^{[-]}$	-1
B	$1^{[+]}$	-1
η	$0^{[-]}$	-1

The following relations are true to a good approximation at high energies:

$$p^* = 1/2\ s^{1/2} \qquad (2.8)$$

$$s = 2\ p_1\ m_2 \qquad (2.9)$$

$$t = -p_t{}^2 \qquad (2.10)$$

$$u = -2\ p_3\ m_2 \qquad (2.11)$$

There are many representations of the scattering amplitudes in the literature and each representation appears with a number of phase conventions. It is necessary to introduce three of these representations in order to describe simply a number of concepts which restrict the form of the scattering amplitudes. The first representation uses axes of spin quantization which are the same for initial and final states. In this representation the scattering amplitudes are formulated in the c.m. system with respect to the three mutually orthogonal unit vectors

$$\hat{l} = (\hat{p}_1{}^* + \hat{p}_3{}^*)/(2\cos(\theta_3{}^*/2)) \qquad (2.12a)$$

$$\hat{m} = (\hat{p}_1{}^* - \hat{p}_3{}^*)/(2\sin(\theta_3{}^*/2)) \qquad (2.12b)$$

$$\hat{n} = (\hat{p}_1{}^* \times \hat{p}_3{}^*)/\sin(\theta_3{}^*) \qquad (2.12c)$$

The scattering amplitude in this representation will be given by $T(s,\hat{p}_1{}^*,\hat{p}_3{}^*,\vec{\sigma}_1,\vec{\sigma}_2)$ where $\vec{\sigma}_1$ and $\vec{\sigma}_2$ are the Pauli spin matrices for particles 1 and 2.

The second representation is known as the s-channel helicity representation. The scattering amplitude will be represented by f in this representation. The spin quantization axes are parallel to $\hat{p}_1{}^*$ for particles 1 and 2 and are parallel to $\hat{p}_3{}^*$ for particles 3 and 4.

The third representation is known as the s-channel transversity representation. In this representation the spin quantization axis is the normal to the scattering plane. Transforming (in the c.m.system) from the helicity representation to the transversity representation involves only a rotation with Euler angles ($\pi/2$, $\pi/2$, $-\pi/2$). In the transversity representation the scattering amplitude will be represented by G.

The incoherent sum of the absolute squares of the scattering amplitudes is equal to the differential cross section in any of the three representations just mentioned. Since the process of interest in this paper is

$$\Lambda + p \longrightarrow \Lambda + p$$

we will restrict our attention in discussions which follow to elastic scattering of particles with spin[parity] given by

$$1/2^{[+]} + 1/2^{[+]} \longrightarrow 1/2^{[+]} + 1/2^{[+]} \qquad (2.13)$$

2.2 DYNAMICAL ORIGINS OF POLARIZATION

If we examine the spin directions of a group of particles with respect to some direction $\hat{a}$ and we find that the distribution of spin directions with respect to $\hat{a}$ is asymmetric, then we say that the group of particles is polarized with respect to $\hat{a}$. Thus polarization P is a statistical property of a group of particles. The value of P can range from -1 to +1, with P = +1 implying that all spins are parallel to $\hat{a}$, P = Ø implying a completely symmetric distribution of the spins relative to $\hat{a}$, and P = -1 implying that all spins are antiparallel to $\hat{a}$.

One property of particles with spin is if we scatter a group of unpolarized (P = Ø) particles from an unpolarized target, then the particles scattering in a given direction can become polarized with respect to the normal to the scattering plane. It is easy to see this from a consideration of central forces and spin orbit forces in a simple, semiclassical model [17].

Consider a spin one-half particle whose spin is directed out of the paper in Figure 2.1 and scatter it from a very massive spinless particle which is at rest. The potential for this scattering process can be expressed in the following form:

$$v = v_c(r) + v_s(r) \vec{\sigma} \cdot \vec{L} \qquad (2.14)$$

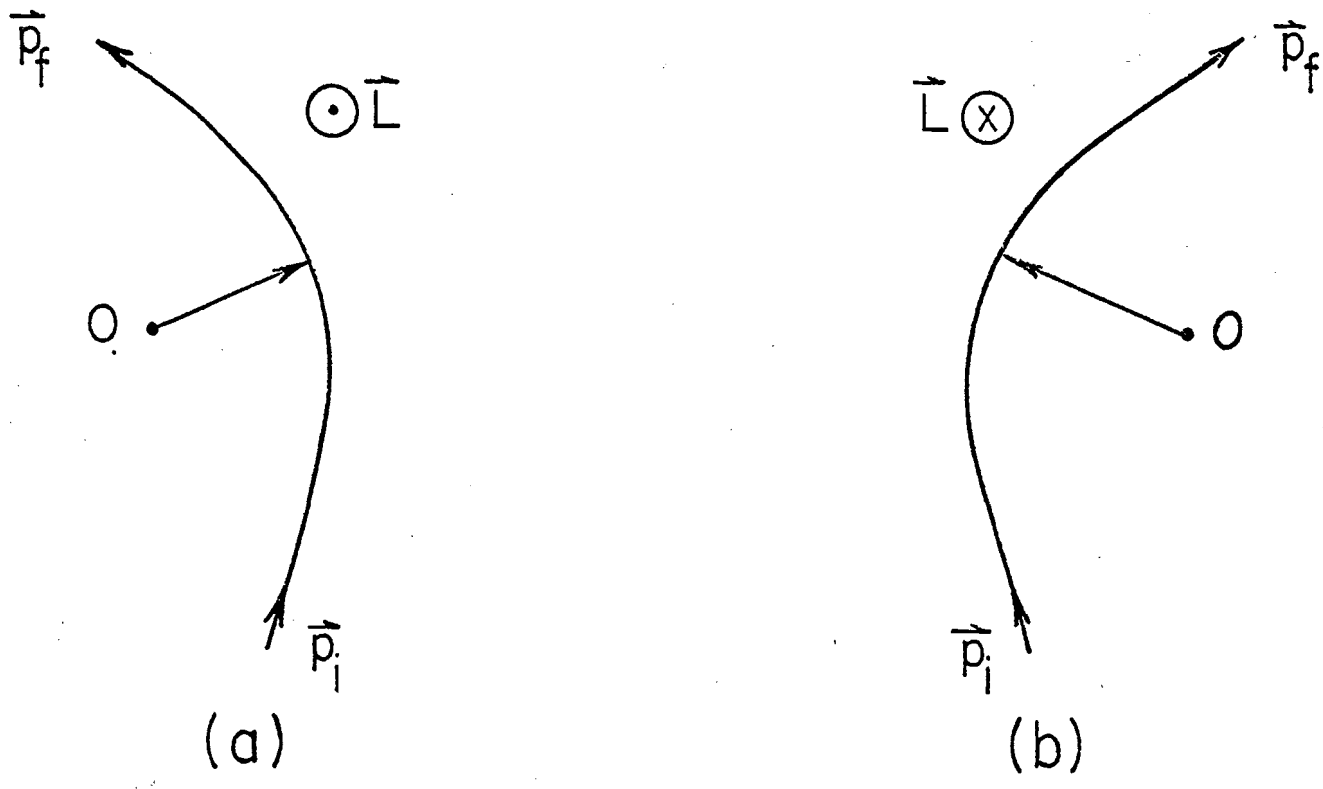

Fig. 2.1

where $v_c(r)$ and $v_s(r)$ are, respectively, the "central potential" and the "spin orbit potential", $\vec{\sigma}$ is the Pauli spin operator and $\vec{L}$ is the orbital angular momentum operator.

Suppose that v_c and v_s are both negative, but that

$$|v_c| >> |v_s| \qquad (2.15)$$

so that the total potential is always attractive. The lighter particle with spin out of the paper (let this represent $s_z = +1/2$) will be deflected toward the point O. Thus, if it passes to the right of O, it will be deflected to the left [Figure 2.1a], and both v_c and v_s will be attractive. If it passes to the left of O, it will be deflected to the right, but v_s will be repulsive, thus reducing the overall attractive force [Figure 2.1b]. Thus the interaction is stronger for particles deflected to the left than for those deflected to the right, and for random impact parameters there will be a net tendency for a beam of particles with $s_z = +1/2$ to scatter to the left. On the other hand, there will be a net tendency for a beam of particles with $s_z = -1/2$ to scatter to the right.

For an experiment conducted with an unpolarized incident beam this asymmetry is just cancelled. However if we detect only particles scattered to the left, we will find that more have spin $s_z = +1/2$ than have spin $s_z = -1/2$ (in

the geometry of Figure 2.1). Thus the detected particles will be polarized with respect to the normal to the scattering plane. We see that measurements of this polarization can provide us with useful information about the nature of spin dependent forces in the interaction process.

Of course, this model is not a complete description of Λ-p elastic scattering because the target is in fact less massive than the incident particle, both the target and beam particles have spin, and we can not expect to be able to define a classical orbit. Useful guidelines do arise from this model, however.

First, we see that the polarization is nonzero only to the extent that the spin-dependent forces are not negligible in comparison to other forces in the interaction. Further, we see that for particles scattered to the right the polarization should be equal and opposite to that for particles scattered to the left. Thus, by defining the normal to the scattering plane as

$$\hat{n} = \hat{p}_1 \times \hat{p}_3/\sin\theta_3^* \qquad (2.16)$$

we would expect to be able to measure the elastic scattering polarization for arbitrary scattering directions in a consistent way.

In addition to these simple results, there are several useful general rules which can result from the scattering of an unpolarized beam on an unpolarized target [17]. These are given below without proof.

1. If there are only s-waves in the initial and final states, there will be no polarization.
2. If a reaction goes through a single intermediate state which has a total angular momentum $J = 0$, there will be no polarization.
3. If the final state is in the $s=0$ singlet state, there will be no polarization.
4. Polarization can result only from interference of different spins or partial waves.
5. Polarization will not occur unless there are noncentral interactions (e,g, spin-dependent forces).
6. If parity is conserved in the interaction, the polarization is always parallel to $\hat{p}_1 \times \hat{p}_3$.

To see how the polarization information fits into a complete description of the scattering process (in terms of its scattering amplitudes) we must learn about the structure of the scattering amplitudes.

2.3 MODEL INDEPENDENT THEORY

2.3.1 The Wolfenstein Formalism

In an elastic collision between two spin 1/2 particles, each initial and final state particle has two possible spin orientations, leading to a total of 16 possible configurations of particle spins. We could thus picture as

many as 16 complex-valued functions being necessary to describe completely the scattering process. Each of these functions can depend upon $\hat{p}_1{}^*$, $\hat{p}_3{}^*$, $\vec{\sigma}_1$, $\vec{\sigma}_2$, and on the energy of the particles. The sum of these 16 functions forms the scattering amplitude $T(\hat{p}_1{}^*,\hat{p}_3{}^*, \vec{\sigma}_1, \vec{\sigma}_2, s)$.

The functional form of $T(\hat{p}_1{}^*,\hat{p}_3{}^*, \vec{\sigma}_1, \vec{\sigma}_2, s)$ is restricted by some very general symmetries. Invariance under spatial rotations implies that T is a scalar function of $\hat{p}_1{}^*$, $\hat{p}_3{}^*$, $\vec{\sigma}_1$, and $\vec{\sigma}_2$. The assumption that the interaction is invariant with respect to space inversion (parity) implies that

$$T(-\hat{p}_1{}^*,-\hat{p}_3{}^*, \vec{\sigma}_1, \vec{\sigma}_2, s) = T(\hat{p}_1{}^*,\hat{p}_3{}^*, \vec{\sigma}_1, \vec{\sigma}_2, s) \qquad (2.17)$$

Invariance with respect to time reversal leads to the condition that

$$T(\hat{p}_1{}^*,\hat{p}_3{}^*, \vec{\sigma}_1, \vec{\sigma}_2, s) = T(-\hat{p}_1{}^*,-\hat{p}_3{}^*,-\vec{\sigma}_1,-\vec{\sigma}_2, s) \qquad (2.18)$$

The most general expression we can write for T, consistent with these conditions is

$$T(\hat{p}_1{}^*,\hat{p}_3{}^*, \vec{\sigma}_1, \vec{\sigma}_2, s) = a + b(\vec{\sigma}_1\cdot\hat{n}\ \vec{\sigma}_2\cdot\hat{n}) + g(\vec{\sigma}_1 + \vec{\sigma}_2)\cdot\hat{n}$$
$$+ g'(\vec{\sigma}_1 - \vec{\sigma}_2)\cdot\hat{n} + d(\vec{\sigma}_1\cdot\hat{m}\ \vec{\sigma}_2\cdot\hat{m}) + e(\vec{\sigma}_1\cdot\hat{l}\ \vec{\sigma}_2\cdot\hat{l})$$
$$(2.19)$$

where $\hat{n}$, $\hat{l}$, and $\hat{m}$ are the unit vectors defined in relations (2.12). We see that T depends on at most six different functions: a,b,g,g',d,e which are functions of p* and $\hat{p}_1^* \cdot \hat{p}_3^* = \cos(\theta_3^*)$ only. In terms of these functions the differential elastic cross section is given by

$$d\sigma/d\Omega^* = |a|^2+|b|^2+|g|^2+|g'|^2+|d|^2+|e|^2 \quad (2.20)$$

This representation of the scattering amplitude is useful for describing some aspects of the scattering process. For instance, in the forward limit ($\theta_3 \longrightarrow 0$) angular momentum conservation implies that [3]

$$g(\theta_3=0) = 0 \qquad (2.21)$$

$$g'(\theta_3=0) = 0 \qquad (2.22)$$

$$b(\theta_3=0) = d(\theta_3=0) \qquad (2.23)$$

so that only three independent contributions to T remain. One of the remaining contributions, a, is independent of the spin configuration of the particles (i.e. it does not appear together with any of the Pauli spin operators).

Comparison of the relative sizes of the contributions to T from the spin independent amplitude a and the spin dependent amplitudes b and e near the forward direction gives a simple measure of the importance of spin dependent forces in the scattering process. This comparison can be

made directly from easily measured quantities and the optical theorem. For instance, the Λ-p total cross section can be estimated by using data on elastic Λ-p scattering, extrapolating to t=0, and using the optical theorem. However, the presence of nonzero contributions from spin dependent amplitudes means that the use of the optical theorem gives only an upper bound for the total cross section. In fact, the total cross section is <u>equal</u> to the value derived from the forward imaginary part of the elastic scattering <u>only</u> if there is no spin dependence (i,e, if b(0)=e(0)=0). Positivity of T places model independent restrictions on each of the nonvanishing amplitudes in the forward direction [4]. In fact, b(0) and e(0) must lie within the shaded region of Figure 2.2 and a(0) must be nonnegative. These conditions are not very restrictive, however, and imply only that [4]

$$\left(\frac{d\sigma}{dt}\bigg|_{t=0}\right)^2 < \pi/4(\sigma_{tot})^2 < 4\left(\frac{d\sigma}{dt}\bigg|_{t=0}\right)^2 \qquad (2.24)$$

where the minimum value of the total cross section corresponds to the point M on the figure.

We would expect the description of the scattering process that is given by those amplitudes which remain finite in the forward limit to be adequate for small values of t. We have seen the amount of information needed to describe the elastic scattering process shrink from the sixteen amplitudes needed for the most general case to six

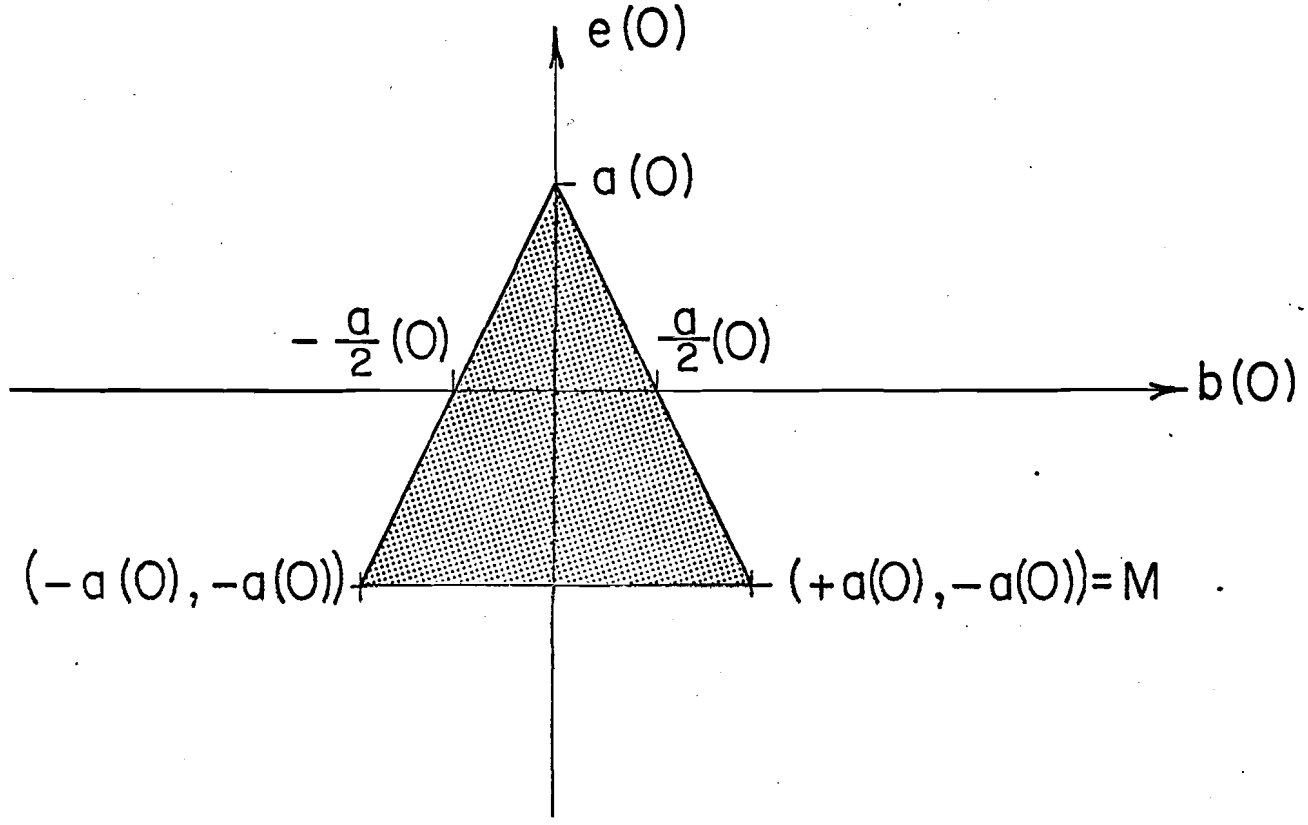

Fig. 2.2

amplitudes for processes which are invariant under spatial rotations, parity reflections, and time reversal, and finally to three amplitudes near the forward direction. This formalism shows clearly the amount of information that is needed to describe the scattering process. It was formulated primarily by Wolfenstein [5],[6] in the 1950's.

Unfortunately this formalism does not show clearly how the amplitudes are related to the various spin states of the interacting particles. We used a fixed axis of quantization (for each event) which was natural for the initial state but quite unnatural for the final state. The formalism is therefore awkward to work with. Furthermore, this formalism separates the angular momentum operator into a spin and an orbital part which leads to complications in the relativistic case [7].

2.3.2 Helicity Amplitudes

These problems can be avoided if we choose the axis for spin quantization in the c.m. to be parallel to the direction of motion of the particles. This means that the spin quantization axis is the same for particles 1 and 2 as in the case just discussed, but it is rotated by the scattering angles θ_3^* and ϕ_3^* for particles 3 and 4 (see Figure 2.3). The component of spin along the direction of motion (called the helicity) is equal to the component of the total angular momentum along the same direction so there

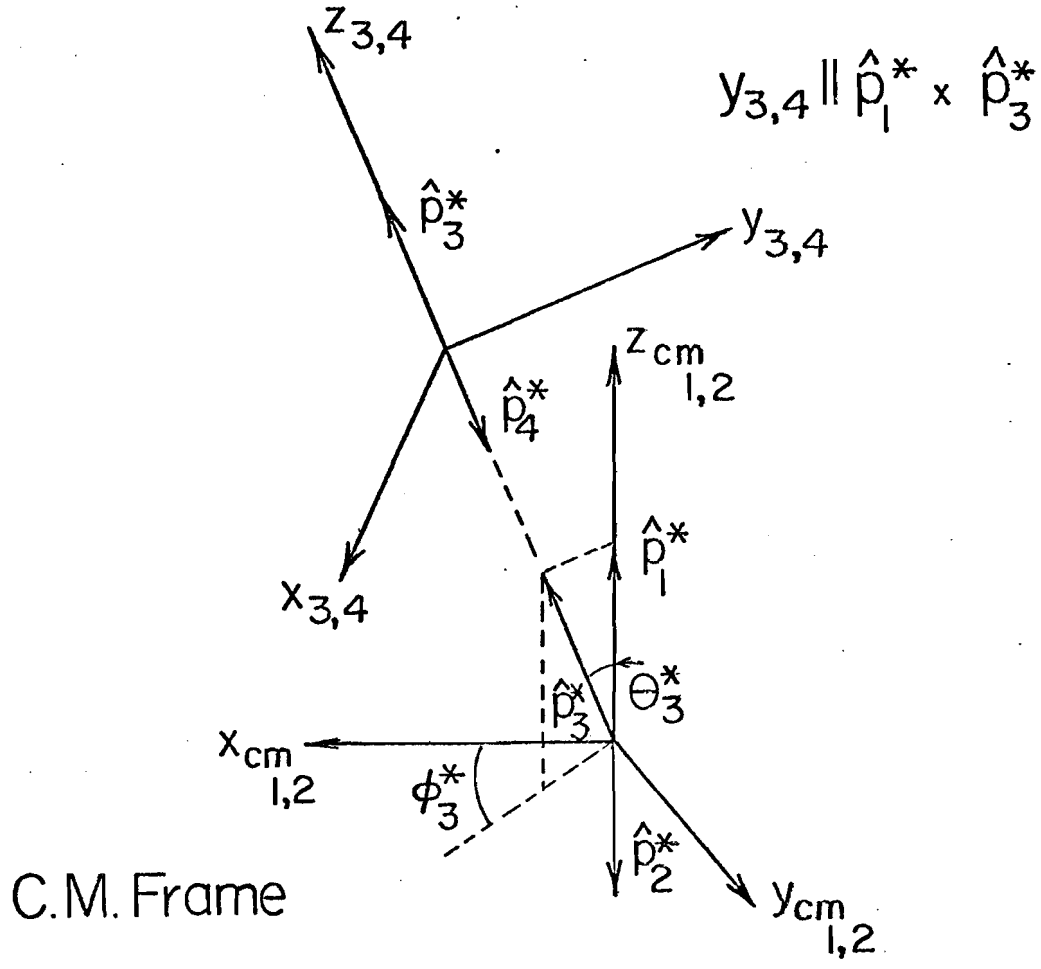
$z_{3,4}$
$y_{3,4} \parallel \hat{p}_1^* \times \hat{p}_3^*$
$\hat{p}_3^*$
$y_{3,4}$
$z_{cm\,1,2}$
$\hat{p}_4^*$
$\hat{p}_1^*$
$x_{3,4}$
$\hat{p}_3^*$
Θ_3^*
$x_{cm\,1,2}$
ϕ_3^*
$\hat{p}_2^*$
C.M. Frame
$y_{cm\,1,2}$

Fig. 2.3

is no separation into spin and orbital parts. The helicity λ of a particle is invariant under ordinary rotations (those involving no spatial reflections) so it is possible to construct states of definite angular momentum J, in which all particles involved have definite helicities. Thus, in describing the reaction

$$1 + 2 \longrightarrow 3 + 4 \qquad (2.25)$$

in the c.m. frame, we may use E*, J, M(=J_z) together with the helicities λ_1, λ_2 as quantum numbers for the initial state, and E*, J, M, λ_3, λ_4 for the final state.

The amplitudes in the helicity representation are defined in terms of the S-matrix elements for transitions from an initial state $\langle i|$ with helicities λ_1, λ_2 to a final state $|f\rangle$ with helicities λ_3, λ_4. The S-matrix element $S_{i,f}$ is just the transition amplitude for some initial configuration of particles in a state $\langle i|$ which ends up as a different configuration of particles in a state $|f\rangle$. The collection of all the matrix elements $S_{i,f}$ yields the S-matrix [16]. Since E*, J, M appear in both initial and final states we may write the S-matrix for the process (2.25) in the form

$$\langle E'J'M'\lambda_3\lambda_4|S|E\ J\ M\ \lambda_1\lambda_2\rangle$$
$$= \delta(E-E')\,\delta_{JJ'}\,\delta_{MM'}\langle\lambda_3\lambda_4|S^J(E)|\lambda_1\lambda_2\rangle \quad (2.26)$$

where $S^J(E)$ is the submatrix of S belonging to definite values of J and E. The helicity has the following convenient properties:

1. It is invariant under ordinary rotations (those involving no spatial reflections).

2. For massive particles λ has $2s + 1$ (s=spin) possible values which are

$$\lambda = -s, -s+1, \ldots, s \qquad (2.27)$$

3. Under parity reflection λ changes sign.

4. The magnitude of λ is invariant under Lorentz transformations parallel to the particle directions of motion.

Defining the T-matrix in the familiar way

$$S - 1 = iT \qquad (2.28)$$

we can write the differential cross section for a particular set of initial and final state helicities as

$$d\sigma/d\Omega = (2\pi/p^*)^2 \, \langle \theta_3^* \phi_3^* \lambda_3 \lambda_4 | T(E) | 00 \lambda_1 \lambda_2 \rangle^2$$
$$\equiv \left| f_{\lambda_3 \lambda_4 ; \lambda_1 \lambda_2}(\theta_3^*, \phi_3) \right|^2 \qquad (2.29)$$

This relation defines the helicity amplitudes $f(\theta_3^*, \phi_3^*)$. The dependence of f upon the scattering angles is given by the partial wave expansion [7]:

$$f_{\lambda_3 \lambda_4 ; \lambda_1 \lambda_2}(\theta_3^*, \phi_3^*) =$$
$$1/p^* \sum_J (J+1/2) \langle \lambda_3 \lambda_4 | T^J(E) | \lambda_1 \lambda_2 \rangle e^{i(\lambda - \mu)\phi_3^*} d^J_{\lambda\mu}(\theta_3^*) \qquad (2.30)$$

where $\lambda = \lambda_1 - \lambda_2$ and $\mu = \lambda_3 - \lambda_4$, and where

$$\langle \lambda_3\lambda_4 | S^J(E) | \lambda_1\lambda_2 \rangle - \delta_{\lambda_1\lambda_3}\delta_{\lambda_2\lambda_4} = i\langle \lambda_3\lambda_4 | T^J(E) | \lambda_1\lambda_2 \rangle \quad (2.31)$$

The $d^J_{\lambda\mu}(\theta)$ are relatively simple functions of the Legendre polynomials and their derivatives [8]. From the above relation we see that

$$f_{\lambda_3\lambda_4;\lambda_1\lambda_2}(\theta_3^*,\phi_3^*)=e^{i(\lambda-\mu)\phi_3^*}f_{\lambda_3\lambda_4;\lambda_1\lambda_2}(\theta_3^*,0) \quad (2.32)$$

so that the ϕ-dependence, while not absent, is trivial.

The consequences of parity and time reversal invariance for

$$1/2^{[+]} + 1/2^{[+]} \longrightarrow 1/2^{[+]} + 1/2^{[+]}$$

elastic scattering can be written as follows [9]:

Parity:

$$f_{\lambda_3\lambda_4;\lambda_1\lambda_2}(\theta_3^*,0)=(-1)^{\lambda-\mu}f_{-\lambda_3-\lambda_4;-\lambda_1-\lambda_2}(\theta_3^*,0) \quad (2.33)$$

Time Reversal:

$$f_{\lambda_3\lambda_4;\lambda_1\lambda_2}(\theta_3,0)=(-1)^{\lambda-\mu}f_{\lambda_1\lambda_2;\lambda_3\lambda_4}(\theta_3^*,0) \quad (2.34)$$

From these conditions we find (as before) that there are six independent amplitudes which are conventionally taken to be:

$$\begin{array}{ll} f_1=f_{++++} & f_4=f_{+--+} \\ f_2=f_{++--} & f_5=f_{+++-} \\ f_3=f_{+-+-} & f_6=f_{++-+} \end{array} \quad (2.35)$$

where (+) and (-) represent helicity values of +1/2 and -1/2. In the forward direction we find that helicity

amplitudes which have a nonzero net helicity flip (given by $\lambda_3-\lambda_4-\lambda_1+\lambda_2$) must vanish. This implies that

$$f_4(\theta_3=0) = f_5(\theta_3=0) = f_6(\theta_3=0) = 0 \quad (2.36)$$

We are left with three nonvanishing amplitudes which are related to the "Wolfenstein" amplitudes a(0), b(0), e(0) by the following [10]:

$$f_1 = a(0) + e(0) \quad (2.37)$$

$$f_2 = b(0) \quad (2.38)$$

$$f_3 = a(0) - e(0) \quad (2.39)$$

All physical observables are bilinear combinations of the individual amplitudes. For instance, in terms of the helicity amplitudes, the differential elastic cross section for

$$\Lambda + p \rightarrow \Lambda + p$$

is given by [13]:

$$d\sigma/dt = |f_1|^2 + |f_2|^2 + |f_3|^2 + |f_4|^2 \; 2|f_5|^2 + 2|f_6|^2 \quad (2.40)$$

and the polarization of the elasticly scattered lambda from an unpolarized target is given by [47]:

$$P\, d\sigma/dt = 2\, \mathrm{Im}[(f_1 + f_3)f_6^* - (f_2 - f_4)f_5^*] \quad (2.41)$$

We see that P vanishes in the forward direction since

$$f_5(0) = f_6(0) = 0.$$

2.3.3 Transversity Amplitudes

One disadvantage of the helicity amplitudes is that they do not represent transitions in states of definite

parity. If we wish to view the scattering process in terms of particle exchange or Reggeon exchange, for example, the helicity amplitudes cannot be related to any single simple exchanged object. Rather, the exchanged object must be represented in terms of a linear combination of several helicity amplitudes. The desirability of using a set of amplitudes similar to the helicity amplitudes, but representing transitions in states of definite parity is one motivation for the usage of another set of spin quantization axes: the transversity axes.

The transversity axes are related to the helicity axes by a rotation with Euler angles ($\pi/2$, $\pi/2$, $-\pi/2$) which means that the two sets of axes are related in the following way:

$$(x,y,z)_{\text{helicity}} \longrightarrow (x,z,-y)_{\text{transversity}} \qquad (2.42)$$

The axis of spin quantization in this representation is the normal to the scattering plane. This makes the transversity amplitudes particularly useful for describing polarizations since the parity-allowed polarizations must be parallel to this axis. The component of a particle's spin along the normal to the scattering plane is called the transversity . The transversity is invariant under reflections in the scattering plane and under Lorentz transformations in the scattering plane, including boosts from the c.m. to the individual particle rest frames (the rest frame of particle 2 being the lab frame). The relation between the transversity amplitudes $G_{\tau_3,\tau_4;\tau_1,\tau_2}$ and the helicity

amplitudes $f_{\lambda_3\lambda_4;\lambda_1\lambda_2}$ is [9],

$$G_{\tau_3\tau_4;\tau_1\tau_2}=\sum_{\lambda}[D^{J_3*}_{\tau_3\lambda_3}(R)D^{J_4*}_{\tau_4\lambda_4}(R)D^{J_1}_{\tau_1\lambda_1}(R)D^{J_2}_{\tau_2\lambda_2}(R)$$

$$(-1)^{J_2-\lambda_2}(-1)^{J_4-\lambda_4}\ f_{\lambda_3\lambda_4;\lambda_1\lambda_2}(\theta,\emptyset)] \quad (2.43)$$

where $R=(\pi/2\ ,\ \pi/2\ ,\ -\pi/2)$ and where

$$D^{J}_{\tau\lambda}(a,b,c)=e^{-ia\tau}d^{J}_{\tau\lambda}(b)e^{-ic\lambda} \quad (2.44)$$

The parity and time reversal restrictions on the transversity amplitudes are as follows:

$$\text{Parity:}G_{\tau_3\tau_4;\tau_1\tau_2}=(-1)^{\tau_1+\tau_2-\tau_3-\tau_4}G_{\tau_3\tau_4;\tau_1\tau_2} \quad (2.45)$$

$$\text{Time Reversal:}G_{\tau_3\tau_4;\tau_1\tau_2}=(-1)^{\tau_1-\tau_2+\tau_4-\tau_3}G_{\tau_1\tau_2;\tau_3\tau_4} \quad (2.46)$$

Note that parity conservation requires transversity amplitudes to vanish unless $(-1)^{\tau_1+\tau_2-\tau_3-\tau_4}=1$. The eight amplitudes remaining after applying the parity conservation constraint are already linearly independent [42]. In contrast, for helicity amplitudes the parity conservation implies some linear relations and all the amplitudes are, in general, different from zero. The time reversal constraints (together with parity conservation) leave six independent amplitudes which can be taken to be

$$G_1 = G_{++++} \qquad G_4 = G_{-+-+}$$
$$G_2 = G_{----} \qquad G_5 = G_{++--}$$
$$G_3 = G_{+-+-} \qquad G_6 = G_{+--+} \quad (2.47)$$

Using relation (2.43) we see that the transversity amplitudes are related to the helicity amplitudes by the following [46]:

$$G_1=1/2[f_1+f_2+f_3-f_4-2i\ f_5+2i\ f_6]$$

$$G_2=1/2[f_1+f_2+f_3-f_4+2i\ f_5-2i\ f_6]$$

$$G_3=1/2[f_1-f_2+f_3+f_4+2i\ f_5+2i\ f_6]$$

$$G_4=1/2[f_1-f_2+f_3+f_4-2i\ f_5-2i\ f_6]$$

$$G_5=1/2[-f_1-f_2+f_3-f_4]$$

$$G_6=1/2[f_1-f_2-f_3-f_4] \quad (2.48)$$

or

$$f_1=1/4(G_1+G_2+G_3+G_4-2G_5+2G_6)$$

$$f_2=1/4(G_1+G_2-G_3-G_4-2G_5-2G_6)$$

$$f_3=1/4(G_1+G_2+G_3+G_4+2G_5-2G_6)$$

$$f_4=1/4(-G_1-G_2+G_3+G_4-2G_5-2G_6)$$

$$f_5=i/4(G_1-G_2-G_3+G_4)$$

$$f_6=i/4(-G_1+G_2-G_3+G_4) \qquad (2.49)$$

In the forward limit relation (2.36) implies linear relations among the transversity amplitudes:

$$\lim_{\theta_3 \to 0} (G_1 - G_2) = 0 \quad (2.50)$$

$$\lim_{\theta_3 \to 0} (G_3 - G_4) = 0 \quad (2.51)$$

$$\lim_{\theta_3 \to 0} (G_1 + G_5 + G_6) = \lim_{\theta_3 \to 0} G_3 \quad (2.52)$$

We are thus left with three independent amplitudes which we may take to be G_1, G_3, and G_5. The relations between these amplitudes and the limiting values of the Wolfenstein amplitudes are:

$$G_1(0) = a(0) + 1/2\ b(0) \quad (2.53)$$

$$G_3(0) = a(0) - 1/2\ b(0) \quad (2.54)$$

$$G_5(0) = -e(0) - 1/2\ b(0) \quad (2.55)$$

If we apply the relations (2.49) to equation (2.41) which defines the polarization in the helicity representation, we see that

$$P \quad d\sigma/dt = 1/2 \mathrm{Re}[(G_1+G_2)(G_1^*-G_2)+(G_3+G_4)(G_3^*-G_4^*)] \quad (2.56)$$

Referring to definitions (2.47) we see that the two contributions to P are

$$1/2\ \mathrm{Re}[(G_{++++} + G_{----})(G_{++++}^* - G_{----}^*)]$$

and

$$1/2\ \mathrm{Re}[(G_{+-+-} + G_{-+-+})(G_{+-+-}^* - G_{-+-+}^*)].$$

These relations show some very interesting aspects of the polarization which do not appear as clearly in any other representation. First it is interesting to note that only amplitudes which show no transversity flip appear in the polarization. In addition, these relations show the amplitude structure of the polarization in a way which is

easy to understand intuitively (i.e. they show explicitly that the polarization arises from a difference in the relative populations of final state spin orientations).

Another convenient property of the transversity amplitudes is that they conserve a quantum number called naturality ξ. The most general definition of the naturality is [11]:

$$\xi \equiv (-1)^{J} \eta \tag{2.57}$$

where η is intrinsic parity (or the product of the individual particle intrinsic parities in a product state). For an elastic lambda —proton scattering transversity amplitude it becomes [12]:

$$\xi = e^{i\pi(\tau_3 - \tau_1)} = (-1)^{\tau_3 - \tau_1 + 1} \tag{2.58}$$

If the parity of the object exchanged in the scattering process is given by $P=(-1)^J$ [$P=(-1)^{(J+1)}$] we say that the object exchanged had natural [unnatural] parity. We see that the naturality associated with a transversity amplitude is +1 for natural parity "exchange" and -1 for unnatural parity "exchange". Thus the transversity amplitudes G_1, G_2, G_3, G_4 are associated with natural parity exchange while G_5 and G_6 are associated with unnatural parity exchange.

A very useful result concerning natural and unnatural parity exchange is derived by Ader et al [12]. It states that in any scattering process with an unpolarized initial state and measurement of only one polarization in the final state, any observable quantity O can be expressed only in terms of incoherent sums over natural or unnatural parity exchange of the type

$$O = [G_i^{[+]} G_j^{[+]*} + G_k^{[-]} G_l^{[-]*}] \quad (2.59)$$

Here the superscript refers to the naturality so that i, j are 1, 2, 3, or 4 and k, l are 5 or 6. In particular, observable quantities are insensitive to the relative phase between opposite naturality contributions. This places restrictions upon the way that observables can be related to the transversity amplitudes. For instance, in the forward limit, observables can be composed of only two types of terms. One type (from amplitudes which represent natural parity exchange) will contain only $G_1G_1^*$, $G_1G_3^*$, $G_3G_1^*$, or $G_3G_3^*$. The other type (from amplitudes which represent unnatural parity exchange) will contain only $G_5G_6^*$, $G_5G_5^*$, $G_6G_6^*$, or $G_6G_5^*$ where $G_6=G_3-G_1-G_5$.

As an example of some of these principles, consider simple Regge exchange. The allowed exchanges for baryon-baryon elastic scattering are given in Table 2.2 along with their values of $\text{spin}^{[\text{parity}]}$ and their naturalities. From this table we can see the restrictions that naturality considerations place on the allowed Regge

exchanges. Expression (2.56) does not depend on the transversity flip amplitudes which are associated with unnatural parity exchange, so we see that the Regge exchanges with naturality (-) can not contribute to the polarization. This eliminates contributions from π , B, and η exchange. The remaining amplitudes G_1, G_2, G_3, G_4 which do appear in the polarization should be dominated by Pomeron exchange. We would expect any polarization of the final state particles to arise from interference of the two lowest lying exchanges with natural parity and different values of J: for Λ-p elastic scattering the Pomeron and the ω .

Another useful feature of the transversity amplitudes is that the crossing relations, which relate the transversity amplitudes for processes in the s, t, or u channels, are relatively simple. If we denote the amplitudes as follows:

$$1 + 2 \longrightarrow 3 + 4 \text{ ; s-channel, amplitude G} \qquad (2.60)$$

$$1 + \bar{3} \longrightarrow \bar{2} + 4 \text{ ; t-channel, amplitude H} \qquad (2.61)$$

$$\bar{3} + 2 \longrightarrow \bar{1} + 4 \text{ ; u-channel, amplitude U} \qquad (2.62)$$

then the crossing relations are [42]

$$G_{\tau_3\tau_4;\tau_1\tau_2} = (-1)^{\tau_2+\tau_3} e^{i(\psi_3\tau_3 - \psi_4\tau_4 + \psi_2\tau_2 - \psi_1\tau_1)} H_{-\tau_2\tau_4;\tau_1 -\tau_3} \qquad (2.63)$$

$$G_{\tau_3\tau_4;\tau_1\tau_2} = (-1)^{\tau_1+\tau_3} e^{i\left(\bar{\varphi}_2\tau_2+\bar{\varphi}_4\tau_4-\bar{\varphi}_1\tau_1-\bar{\varphi}_3\tau_3\right)} U_{-\tau_1\tau_4;-\tau_3\tau_2} \quad (2.64)$$

The angles φ_i and $\bar{\varphi}_i$ are explicitly known functions of the invariants s, t, and u [43]. We see that the crossing matrices have in each row and in each column only one nonzero element. Thus there is no summation in the crossing relations and there is a one-to-one correspondence between spin amplitudes in the direct and crossed channels. This property is extremely convenient for use with models which express physical quantities in terms of the crossed-channel amplitudes.

2.4 THEORETICAL MODELS

The starting point of many model builders is the simple Regge-pole exchange picture, as indicated in Figure 2.4. Although this simple exchange picture is not expected to be exact, it helps to interpret some experimental results. Two general predictions, which should be true when a single Regge-pole dominates, are phase coherence and factorization of amplitudes [9].

Phase coherence implies restrictions on the relative phases of the various scattering amplitudes. In the helicity and "Wolfenstein" representations, the phase coherence implies that the amplitudes are relatively real. In the transversity representation the amplitudes fulfill the relation

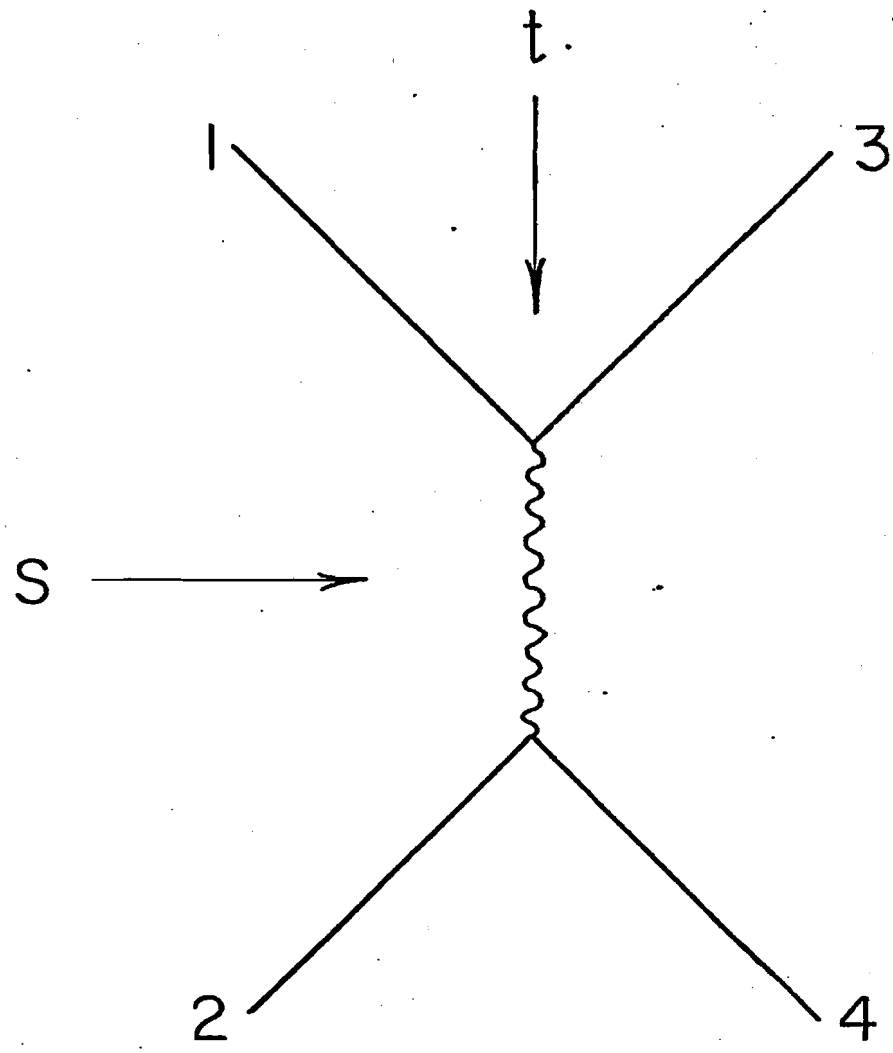

Fig. 2.4.

$$G_{\tau_3\tau_4;\tau_1\tau_2} = (-1)^{\tau_1+\tau_2-\tau_3-\tau_4} G^*_{-\tau_3-\tau_4;-\tau_1-\tau_2} \quad (2.65)$$

if the helicity amplitudes are real (as in the one-particle-exchange models). This relation can be readily generalized for the case when the helicity amplitudes have a common nonzero phase. Phase coherence implies that the trace of any bilinear combination of amplitudes will vanish if an odd number of Pauli spin matrices appears.

Factorization means that the vertex contributions to the scattering amplitude decompose into a simple product with no vertex-vertex coupling terms. This would mean that the only way that information could be transmitted from one vertex to the other would be via a Reggeon propagator term in the amplitude. Hence particle 3 should not be influenced by polarizations of particles 2 and 4. If, in addition to factorization, one allows natural parity exchange only, then there are no spin dependent amplitudes [15]. Thus there could be no polarization of final state particles from an unpolarized initial state.

Violations of these simple predictions provide important information for model builders. Some of the concepts which have been used to explain departures from the simple exchange picture are Regge cuts, multiple exchanges, and absorption. Among the more recent models for two body scattering are the following:

1. Complex Regge Pole Models [22]

2. Dual Absorption Models [20],[21]

3. Effective Absorption Models [39]

4. The Poor Man's Absorption Model [14]

5. The Strong Central Absorption Prescription [33]

The complex Regge pole models allow the existence of Regge cuts and multiple exchanges and try to approximate the observed behavior of the amplitudes with a suitably placed pair of complex conjugate Regge poles. The absorption models alter the form of the scattering amplitudes from those expected in the simple exchange picture by assuming that contributions from scatters with certain impact parameters are suppressed (absorbed). For instance, a peripheral exchange picture could be built up by assuming that small impact parameter contributions to the scattering amplitudes are suppressed. A comparison of the properties of these models and a fairly thorough set of references can be found in a review by Fox and Quigg [14].

2.5 EXPERIMENTAL DETERMINATION OF THE SCATTERING AMPLITUDES

In order to measure all of the independent scattering amplitudes for $\Lambda + p \longrightarrow \Lambda + p$ one would need to perform enough measurements to specify uniquely the real and imaginary

parts of the six independent amplitudes. Since there is an overall phase that can not be determined, eleven measurements are necessary. The presence of six independent amplitudes implies that there are 36 linearly independent observables. It is possible to derive a set of 25 quadratic relations among these observables, however, leaving eleven observables which are independent in the sense that one can not be predicted from the others [38]. Thus, in principle, it is possible to obtain a heavily overdetermined set of measurements.

Among these measurements are (in order of ascending measurement difficulty) the quantities $d\sigma/dt$,P, R, D_1, D_2, K_1, K_2, and C_{nn} [19]. The polarization parameter P is a measure of the asymmetry of the normal spin component of the scattered lambda when both beam and target are unpolarized. Scattering an unpolarized lambda from a polarized target yields two more nonzero polarization parameters, R and A. Only P and R have been included in the preceding list because of the relation

$$P^2 + R^2 + A^2 = 1 \qquad (2.67)$$

The depolarization parameter D_1 [D_2] is a measure of how the normal spin component of particle 1 [particle 2] changes in the scattering process. The spin correlation parameter C_{nn} is a measure of how the cross section depends on the relative orientation of the two initial state particle normal spin components [18]. The polarization transfer parameter K_1 [K_2] is a measure of how much of the

polarization of particle 1 [particle 2] is transferred to particle 4 [particle 3].

Most of the parameters described thus far are quite difficult to measure, since they require a polarized beam, a polarized target, or both. One way to expand the list of measurements from the eight just described to the eleven which are necessary for a complete amplitude analysis is to replace the differential cross section in the list with various differential cross sections where both initial and final states are restricted to definite spin configurations. Much progress has been made in the design of polarized proton targets, and a partially polarized lambda beam is now available [40]. Even so, most of these measurements are so difficult that there is little hope for a complete amplitude analysis in the near future.

2.6 EXPERIMENTAL BACKGROUND

Rather little is known about hyperon-nucleon interactions at high energies, because in the past, hyperons have been difficult to produce in large numbers and they have relatively short lifetimes. Most experimental knowledge about hyperon-nucleon interactions to date is from bubble chamber experiments [23]. Experimental information about the polarization P arising from hyperon-nucleon scattering is almost nonexistant.

The most recently published measurement of the Λ-p total cross section at high energy is that of Gjesdal et al [24] who obtain a value of

$$\sigma_{tot\Lambda p} = 34.6 \pm 0.4 \text{ mb} \qquad (2.68)$$

in the lambda momentum interval 6 - 21 GeV/c. There are three measurements of the Λ-p elastic cross section at about 4 GeV/c [25], [26], [27] which combine to give

$$\sigma_{el} = 12.0 \pm 1.3 \text{ mb} \qquad (2.69)$$

in the momentum interval 2 - 5 GeV/c. Data at momenta lower than 2 GeV/c are tabulated by Alexander et al [28]. Anderson [27] also gives a measurement of the Λ-p elastic cross section in the lambda momentum interval of 6 - 17 GeV/c:

$$\sigma_{el} = 4.1 \pm 1.6 \text{ mb} \qquad (2.70)$$

Polarization data for Λ-p elastic scattering are tabulated for lambda momenta below 1.3 GeV/c by Alexander [28]. The only measurements at higher energies are given by Anderson [27] and are

$$\alpha P = -0.4 \pm 0.2 \qquad (2.71)$$

for lambda momenta less than 5 GeV/c, and

$$\alpha P = -0.2 \pm 0.4 \qquad (2.72)$$

for lambda momenta in the interval 5 - 17 GeV/c. The quantity α in these expressions is a measure of the parity violating asymmetry in hyperon decay. For $\Lambda \rightarrow p + \pi^-$, α is equal to 0.647 $\pm$ 0.013 [29],[48]. Since these polarization data do not tell us very much about what to expect for the polarization, we are forced to turn to other

particle systems for whatever information they might offer.

Although folklore has it that polarization effects die away very rapidly at high energies, elastic scattering polarizations persist in $\pi^{\pm}p$, pp, pp, and $K^{-}p$ elastic scattering at incident momenta as high as 45 GeV/c. The momentum and t dependence for these data are shown in Figure 2.5 [30], [36], [37]. Polarization measurements have not yet been made for energies higher than this except for the pp system [19], [31].

The pp polarization below 50 GeV/c is reproduced remarkably well by a model devised by Pumplin and Kane [32]. Their model asserts that the imaginary part of every elastic scattering amplitude at sufficiently large impact parameter is governed by the two-pion exchange cut in the t-channel. This would mean that the large-impact-parameter tail of the Pomeron is not an SU(3) singlet. The contribution of the tail is calculated to be typically about 1/4 of the total cross section and leads to observable differences between high-energy total cross sections for π-p and K-p, and between pp, Λ-p, Σ-p, and Ξ-p. In addition, the tail contribution gives rise to a substantial polarization in pp elastic scattering which persists up to very high energies. Typical predictions of this model are shown in Figure 2.6 [32]. The model predicts that the polarization in Λ-p elastic scattering will be similar in shape to the pp polarization, but smaller by a factor of 2 or 3. This would

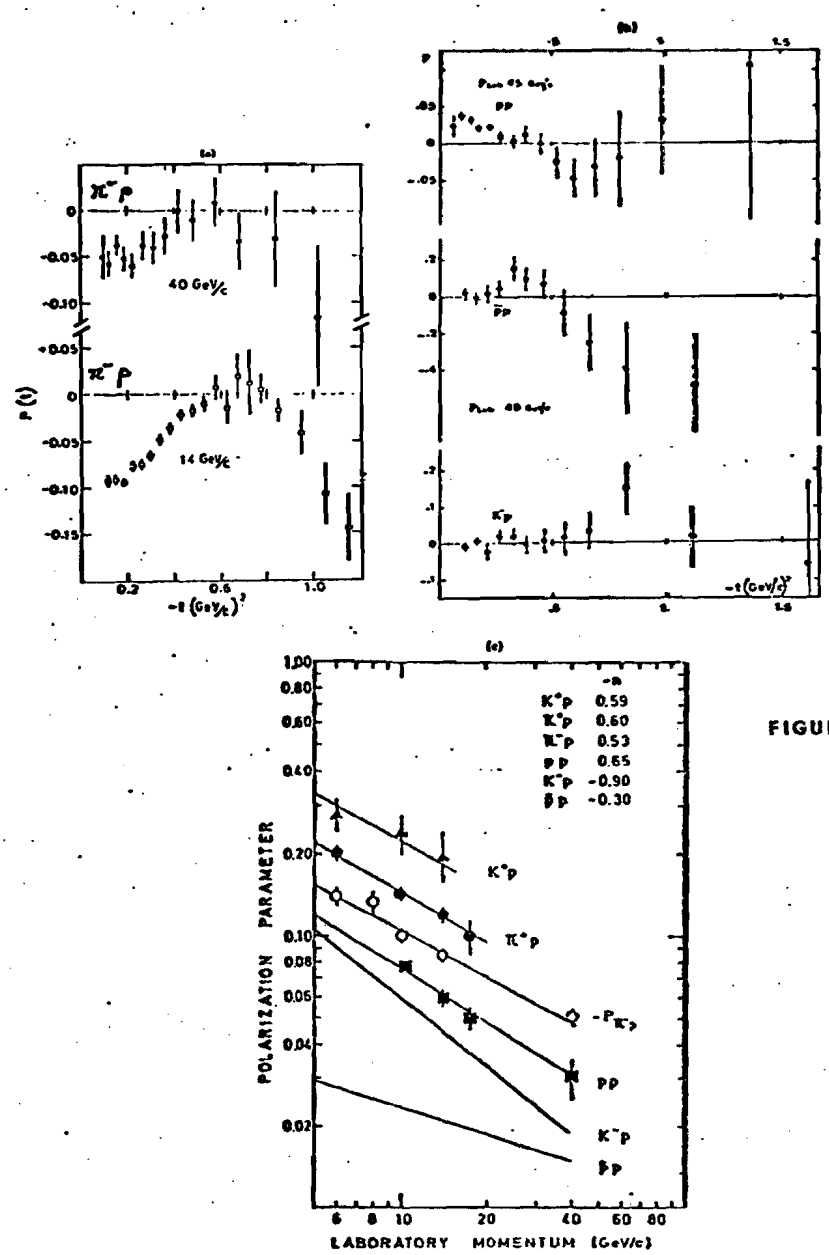
(a)
40 GeV/c
14 GeV/c
P(t)
-t (GeV/c)²
(b)
pp
K⁻p
-t (GeV/c)²
(c)
K⁺p 0.59
π⁺p 0.60
π⁻p 0.53
pp 0.65
K⁻p -0.90
p̄p -0.30
K⁺p
π⁺p
pp
K⁻p
p̄p
POLARIZATION PARAMETER
LABORATORY MOMENTUM (GeV/c)

FIGURE 2.5

imply a lambda polarization of about 0.02 for $t=-0.2(\mathrm{GeV}/c)^2$ at NAL energies; the polarization then decreases to zero at t of about $-0.5(\mathrm{GeV}/c)^2$ and then becomes negative as the magnitude of t increases further.

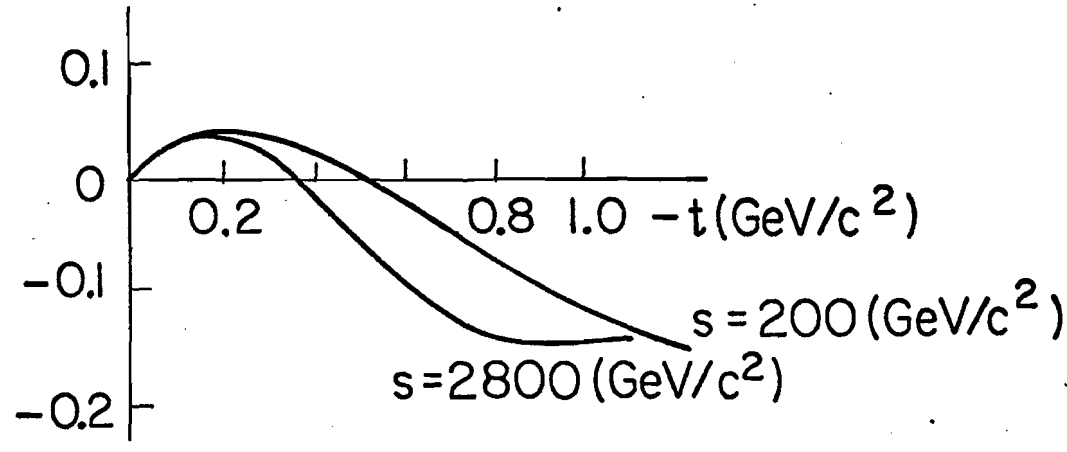

Fig. 2. 6.

CHAPTER 3

EXPERIMENTAL TECHNIQUES

The principle components of the experimental apparatus are [41]:

1. The incident proton beam and the neutral beam collimation system,
2. Neutral beam intensity monitors,
3. The liquid hydrogen target system,
4. The pair spectrometer,
5. The recoil proton detector,
6. The trigger electronics, and
7. The data acquisition system.

These components of the apparatus are discussed in Sections 3.1 - 3.7, respectively. Particular attention is given to design characteristics which were incorporated in the apparatus to minimize biases. Section 3.8 describes typical

data-taking conditions such as beam fluxes and trigger rates.

3.1 PROTON BEAM AND COLLIMATOR

Fig. 3.1 shows a plan view of the apparatus. The data were collected during two running periods, one at 300 GeV/c and the other at 400 GeV/c proton beam momentum. The diffracted proton beam, located in the Meson Laboratory M-2 line at Fermilab, was directed onto a 1/4"-diameter 1/2-interaction-length (15 cm.) beryllium target located at T in Figure 3.1. Typically 85% to 90% of the proton beam was contained within a circle of 6 mm. in diameter. A scintillator telescope S1 consisting of 6 mm. and 12 mm. diameter scintillators, and a 5 cm. diameter scintillator with a 6 mm. hole in its center (halo counter) was used to count the proton beam at low intensity (about 10^6 protons per 800 millisecond spill), and to check the absolute calibration of the argon filled ionization chamber. At the higher intensities of a few times 10^7 protons per spill which were used for data taking, the IC served as the primary proton monitor, although the halo counter was still used to measure the fraction of the proton beam outside the 6mm circle.

The neutral beam was formed by a collimation system incorporating a defining aperture near the center of a channel 5.3 meters long with a vertical magnetic field of 23

Plan view of the apparatus

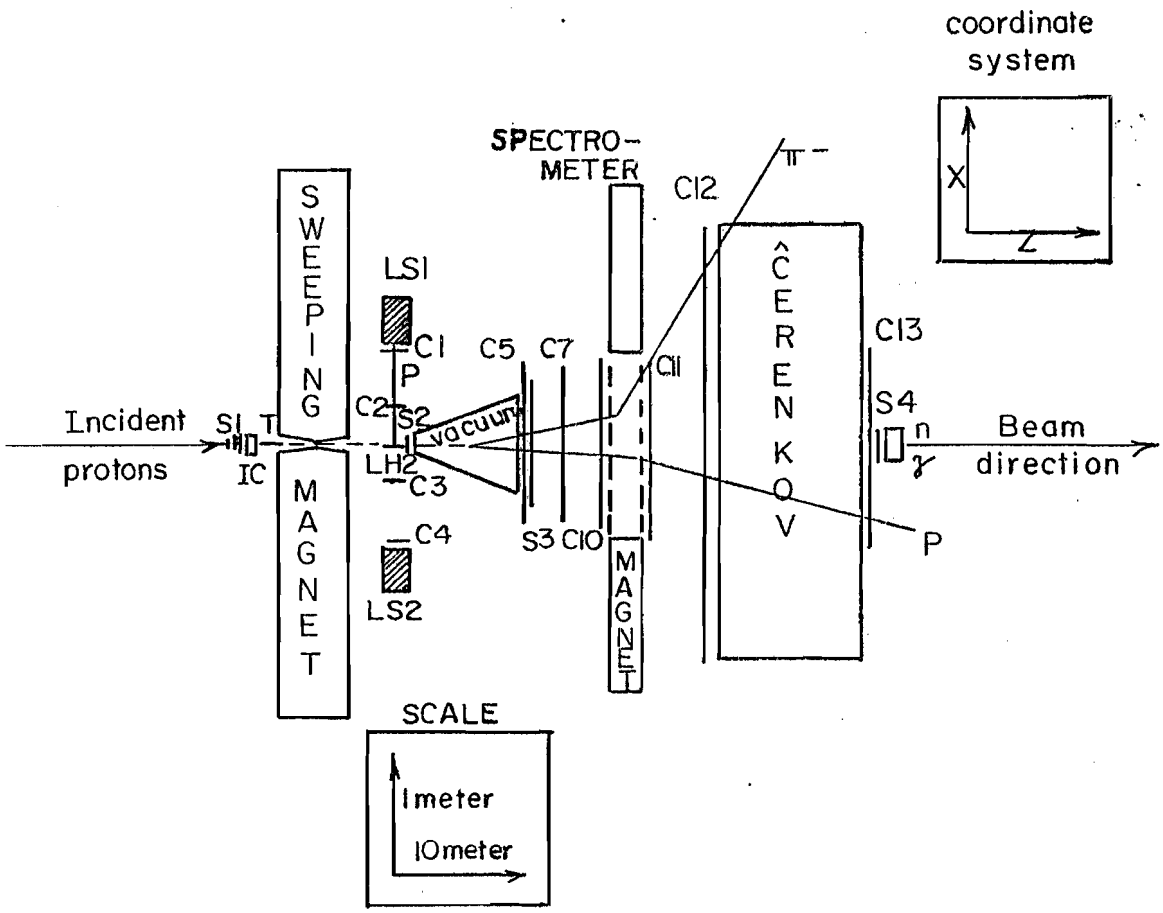

Fig. 3.1

kG. The central aperture was tungsten, 60 cm. long, with a 4 mm. diameter hole. The magnetic field bent the proton beam and the charged particles produced at the production target into the upstream end of the tungsten plug, or into larger aperture brass collimators upstream of the plug. Downstream of the plug, gradually increasing apertures in brass collimators served to remove secondaries made in the defining hole. No attempt was made to remove gamma rays or any other neutral component of the beam. Charged particles were effectively eliminated by this system. Any charged particles remaining in the neutral beam were detected by a scintillation counter S2 and were rejected by the trigger electronics (see Section 3.6). The resulting neutral beam which emerged from the downstream end of the collimator was about 1 cm. in diameter with a 1 mrad total divergence. The effective solid angle of the accepted neutral beam was calculated to be $(1.2 \pm 0.1)\times(10^{-6})$ sr.

One possible bias that could be caused by the collimation system arises from the fact that lambdas produced at nonzero production angles are polarized [40]. The neutral beam was therefore produced at approximately zero production angle. Deviations from zero production angle would result in a lambda polarization whose components would be given by the following [44]:

$$\alpha P_x = -0.039\ p_\Lambda\ \theta_y \qquad (3.1a)$$

$$\alpha P_y = -0.085\ p_\Lambda\ \theta_x \qquad (3.1b)$$

$$\alpha P_z = -0.076\ p_\Lambda\ \theta_y \qquad (3.1c)$$

where θ is the incident proton angle in radians and p_Λ is in GeV/c, and where the x, y, and z directions are defined with respect to the coordinate system shown in Figure 3.1. These relations assume the absence of parity violating components of the polarization [40].

3.2 NEUTRAL BEAM INTENSITY MONITORS

In addition to the proton beam intensity monitors which were described in the preceding section, there were counters which monitored the intensity of the neutral beam. The primary neutral beam monitor was a scintillator telescope located immediately downstream of the collimator exit. This telescope consisted of three pairs of scintillators. The first pair covered the right and left halves of the collimator exit hole; the second pair, half a meter downstream, covered the top and bottom halves of the neutral beam; and the third pair, half a meter farther downstream, covered the right and left halves of the neutral beam. A small fraction of the neutral beam interacted in the first pair of scintillation counters. The resulting charged tracks produced signals in the three pairs of scintillators which were combined in a logical "or". This signal was scaled and used as a monitor of the neutral beam intensity. Charged particles produced in this telescope were prevented from triggering the spectrometer data acquisition system by the veto counter, S2.

At the far downstream end of the apparatus, 40 meters from the downstream face of the collimator, the neutral beam was approximately 5 cm. in diameter. A secondary neutral beam intensity monitor was placed at this location to serve as a check on the stability of the primary monitors, and to give another measure of the total flux of neutrals in the beam. This monitor telescope contained a veto scintillator S4 and components to identify selectively the gamma rays and the neutrons in the beam.

3.3 THE LIQUID HYDROGEN TARGET SYSTEM

The elastic collisions took place in a liquid hydrogen target 91.4 cm. long and 3.81 cm. in diameter. The location of this target is shown in Figures 3.1, 3.2, and 3.3. The hydrogen target was cycled with a nearly identical, but evacuated, target flask every few synchrotron cycles. Incident lambdas which passed through the evacuated flask were recorded during part of each data taking run to measure the neutral beam direction and for background measurements.

Since the lambda and the proton have nearly equal masses, the recoil proton emerges from the hydrogen target in a direction nearly 90° from that of the scattered lambda. As the magnitude of t of the scatter increases, the recoil proton moves away from the perpendicular toward the scattered lambda direction. Because the number of events

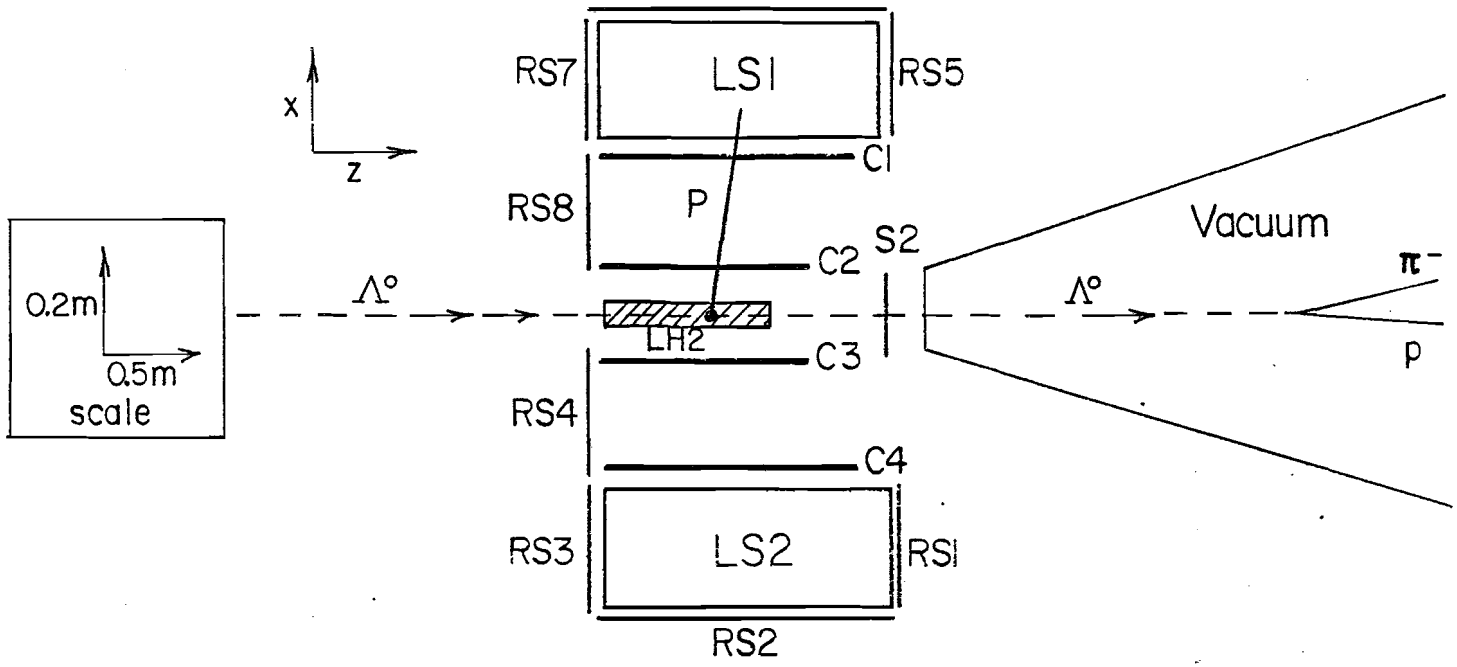
x
z
0.2m
0.5m
scale
Λ°
RS7
LS1
RS5
C1
RS8
P
C2
S2
LH2
C3
RS4
C4
RS3
LS2
RS1
RS2
Vacuum
Λ°
π⁻
p

Fig. 3.2.

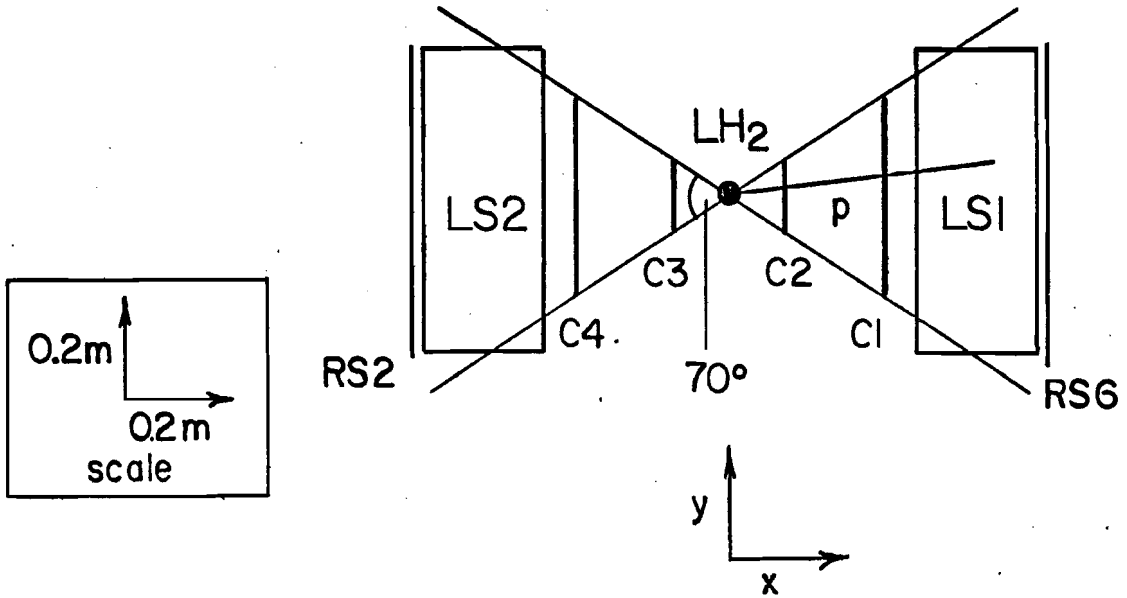

Fig. 3.3

decreases sharply as the magnitude of t increases, very few events were seen in this experiment with a t-value whose magnitude was greater than 1.5(GeV/c)^2. At this value of t, the recoil proton emerges from the hydrogen target about 60 degrees from the scattered lambda direction. At a value of t = -1.5 (GeV/c)^2 the angle between a 200 GeV/c incident lambda and the scattered lambda is about 6 mr.

The hydrogen target imposed a low t cutoff at about t = -0.05 (GeV/c)^2 because the recoil protons corresponding to t values smaller than this usually stop in the hydrogen target.

3.4 THE PAIR SPECTROMETER

The scattered lambda was reconstructed by detecting the decay products from the $\Lambda \rightarrow p + \pi^-$ decay. The scintillation veto counter S2, located immediately downstream of the liquid hydrogen target, defined the beginning of the decay volume for the scattered lambda. The lambda decayed in a 9 meter long evacuated pipe V. The first of six downstream multiwire proportional chambers (MWPC's) was placed next to the output window of the decay vacuum. The three chambers C5, C7, and C10, upstream of the spectrometer magnet M2, were separated by 3 meter long drift spaces. The active areas and wire spacings of all of the MWPC's are given in Table 3.1. The spectrometer magnet M2 was a ferric superconductor with an aperture 60 cm. wide x

Table 3.1

Active Areas of the MWPC's

Chamber #	Horizontal Size (cm.)	Vertical Size (cm.)
C1	128	38.4
C2	102.4	12.8
C3	102.4	12.8
C4	128	38.4
C5	51.2	25.6
C7*	38.4	38.4
C10	51.2	25.6
C11	63.2	25.6
C12	128	51.2
C13	63.2	25.6

All wire spacings were 2 mm.

* Wires were rotated 45° with respect to the z-axis.

Table 3.2

Composition of the Neutral Beam

Type of Particle	Number/10^6 protons	Average Momentum (400 GeV/c protons)
γ	3×10^3	not measured
n	2×10^3	not measured
Λ	40	220 GeV/c
K_S^o	4.5	140 GeV/c
K_L^o	4.5	not measured
$\bar{\Lambda}$	.5	120 GeV/c
Ξ^o	.02	160 GeV/c
$\bar{\Xi}^o$	.001	not measured

20 cm. high, an effective length of 190 cm., and a peak central field of 18 kG. Chamber 11 was located immediately behind the spectrometer, and chamber 12 was three meters downstream. Helium bags were placed in the drift spaces between chambers and in the magnet aperture to decrease multiple scattering. A low pressure threshold gas Cerenkov counter eleven meters long separated chambers 12 and 13. This counter was filled with helium at a pressure of 25 cm.Hg, corresponding to a proton threshold momentum of 170 GeV/c, and served to discriminate between baryons and mesons below this momentum which went through the counter near its axis. The total amount of material in the neutral beam was kept low to minimize absorption and multiple scattering. Each chamber presented 25 mg/cm^2 of carbon equivalent to the beam. The total material from the downstream edge of the 0.7 cm. thick veto scintillator through chamber 12 was about 1.3 gm/cm^2. The mirror and back Al window in the Cerenkov counter added another 1.7 gm/cm^2 just before chamber 13. The spectrometer magnet was operated at about 70% of its full field (corresponding to a bending power of 0.7266 GeV/c transverse momentum) for the 300 GeV/c incident proton beam, and at nearly full field (.9514 GeV/c) for the 400 GeV/c incident proton beam, so that charged particles with momenta above 50 GeV/c and 65 GeV/c, respectively, struck the active area of chamber 13. The different sizes chosen for chambers 12 and 13 can be understood from the large difference in the momenta of the decay products of the

lambda and from the low Q value of the lambda decay. The momentum ratio of the two decay products is typically about

$$p_\pi / p_p = m_\pi / m_p .$$

Thus chamber 12 can be thought of as the pion detector and chamber 13 the proton detector. This is illustrated by the "event" in Figure 3.1.

3.5 RECOIL PROTON DETECTOR

Apparatus for the detection of the recoil proton was placed on both sides of the liquid hydrogen target. Two views of this portion of the apparatus are shown in Figures 3.2 and 3.3. When the liquid hydrogen- filled flask was in the neutral beam, elastically recoiling protons were detected in one of the two pairs of MWPC's C1, C2 (arm 1) or C3,C4 (arm 2). The active areas and wire spacings of these chambers are given in Table 3.1. Tanks filled with liquid scintillator LS1 and LS2 were placed next to C1 and C4 in order to measure the energy of the recoil proton. These tanks were 75 cm. high, 150 cm. wide, and 30 cm. thick and each held about 300 liters of liquid scintillator. Beside each tank were plastic scintillation counters RS2 and RS6 to detect protons passing through the tank. Additional scintillation counters RS3, RS4, RS7, and RS8 served to veto muons emerging from the collimating magnet M1; while RS1-RS3 or RS5-RS7 coincidences could be used to calibrate the tanks with these muons. Any charged particles in the neutral

beam, including lambdas which decayed too near the hydrogen target were vetoed by RS9 (=S2). The chambers were placed to accept any particle emerging from the target in an angular interval of 60°-90° relative to the beam axis and within $\pm 30^{o}$ of the horizontal plane (see Figures 3.2 and 3.3).

The recoil proton detection system and the pair spectrometer were designed to minimize any apparatus-induced biases. Recall from Section 2.2 that the parity allowed polarization arising from elastic scattering is parallel to $\hat{p}_1 \times \hat{p}_3 = \hat{n}$. We see that the normal $\hat{n}$ to the scattering plane was approximately the +y direction if the recoil proton passed through C3 and C4. Conversely, $\hat{n}$ was approximately the -y direction if the recoil proton passed through C1 and C2. This reversal served as a check on apparatus-induced biases, including contributions from the inclusive polarization.

The parity allowed component of the lambda polarization was insensitive to nonzero lambda production angles in the vertical plane (see relations 3.1). Any component of the polarization arising from nonzero lambda production angles in the horizontal plane is easily measured by examining the polarization of the unscattered lambdas. This is discussed in greater detail in chapters 4 and 5.

Another check on apparatus-induced biases was the spectrometer magnet M2. This magnet could be run at either polarity, which served as a check on right-left asymmetries in the portion of the pair spectrometer downstream of M2.

3.6 TRIGGER ELECTRONICS

Prompt signals from the MWPC planes were used as trigger signals. The finest hodoscope mesh employed was 64 wires wide (128 mm), and only the vertical wires (horizontal coordinates) were used for this purpose. The horizontal wires were all added together in a logical "or" and placed in coincidence with the vertical wire pattern to give a chamber output pulse. This was done at each chamber in emitter-coupled logic (MECL -0.75V to -1.5V). In this way any logical combination of signals from scintillators, MWPC's, and the Cerenkov counter could be selected to generate a trigger signal.

The good event trigger used for collecting data was composed of the logical AND of two parts: a neutral-vee trigger and a recoil-proton trigger. The neutral-vee trigger was very unrestrictive, requiring one or more hits in each of C5, C7, C10, C11, C12, and C13. This was vetoed by pulses from S2 to eliminate premature decays or charged tracks, other than those originating from decays in the evacuated volume V. A scintillator S3 was included in the trigger in order to sharpen the coincidence timing. The

recoil-proton trigger required one hit in both C1 and C2 <u>or</u> at least one hit in both C3 and C4. This was vetoed by scintillation counters RS4 and RS8 to prevent accidental coincidences caused by muons emerging from M1. The liquid scintillator tank pulse heights were not used in the trigger, but were read out with each event. The resultant good event trigger logic can be represented by the following relation:

$$GE1 = [(C1.C2) + (C3.C4)] \,.\, \overline{RS4} \,.\, \overline{RS8} \,.$$
$$.\, \overline{S2} \,.\, S3 \,.\, C5 \,.\, C7 \,.\, C10 \,.\, C11 \,.\, C12 \,.\, C13 \qquad (3.2)$$

This good event trigger was also used when the evacuated flask was in the neutral beam in order to check backgrounds. In addition, when the evacuated flask was in place, the recoil proton portion of the trigger was removed periodically from the good event logic and the remaining neutral vee trigger:

$$GE2 = \overline{S2} \,.\, S3 \,.\, C5 \,.\, C7 \,.\, C10 \,.\, C11 \,.\, C12 \,.\, C13 \qquad (3.3)$$

was used to allow unscattered lambdas to be written to tape. The unscattered lambdas were used to monitor the absolute lambda flux and to measure the direction of the neutral beam. The hydrogen-filled flask and the evacuated flask were cycled every few spills to monitor any fluctuations in the direction or intensity of the neutral beam and to make a target-out subtraction to be used in a measurement of the differential cross section [45].

If an event satisfied the good-event trigger logic, an enable pulse was sent back to each chamber, which allowed flip-flops to be set, thus storing the coordinate information pertinent to that event. The trigger logic also generated its own dead time, which remained in force until the read-out process was completed, and sent a priority interupt to the PDP11/45 computer. The computer read all the data via CAMAC, including pulse height information, all of the chamber wire-hit addresses, and a set of flip-flops (latches) corresponding to which counters gave pulses for the event. The typical time to read a complete event was 0.5 msec. The act of reading reset all the registers and the trigger logic dead time gate was removed by the computer when the system was ready for the next event. Once each accelerator cycle, at the end of the beam spill, a separate CAMAC crate containing various gated and ungated monitor scalers and the accumulated charge from the ion chamber for that synchrotron cycle was read and cleared by the computer, thus recording the necessary normalization information.

3.7 ON-LINE PROGRAM

A program was written for the PDP11/45 computer which read the data for each event from CAMAC, stored it in a buffer in core memory, and wrote events directly on magnetic tape when the buffer was full. Tape writing speed during the spill limited the event rate to 640 events/spill. The

events remaining in the buffer at the end of the spill were used to generate histograms stored on a disk. These included hit patterns for each chamber to furnish an on-line check on the quality of the chamber operation. Latch patterns and pulse height distributions from various counters were also histogrammed. The scaler and ion chamber data were written to magnetic tape in a special scaler record every spill.

3.8 NORMAL RUNNING CONDITIONS

The intensity of the proton beam incident on the target T (Figure 3.1) was typically one or two times 10^7 protons per accelerator cycle (spill). The proton beam intensity was lowered to about 10^6 protons per spill briefly before each data taking run to check the calibration of the ionization chamber.

A number of runs were taken with the field in the collimator magnet M1 turned off and the proton beam directed through the collimator at low intensity (about 10^5 protons per spill). These runs produced pp elastic scatters which were used to help measure the relative positions of the recoil chambers with respect to the pair spectrometer chambers. For another type of run, both M1 and M2 were turned off and the measured proton beam direction was used to define the z-axis of the coordinate system which is shown in Figures 3.1 - 3.3.

The composition of the neutral beam is shown in Table 3.2. The long-lived components of the neutral beam (principally gammas and neutrons) were the primary source of background events.

During the normal data taking runs, the proton beam intensity of 10^7 protons on the target T produced about 50 triggers per 0.8-second beam spill using trigger GE1 (see Section 3.6). The trigger rate during the vacuum portion of each run resulted in a similar trigger rate because of the intermittent presence of the neutral vee trigger GE2. Each tape contained about 70,000 vee triggers (GE1 or GE2), and 10,000 muon triggers which could be used to calibrate the liquid scintillator tanks. The length of the accelerator cycle was about 12 seconds. The time required to write a typical data tape was about 4-5 hours.

The contents of a typical data tape are shown in Table 3.3. A total of 72 of these data tapes was taken during the six week run in February and March of 1976.

Table 3.3
Composition of a Typical Data Tape (Run 670)

Target in Beam	Good Event Trig. Type	Type of Event	Number of Triggers	Subcategory	Comments
Liquid Hydrogen	GE_1	Λ-p elastic	1648		These events passed all tests for being elastic events, and were the input for the polarization program.
		K_s^op elastic	83		
		$\bar{\Lambda}$- p elastic	14		
		Other Λ-p scatters	4825	$r^2_{tgt}<1cm^2$	These events had a detected Λ plus something in the recoil planes, but failed tests for an elastic event.
			2479	$r^2_{tgt}>1cm^2$	
64332 total triggers	64332 total triggers		7304	Total	
		Background Triggers	55283		mostly $\gamma \rightarrow e^+e^-$ and neutron interactions.
Vacuum	GE_1	Λ "scatters"	414	$r^2_{tgt}<1cm^2$	These events had a detected plus something in the recoil chambers. Two of these passed elastic tests, but had marginal tgt pointing.
			42	$r^2_{tgt}>1cm^2$	
	3552 total triggers		456	Total	
		Background Triggers	3096		mostly $\gamma \rightarrow e^+e^-$ and neutron interactions.
	GE_2	Λ	1435		
		K_s^o	129		
		$\bar{\Lambda}$	23		
	2143 total triggers	Background Triggers	556		mostly $\gamma \rightarrow e^+e^-$, single tracks, and neutron interactions.
15732 total triggers	RS1-RS3 or RS5-RS7 coinc.	Liquid Scint. Tank Calib. Triggers	10037		These triggers were caused by muons coming from the downstream face of M1.
Total Triggers on Tape --			80064		

CHAPTER 4

DATA ANALYSIS

The off-line analysis was done in three stages. The first stage of the analysis, which is discussed in Section 4.1, reconstructed the tracks of the decay products of the scattered particle from the MWPC information from C5-C13 (see Figure 3.1). This information was then compacted onto data summary tapes, together with the MWPC information from C1-C4. The second stage of the analysis, described in Section 4.2, used this information to reconstruct the recoil proton track, and to calculate the four-momentum of the incident particle and its scattering vertex position. If the event passed tests which were used to define elastic scatters, it was written onto another tape to be used for the polarization measurement. The polarization analysis programs are described in Section 4.3. Section 4.4 discusses the analysis which was done to eliminate biases in the apparatus and in the reconstruction programs.

4.1 THE TRACK RECONSTRUCTION PROGRAM

The raw data tapes were processed by a reconstruction program which searched for events which had two tracks emerging from a common point in the decay volume (neutral vees). The first step of this process was to convert the wire addresses into positions in space using the coordinate system defined by the incident proton beam (see section 3.8). Information from chambers 5, 10, 11, 12, and 13 gave projections of the particles' trajectories in the (x,z) and (y,z) planes. Tracks in the two views were reconstructed independently and were matched using information from chamber 7 whose wires were at 45 degrees. A number of conditions resulted in rejection of the potential event. These are listed with brief explanations where necessary in Appendix A.1.

Once an event was accepted by the track reconstruction program, pertinent information was computed, including the 3-momenta of the two tracks, and the position of the decay vertex. This information, together with the wire hit information from chambers 1-4 and the error matrix obtained in the track fitting, was then written onto a summary tape. In this way most single tracks, neutron interactions, and gamma conversions were eliminated from the data sample. The task of reconstructing the recoil track was left to the next stage of the analysis.

4.2 THE ELASTIC SCATTERING RECONSTRUCTION PROGRAM

The summary tapes which were written by the track reconstruction program were processed by a program which searched for tracks in chambers 1 and 2 (arm 1) or chambers 3 and 4 (arm 2). This information was used, together with the information about the neutral vee, to complete the reconstruction of the elastic scatter.

For each recoil arm, four categories of wire hit topologies were defined. These categories are shown in Table 4.1. Each event was assigned an ordered pair of numbers (i,j) which specified the hit topologies in arms 1 and 2, respectively. Only events of the types (2,0), (0,2), (2,1), (1,2), (3,0), and (0,3) were examined further by the reconstruction program. Over 90% of the detected elastic scatters fell into one of these disjoint categories [45]. Events of the types (2,0), (0,2), (2,1), and (1,2) yielded only one possible recoil proton track. For the (3,0) and (0,3) type events, which resulted in more than one possible recoil proton track, all possible tracks were checked and the best track (see below) was kept. A number of conditions resulted in the rejection of events. These are listed in Appendix A.2.

About two-thirds of the events with a satisfactory Λ were found to have a clean recoil proton track. For these events the position and direction of the recoil track, and the momentum vector of the scattered Λ were determined.

Table 4.1
Classification of Hit Topologies in the Recoil Arms

Category	Hit Structure
0	No hits in either chamber.
1	Missing hits in one, two, or three of the wire planes.
2	Exactly one hit in each of the four wire planes.
3	Wire hits in all planes. More than one hit in one or more planes.

Table 4.2
Monte Carlo Events Fed Directly into the Polarization Program

Momentum	t	αP	$\delta(\alpha P)$	Analysis axis
0-120	0.1-0.2	-0.04	0.12	1 $(=\hat{p}_1 x \hat{p}_3)$
		+0.02	0.14	2 $(=\hat{p}_1)$
		-0.11	0.12	3 $(=(\hat{p}_1 x \hat{p}_3) x \hat{p}_1)$
	0.2-0.4	-0.07	0.17	1
		+0.12	0.18	2
		-0.03	0.16	3
	0.4-0.8	+0.17	0.34	1
		-0.44	0.48	2
		-0.27	0.34	3
120-200	0.1-0.2	+0.08	0.05	1
		-0.03	0.05	2
		+0.08	0.04	3
	0.2-0.4	+0.10	0.06	1
		-0.07	0.06	2
		+0.05	0.05	3
	0.4-0.8	-0.03	0.11	1
		-0.04	0.11	2
		-0.15	0.11	3
200-280	0.1-0.2	+0.05	0.05	1
		+0.08	0.05	2
		+0.06	0.05	3
	0.2-0.4	+0.02	0.05	1
		+0.02	0.05	2
		+0.03	0.05	3
	0.4-0.8	-0.11	0.09	1
		-0.01	0.10	2
		+0.05	0.08	3
280-400	0.1-0.2	-0.01	0.05	1
		-0.03	0.05	2
		-0.04	0.05	3
	0.2-0.4	0.00	0.05	1
		-0.02	0.06	2
		+0.08	0.06	3
	0.4-0.8	+0.01	0.10	1
		-0.12	0.10	2
		+0.09	0.10	3

Assuming elastic scattering, the trajectory of the incident Λ was calculated and projected back to the position of the production target. The selection of elastic events was based on two criteria: the recoil track and the scattered Λ trajectory must intersect in the hydrogen target, and the calculated trajectory of the incident Λ must project back to the production target. The coplanarity and opening angle constraints for an elastic event were combined in the target pointing test. This test was made by calculating the radial distance from the measured center of the incident Λ beam to the incident Λ trajectory projected back to the target position. The position of the incident Λ beam was measured using a sample of unscattered Λ's which were collected at the same time as the elastic data. Figure 4.1(a) shows the distribution of the square of this radial distance r^2 for a typical data tape. The tail of this distribution is composed primarily of inelastic interactions in the hydrogen target and extends far beyond the end of the figure. The target pointing requirement was a severe test since the 6 mm diameter production target was located 8 meters upstream of the elastic scattering vertex. The dashed curve in Figure 4.1(a) is the same parameter for a sample of unscattered Λ's. Occasionally an event of the type (3,0) or (0,3) would result in more than one possible recoil proton track with an acceptible value for r^2. In this case, the track which resulted in the smallest value of r^2 was kept.

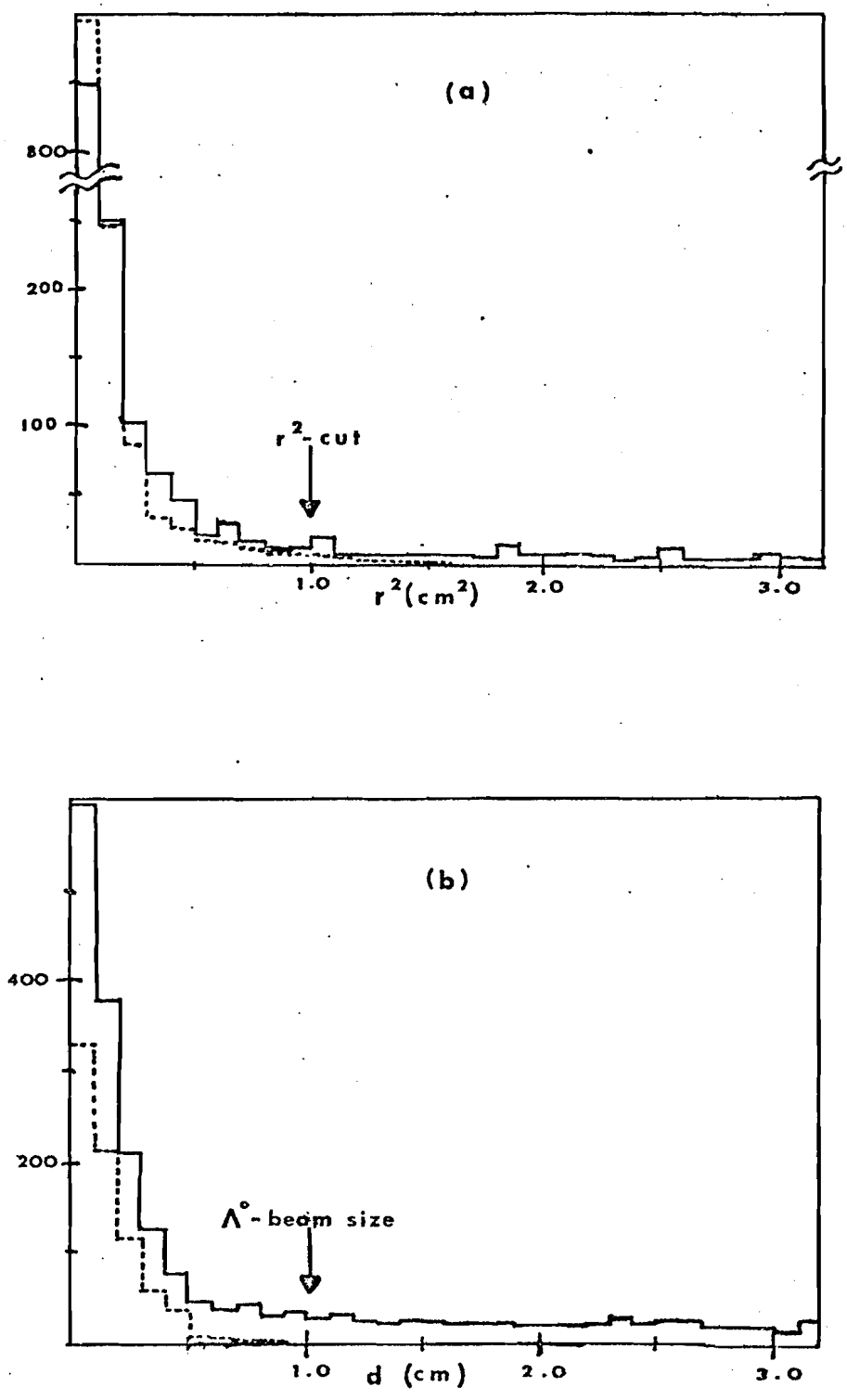
(a)
800
200
100
r²-cut
1.0
r²(cm²)
2.0
3.0
(b)
400
200
Λ°-beam size
1.0
d (cm)
2.0
3.0

FIGURE 4.1

Figure 4.1(b) shows the distribution of the distance of closest approach between the recoil track and the scattered Λ trajectory. The dashed line shows the same parameter for those events passing the target pointing cut which is shown in Figure 4.1(a). It is clear from Figure 4.1(b) that events which satisfy the target pointing cut have a well-defined scattering vertex.

There were two principle sources of background triggers: inelastic scatters and accidental tracks in the recoil chambers associated with an unscattered Λ. Inelastic scatters were largely eliminated by the r^2-cut. Background from accidental triggers would show a broad distribution in Figure 4.1(b). The distribution of events remaining after the r^2-cut was consistent with experimental resolution. Extrapolation of the tail of the r^2 distribution to $r^2 = 0$ gave an estimate of 4% for the total background contribution to the data sample. The effect of this background was checked by doing polarization analyses with r^2 cuts at 0.4 and at 1.0 cm^2. The measured polarizations for these two cuts showed no significant differences.

Events which met all criteria for being elastic scatters were written onto a condensed summary tape to be used by the final stage of the analysis, the polarization program. This data compacting process enabled the useful events from six weeks of data taking (about 5×10^6 triggers

on 71 raw data tapes) to be put onto a single magnetic tape.

4.3 THE POLARIZATION PROGRAM

The input for the third and final stage of the off-line analysis was the condensed summary tape containing only useful elastic scatters. This tape contained three types of scattered particles: Λ , K_s, and $\bar{\Lambda}$. Each scattered particle type was examined separately.

At fixed values of t and incident energy the polarization P of the scattered particle would appear as a distribution $(1 + P \cos \theta^*)$ in the rest system of the scattered particle. The angle θ^* is the polar angle of the proton relative to some spin analysis direction. The asymmetry parameter, α , is 0.647 for Λ , -0.647 for $\bar{\Lambda}$, and 0 for K_s. The events were binned according to their values of the calculated incident particle momentum and t. Next, three mutually orthogonal spin analysis axes were defined (for each event) in the following manner:

1. $\hat{n} = \hat{p}_1 \times \hat{p}_3$ (the normal to the scattering plane)

2. $\hat{l} = \hat{p}_1$ (the incident lambda direction)

3. $\hat{m} = (\hat{n}) \times (\hat{l})$

All other calculations done by the polarization program used only information about the decay of the scattered lambda.

Data which described the trajectories of the scattered lambda's decay products were first put through an acceptance program. This program contained reconstructions of the chamber volumes and the spectrometer magnet aperture which were made slightly smaller than those of the real apparatus to eliminate biases from acceptance edges. The good event trigger for the scattered lambda was duplicated for the reconstructed real event, but with the new smaller fiducial volumes. If the event failed to satisfy this good event trigger, it was rejected. A list of reasons for event rejection at this stage of the analysis is given in Appendix A.3.

For events which were passed by this stage of the analysis, the polarization was calculated by two methods: the maximum likelihood method and a minimum chi-squared method. Separate calculations were done using each method for each of the three spin analysis axes, thus measuring the parity allowed component (P_1) and two parity violating components of the polarization, P^2 and P^3.

The maximum likelihood method computed for each event the likelihood $L_i(p)$ that the lambda decay i was part of a polarized distribution relative to one of the spin analysis axes. The likelihood for each event was given by

$$L_i(p) = (1 + P \cos \theta_i^*) / \int_{acc} (1 + P \cos \theta^*) d \cos \theta^*$$

where $\cos \theta_i^*$ was the decay proton direction in the lambda

rest frame relative to one of the spin analysis axes and $\int_{acc}$ was the integral over the acceptance for the event. The likelihood function for the set of N events is

$$L(P) = \prod_{i=1}^{N} L_i(P)$$

and the most probable polarization occurs when L(P) is maximum. The acceptance integral for each event was calculated by generating fake events identical to the real events but with values of cos θ^* evenly spaced through the entire interval of cos θ^*. These events were run through the acceptance program, with edges in the acceptance regions of cos θ^* being found by interpolation. The likelihood was then parametrized as a function of the polarization P to avoid the necessity of generating a large table of likelihoods for different values of P. This method is described in greater detail in Appendix B.

The minimum chi-squared method generated 10 fake events randomly distributed over the acceptance region in cos θ^* for each real event. These events were used to generate a Monte Carlo distribution in cos θ^* which was compared with that of the real events using a χ^2-test. The fake event distribution in cos θ^* was parametrized as a function of P in order to avoid the necessity of generating separate distributions in cos θ^* for many different values of P. This method is described in greater detail in Appendix C.

The maximum likelihood calculation is the best statistical technique for obtaining the polarization, because each event contributes independently to the final result. There is a possibility of making small systematic errors in the acceptance integral calculation, however. Such errors could be caused by very small acceptance regions in cos θ^* which lay entirely between adjacent values of cos θ^* of the fake events used in the acceptance calculation. The fake events used in the acceptance calculation are generated at values of cos θ^* given by -1.0,-0.9,-0.8, ... ,0.9,1.0. Thus an acceptance region lying in the interval $0.51 \leq \cos\theta^* \leq 0.59$, for instance, would be missed in the acceptance calculation. Therefore, the minimum chi-squared method, which is not subject to this defect, was introduced as a check on the calculation of the acceptance integral in the maximum likelihood method.

The value of P obtained by the maximum likelihood method P_{lik} corresponds to the most probable value of P, while the value of P obtained by the minimum chi-squared method P_{chi} corresponds to a value of P for which the Monte Carlo cos θ^* distribution of events gives the best fit when compared with the real event cos θ^* distribution. Even assuming that there are no systematic errors in either computational method, the results of the two polarization calculations are not equal, in general, since there is a statistical contribution to P_{chi} due to errors of estimation which is not present in P_{lik} [35]. The two values converge

rapidly to a common value, however, as the number of events in the sample increases. In this analysis, a sample of Monte Carlo events much larger than the sample of real events was processed in order to minimize this difference, and there were no significant differences in the results of the two computational methods. The values for the polarization presented in Chapter 5 are P_{1ik}.

4.4 BIAS CHECKS

As was discussed in the preceding section, the polarization calculation required the generation of a large sample of fake events based on the real events which were being processed. Therefore, checking for any discrepencies between the real events and the fake events provided a powerful tool with which to search for apparatus or software biases. A number of quantitative comparisons of this type were incorporated into the polarization analysis programs.

One such set of comparisons between the real and the fake events was MWPC hit distributions. The acceptance program propagated real and fake events through a reconstruction of the experimental apparatus and kept track of the positions in space of the scattered particles' decay products in the MWPC's. The resulting distributions for real and fake events were histogrammed, normalized to each other, and compared via a χ^2-test. Typical results from the Λ-p elastic scattering data are shown in Figure 4.2(a)

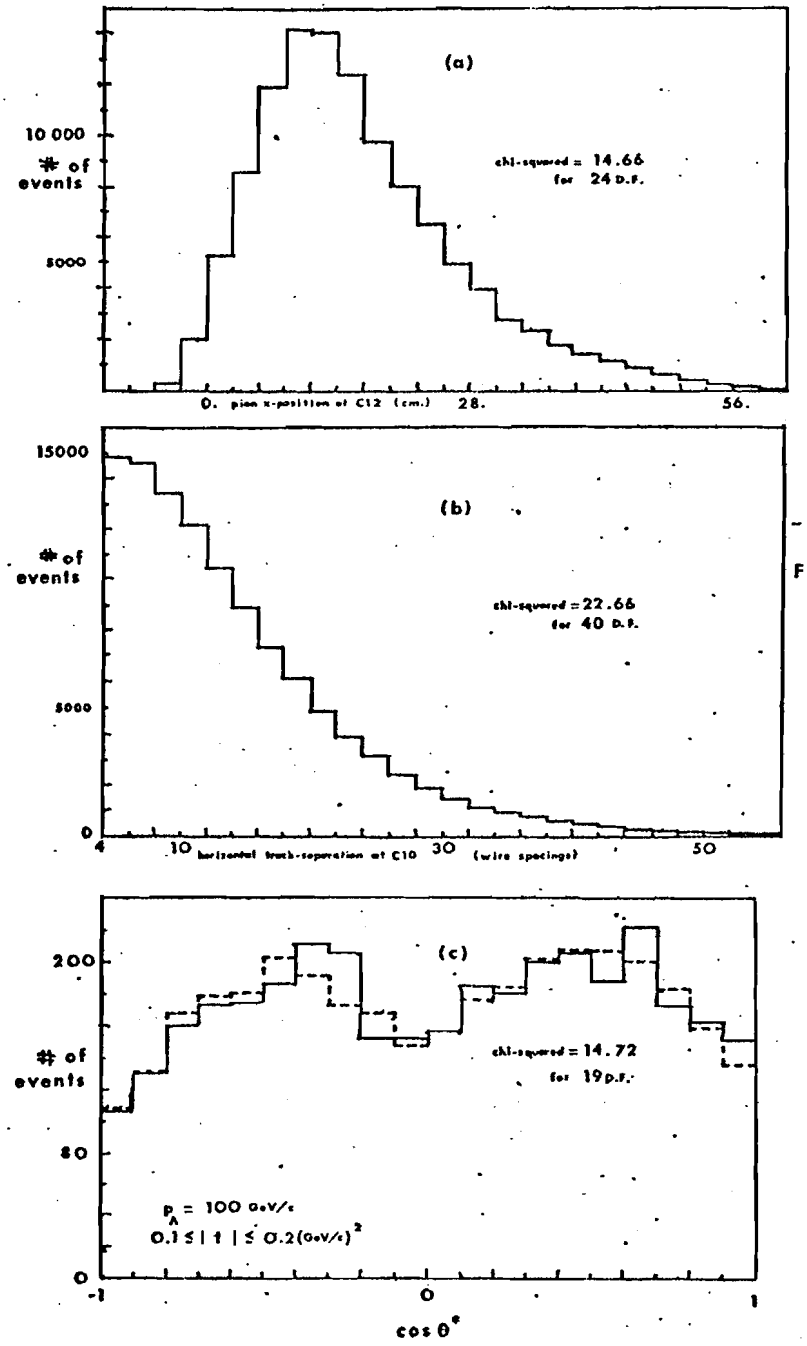
(a)
10 000
# of events
5000
chi-squared = 14.66
for 24 D.F.
0. pion x-position at C12 (cm.) 28.
56.
(b)
15000
# of events
5000
0
chi-squared = 22.66
for 40 D.F.
4
10
horizontal track-separation at C10
30
(wire spacings)
50
(c)
200
# of events
80
0
chi-squared = 14.72
for 19 D.F.
p_Λ = 100 GeV/c
$0.1 \le |t| \le 0.2 (GeV/c)^2$
-1
0
1
cos θ*

FIGURE 4.2

which displays the horizontal coordinate of the pion from the $\Lambda \rightarrow p\pi^-$ decay at C12. The differences between the real event distribution and the normalized fake event distribution are too small to appear in the plot. However, the value of chi-squared for the fit of the fake distribution to the real event distribution is shown.

Another comparison which was found to be of interest was the distance between the tracks of the scattered particle's decay products in C5 and C10. Typical results of this type of comparison are shown in Figure 4.2(b), which shows the horizontal track-separation at C10. Again the differences between the real and fake event distributions are too small to appear in the figure, but the value of chi-squared for the fit is shown. The separation is measured in units of MWPC wire spacings (2 mm/wire). There was a general tendency in the track-separation comparisons for a bad value of chi-squared at small separations. This was due to the graininess of the MWPC's. A track separation cut was used to eliminate this source of bias. The effects of the problem at small values of the track-separation will be discussed in more detail later.

Another useful comparison between the real and fake events was the event distributions in cos θ^*. Both the likelihood method and the chi-squared method calculated a "best" value for the polarization and generated cos θ^* distributions for the fake events. The comparison of these

"best" distributions with the real event cos θ^* distributions via a χ^2-test gave an excellent measure of the quality of the data. A typical comparison of this type is shown in Figure 4.2(c) for the Λ-p data with scattered Λ momenta less than 120 GeV/c in the t interval $0.1 \leq |t| \leq 0.2$ $(GeV/c)^2$. This time a bin with relatively few events is shown, so the differences between the real and fake event distributions appear in the figure. The solid line shows the real event distribution and the dashed line shows the fake event distribution. The value of chi-squared for the fit is also shown.

Processing certain control samples of data other than the Λ-p elastic scattering data allowed the selective testing of various sections of the software analysis programs. Therefore, several checks were made on data samples other than the elastic scattering data. In each of these checks the chamber fits and the fits in cos θ^* were examined for any discrepencies which would indicate biases. These data sets included Monte Carlo events and unscattered lambdas.

A Monte Carlo sample of lambda-p elastic scatters was generated at P=0 by an independent Monte Carlo program. These events were fed directly into the polarization program to check the acceptance program and the mechanics of the polarization analysis program. The polarizations obtained in this analysis are shown in Table 4.2. The chamber fits

and the cos θ^* fits showed no large biases.

Next the same sample of Monte Carlo events was written in a format nearly identical to that written by the online computer program (see Section 3.7). This set of events was put through the first and second stages of the off-line analysis program (described in sections 4.1 and 4.2) in order to probe for biases introduced by the track reconstruction programs. The events which were passed by these analysis programs were then analyzed by the polarization program. The polarizations obtained are shown in Table 4.3. It was found that these events showed a bias with respect to $\hat{I}$ at high momentum. The bias was roughly independent of t. The track separation and cos θ^* distributions for the Monte Carlo events and the fake events showed that the cause of the bias was the loss of events by the track reconstruction program whose decay products had an opening angle too small to be resolved well from the MWPC information. The effect grew worse as the lambda momentum increased because more and more of the decays at higher momenta had opening angles too small to be resolved due to the granularity of the MWPC data. This bias was eliminated by adding a track separation requirement in C5 and C10 in the acceptance program (see Appendix A.3). The events were then rerun with this cut added. The resulting polarizations are shown in Table 4.4 for lambdas with momenta above 120 GeV/c. Another set of events was generated with better statistics for lambdas with momenta below 160 GeV/c. The

Table 4.3

Monte Carlo Events Filtered Through the Track Reconstruction Program

Momentum	t	αP	$\delta(\alpha P)$	Analysis Axis
0-120	0.1-0.2	-0.06	0.12	1 $(=\hat{p}_1 \times \hat{p}_3)$
		+0.05	0.14	2 $(=\hat{p}_1)$
		+0.01	0.13	3 $(=(\hat{p}_1 \times \hat{p}_3) \times \hat{p}_1)$
	0.2-0.4	+0.05	0.21	1
		+0.43	0.21	2
		-0.17	0.19	3
120-200	0.1-0.2	+0.06	0.05	1
		0.00	0.05	2
		+0.07	0.04	3
	0.2-0.4	+0.09	0.06	1
		+0.02	0.06	2
		+0.07	0.06	3
	0.4-0.8	-0.17	0.13	1
		+0.04	0.16	2
		-0.20	0.13	3
200-280	0.1-0.2	+0.05	0.05	1
		+0.22	0.05	2
		+0.11	0.05	3
	0.2-0.4	+0.06	0.06	1
		+0.01	0.06	2
		+0.02	0.06	3
	0.4-0.8	+0.02	0.11	1
		+0.05	0.13	2
		+0.14	0.11	3
280-400	0.1-0.2	-0.02	0.05	1
		+0.18	0.06	2
		-0.04	0.05	3
	0.2-0.4	-0.01	0.07	1
		+0.18	0.08	2
		+0.11	0.07	3
	0.4-0.8	-0.01	0.13	1
		+0.16	0.16	2
		+0.14	0.14	3

Table 4.4

Monte Carlo Events with Track Separation Cut (p_Λ>120GeV/c)

Momentum	t	αP	$\delta(\alpha P)$	Analysis Axis
120-200	0.1-0.2	+0.05	0.05	1(=$\hat{p}_1 x \hat{p}_3$)
		-0.01	0.05	2(=$\hat{p}_1$)
		+0.07	0.05	3(=$(\hat{p}_1 x \hat{p}_3) x \hat{p}_1$)
	0.2-0.4	+0.13	0.07	1
		+0.01	0.08	2
		+0.07	0.08	3
	0.4-0.8	-0.14	0.15	1
		-0.15	0.20	2
		-0.23	0.15	3
200-280	0.1-0.2	+0.04	0.05	1
		+0.19	0.05	2
		+0.14	0.05	3
	0.2-0.4	+0.01	0.07	1
		+0.03	0.07	2
		+0.02	0.07	3
	0.4-0.8	-0.09	0.12	1
		-0.09	0.14	2
		+0.14	0.12	3
280-400	0.1-0.2	-0.04	0.07	1
		+0.11	0.08	2
		-0.02	0.06	3
	0.2-0.4	-0.04	0.08	1
		+0.01	0.11	2
		+0.06	0.09	3
	0.4-0.8	-0.04	0.18	1
		-0.12	0.20	2
		+0.29	0.17	3

Table 4.5

Monte Carlo Events with Track Separation Cut (p_Λ<160GeV/c)

Momentum	t	αP	$\delta(\alpha P)$	Analysis Axis
0-120	0.1-0.2	-0.03	0.03	1(=$\hat{p}_1 x \hat{p}_3$)
		+0.02	0.03	2(=$\hat{p}_1$)
		-0.05	0.03	3(=$(\hat{p}_1 x \hat{p}_3) x \hat{p}_1$)
	0.2-0.4	-0.007	0.05	1
		+0.05	0.07	2
		+0.01	0.05	3
	0.4-0.8	+0.02	0.13	1
		+0.26	0.19	2
		+0.16	0.14	3
120-160	0.1-0.2	+0.005	0.016	1
		+0.015	0.018	2
		-0.024	0.015	3
	0.2-0.4	+0.03	0.03	1
		+0.04	0.03	2
		+0.02	0.03	3
	0.4-0.8	-0.006	0.06	1
		+0.09	0.07	2
		+0.15	0.06	3

polarizations resulting from this calculation are shown in Table 4.5. The chamber fits and the cos θ^* distributions showed no significant biases once the track separation cut was applied.

A high precision check on both apparatus and program biases was provided by the unscattered lambdas (beam lambdas) which were taken during each data run with the trigger GE2 described in section 3.6. The data tapes contained more than twice as many beam lambdas as scattered lambdas. There was no scattering plane for the beam lambdas, so the x, y, and z axes were used by the polarization analysis. These axes correspond approximately to the axes 3, 1, and 2 respectively which were used for the scattered events. The second stage of the analysis was bypassed for the beam lambda calculations, since there was no recoil proton.

The beam lambdas were analyzed with respect to the z axis with and without the track separation cut in order to check the opening angle bias with better statistics. The resulting polarizations are shown in Figures 4.3(a) and 4.3(b). Again the track separation and cos θ^* distributions showed clearly the necessity of the track separation cut. Polarizations for the x and y directions of the analysis axis were calculated with the track separation cut. The resulting polarizations are shown in Figures 4.4(a) and 4.4(b).

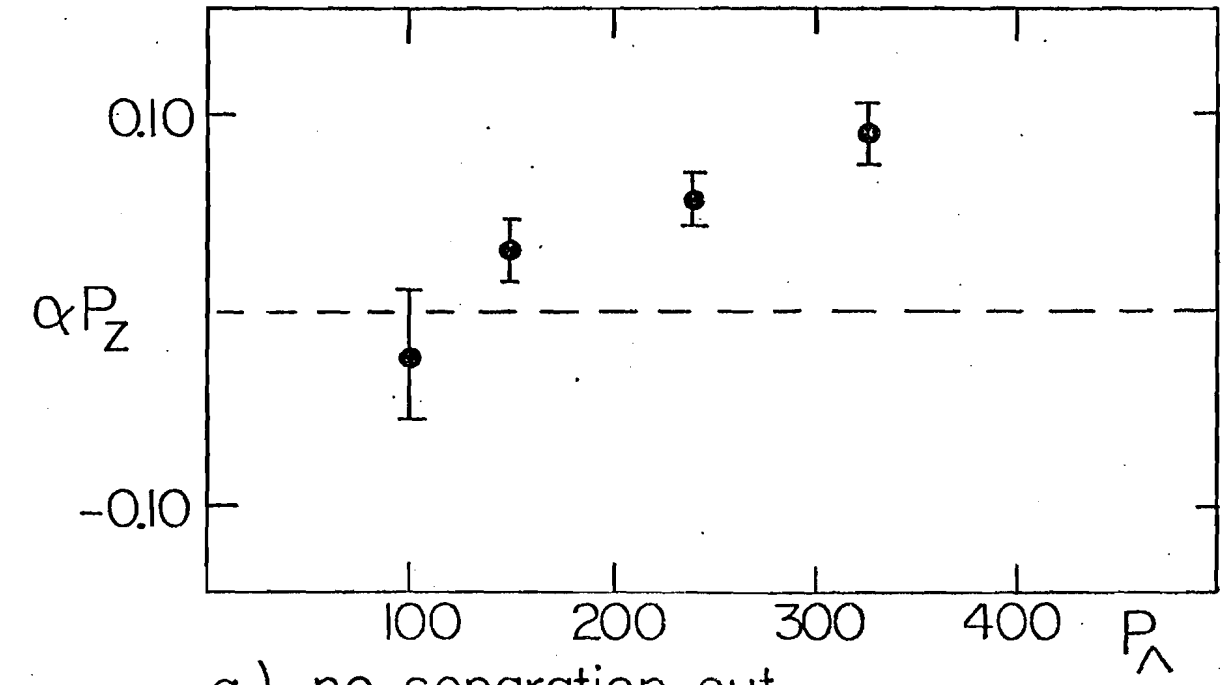

a.) no separation cut

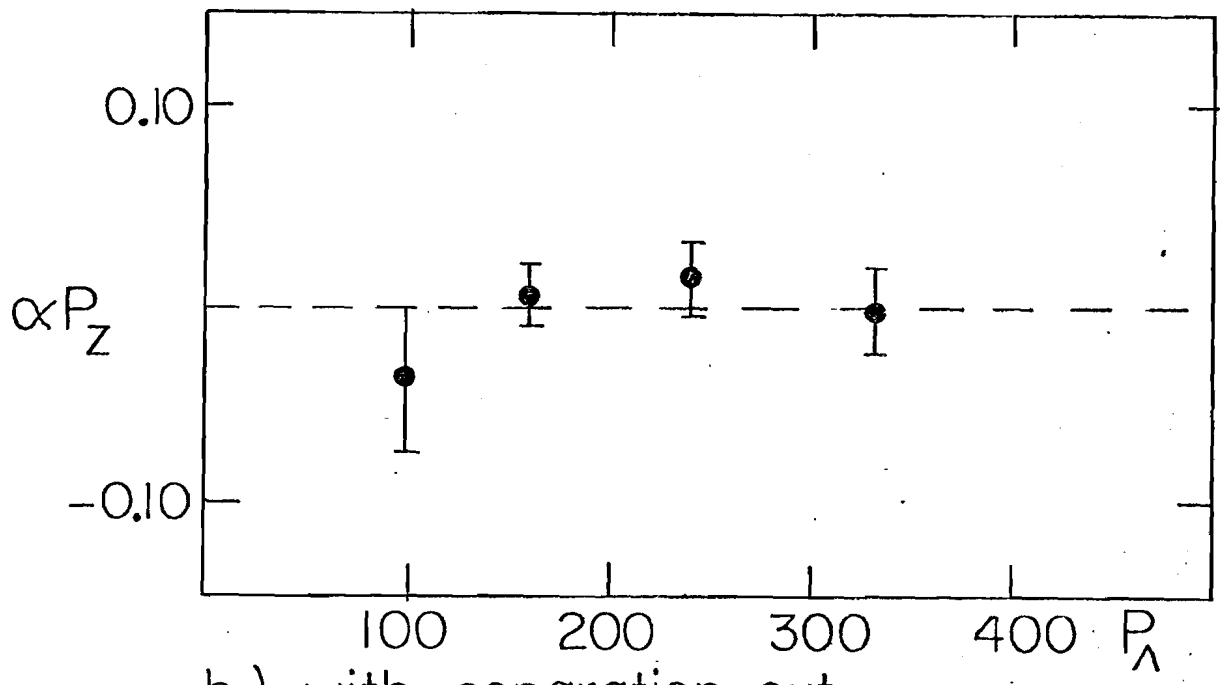

b.) with separation cut

Fig. 4.3

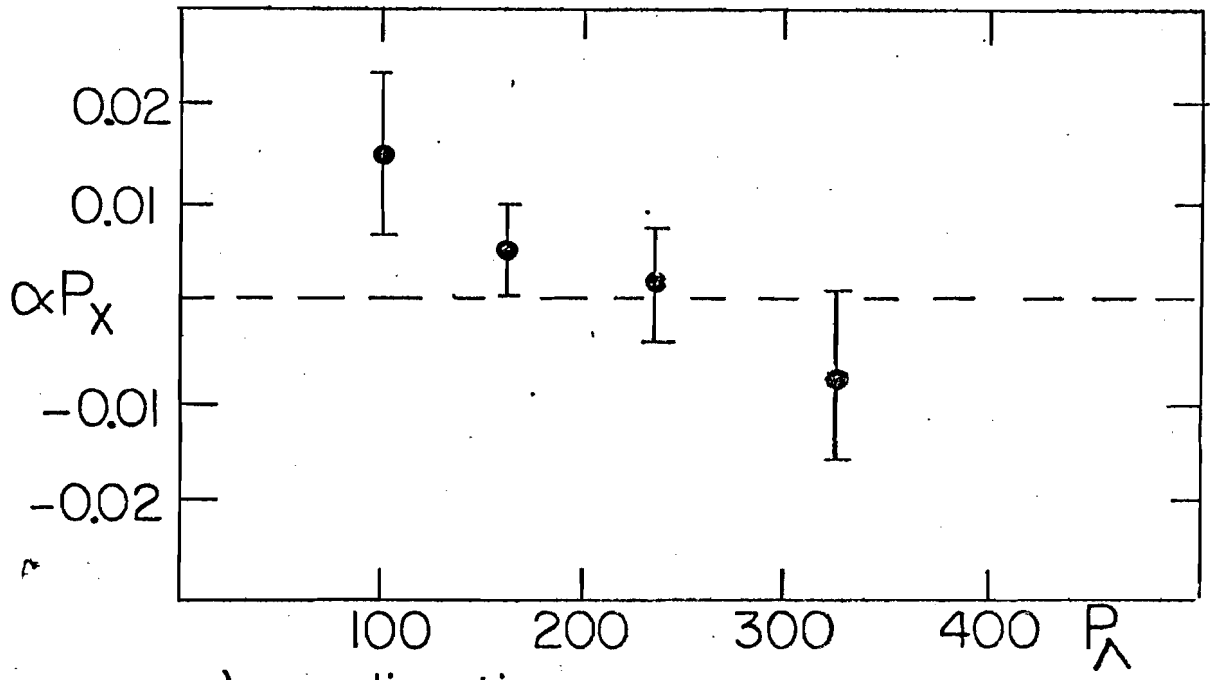

a.) x – direction

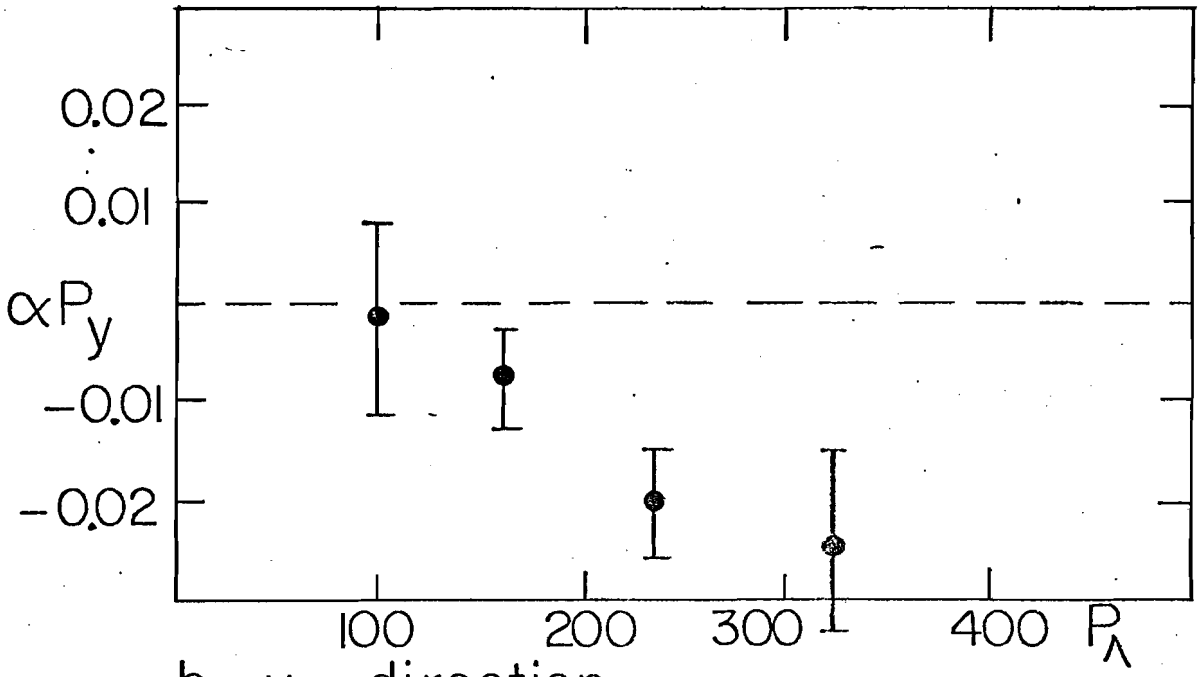

b. y – direction

Fig. 4.4

The beam lambdas showed no significant polarizations along the x or z axes with overall statistical uncertainties of ± 0.005. However, there was a small bias giving a vertical polarization signal which appeared to scale with the Λ momentum. It was therefore necessary to make a correction to the elastic polarizations along this direction. This correction was typically much smaller than the statistical uncertainties in the measured polarizations, because the direction of the normal to the scattering plane (which was approximately the $\pm y$-direction) reversed for left-scattered Λ's relative to right scattered Λ's. This correction is discussed further in Section 5.2.

CHAPTER 5

RESULTS

The measured values of the elastic scattering polarizations with respect to the three directions defined in Chapter 4 for lambda-p, K_s-p, and antilambda-p are presented in section 5.1. Results are given as a function of the incident momentum and of t of the scatter. Section 5.2 explains the corrections which were made to the data, and Section 5.3 contains the results of various bias checks which were made using the lambda-p elastic scattering data.

5.1 THE ELASTIC SCATTERING POLARIZATIONS

The lambda-p elastic scattering data was divided into four momentum bins and five t bins, as shown in Table 5.1. The measured polarizations for various combinations of these bins with respect to the parity allowed direction $\hat{p}_1 \times \hat{p}_3$ are shown in Figures 5.1(a)-5.1(f). The polarization is zero within errors everywhere except in the lowest momentum bins. Figure 5.1(f) shows data in the range $0.1 < |t| < 0.4$ as

Table 5.1

Binning Used for Elastic Scattering Data

Variable	Bin Boundaries	Average value of variable for data in bin
p_Λ	0 - 120 GeV/c 120 - 200 GeV/c 200 - 280 GeV/c 280 - 400 GeV/c	100 GeV/c 160 GeV/c 230 GeV/c 320 GeV/c
t	0.0 - 0.1 $(GeV/c)^2$ 0.1 - 0.2 $(GeV/c)^2$ 0.2 - 0.4 $(GeV/c)^2$ 0.4 - 0.8 $(GeV/c)^2$ > 0.8 $(GeVc)^2$	0.065 $(GeV/c)^2$ 0.14 $(GeV/c)^2$ 0.27 $(GeV/c)^2$ 0.50 $(GeV/c)^2$ 1.00 $(GeVc)^2$

Table 5.2
Parity Allowed Λ Polarizations for $.1 \leq |t| \leq .4$

p_Λ	P	χ^2 that P=0
100 GeV/c	-0.140 ± 0.040	12.2
160 GeV/c	-0.029 ± 0.017	2.9
230 GeV/c	-0.022 ± 0.018	1.5
320 GeV/c	$+0.010 \pm 0.028$	0.1

Parity allowed lambda polarizations

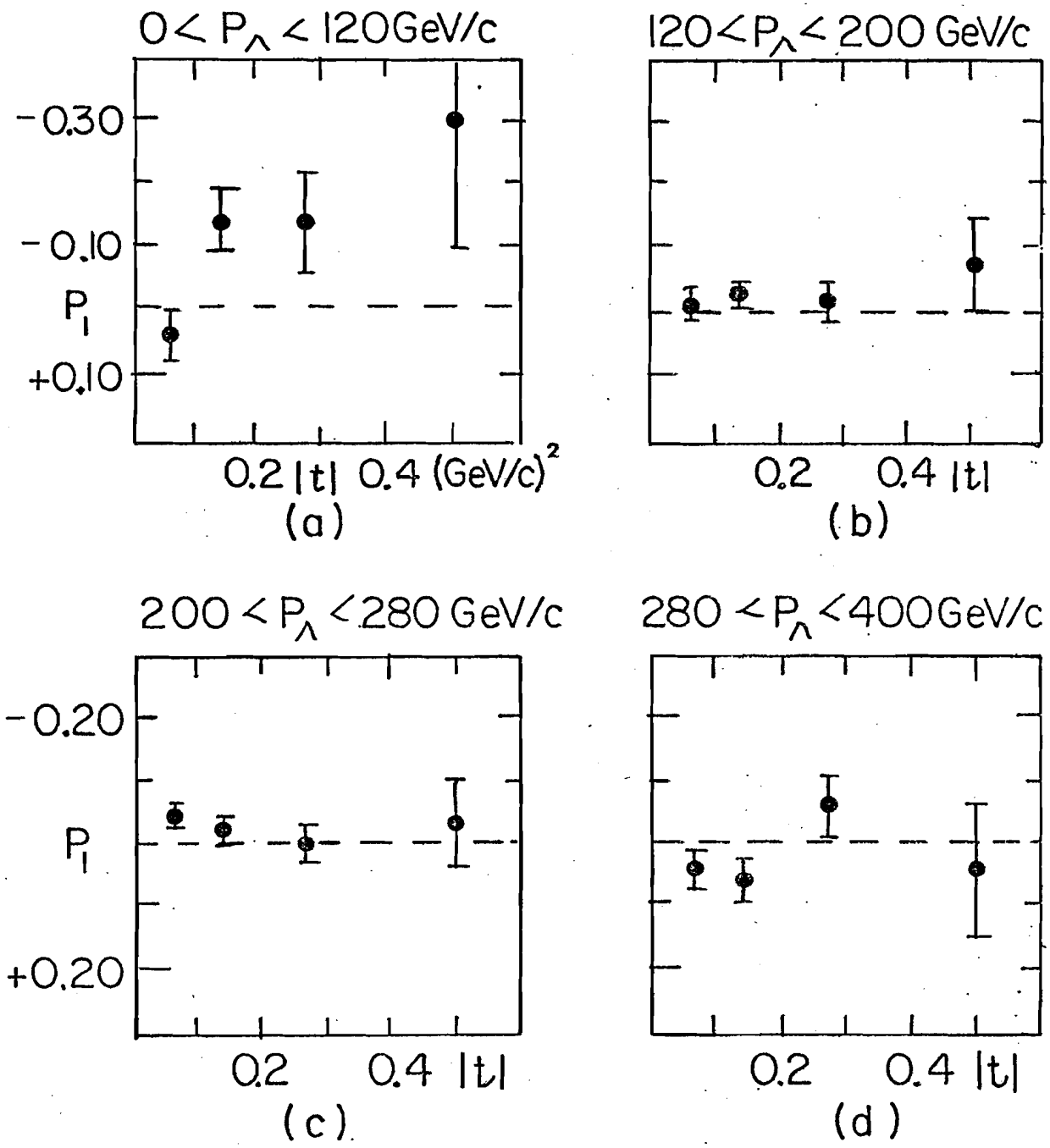

Fig. 5.1

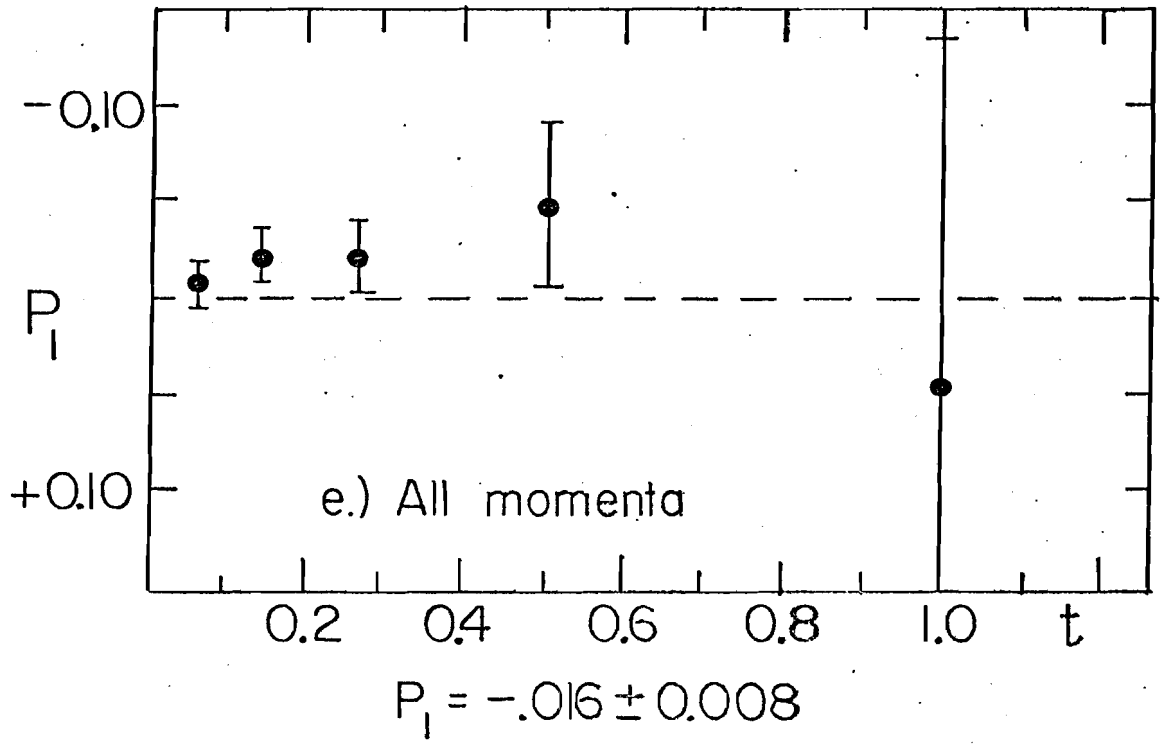

$P_1 = -.016 \pm 0.008$

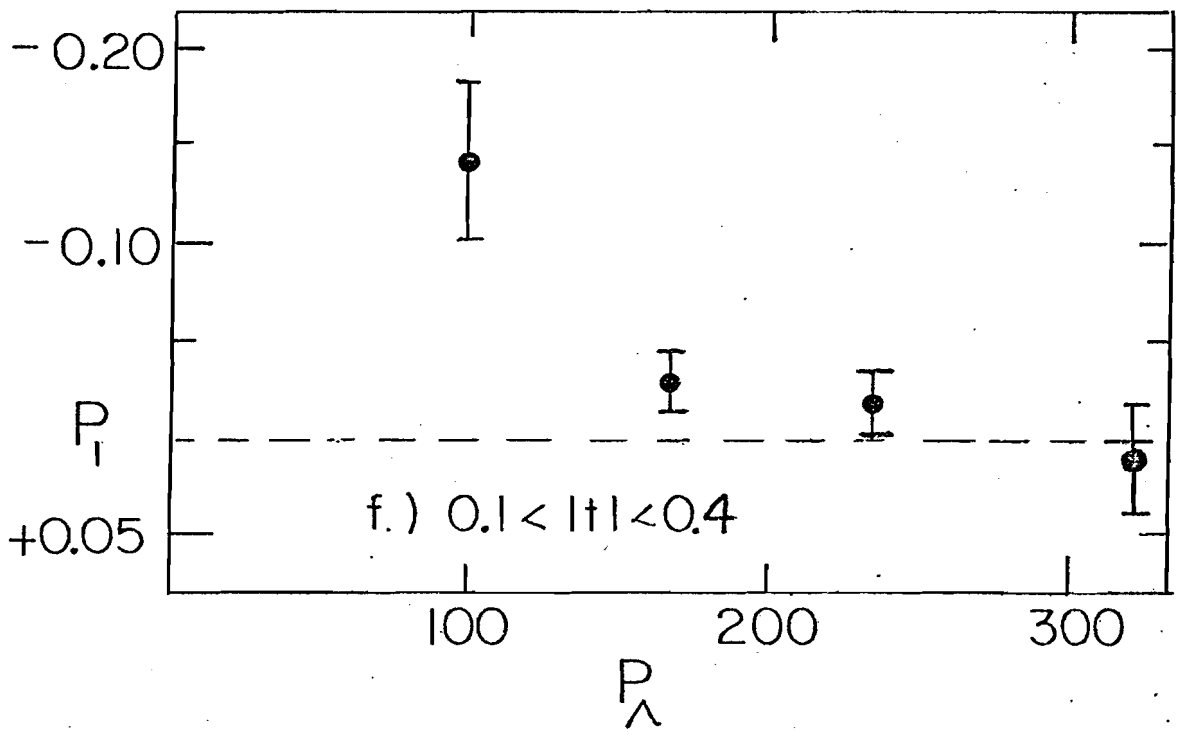

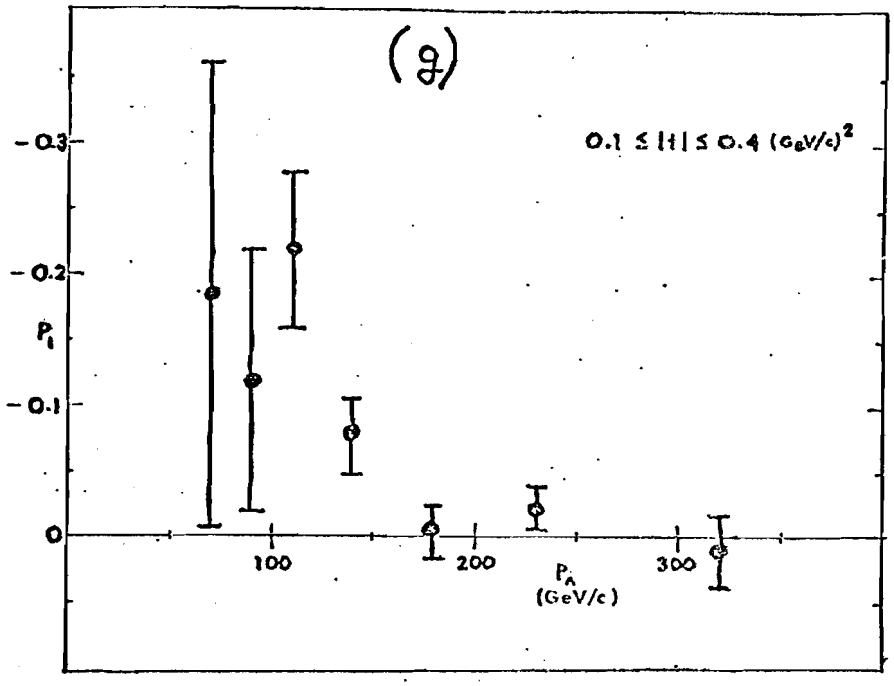
(g)
0.1 ≤ |t| ≤ 0.4 (GeV/c)²
-0.3
-0.2
-0.1
0
P_1
100
200
300
P_A
(GeV/c)

a function of momentum. The numerical values of the points and their errors are shown in Table 5.2. The points at 100 GeV/c and at 160 GeV/c are 3.4 and 1.7 standard deviations above P = 0. They show that for lambda momenta below 300 GeV/c there is a negative polarization. The magnitude of the polarization is seen to decrease as the momentum increases, as can be seen in Figure 5.1(f).

To investigate this effect further, finer binning in the momentum was done. The values which were obtained for the Λ-p polarizations are plotted in figure 5.1(g). This figure shows clearly that the results are not a function of the bin choices.

Polarization measurements with respect to the two parity violating directions are shown in Figures 5.2 and 5.3. All of these values for the polarization are consistent with zero. The numerical values for the lambda polarizations together with their errors and the χ^2 for the cos θ* fits are given in Table 5.3. The t-distribution, scattered lambda momentum distribution, recoil proton momentum distribution, and scattered lambda reconstructed invariant mass for the events submitted to the polarization analysis programs are shown in Figures 5.4 - 5.7, respectively.

The neutral beam contained a substantial sample of K_s. A measurement of the "polarization" for the decay

$$K_s \longrightarrow \pi^+ + \pi^-$$

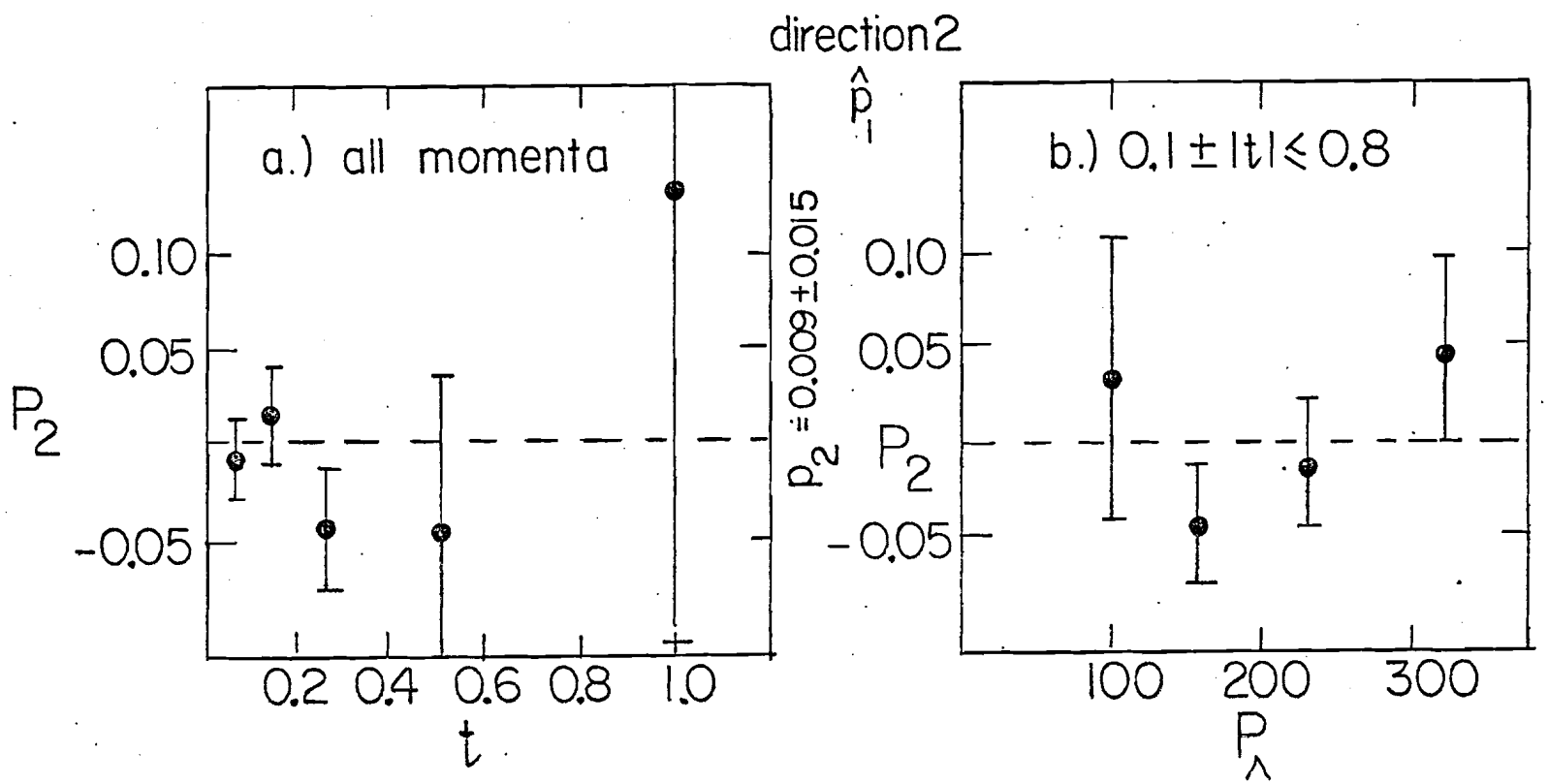
direction 2
$\hat{p}_1$
a.) all momenta
b.) $0.1 \pm |t| \leq 0.8$
$P_2 = 0.009 \pm 0.015$
P_2
0.10
0.05
-0.05
0.2
0.4
0.6
0.8
1.0
t
100
200
300
P_Λ

Fig. 5.2

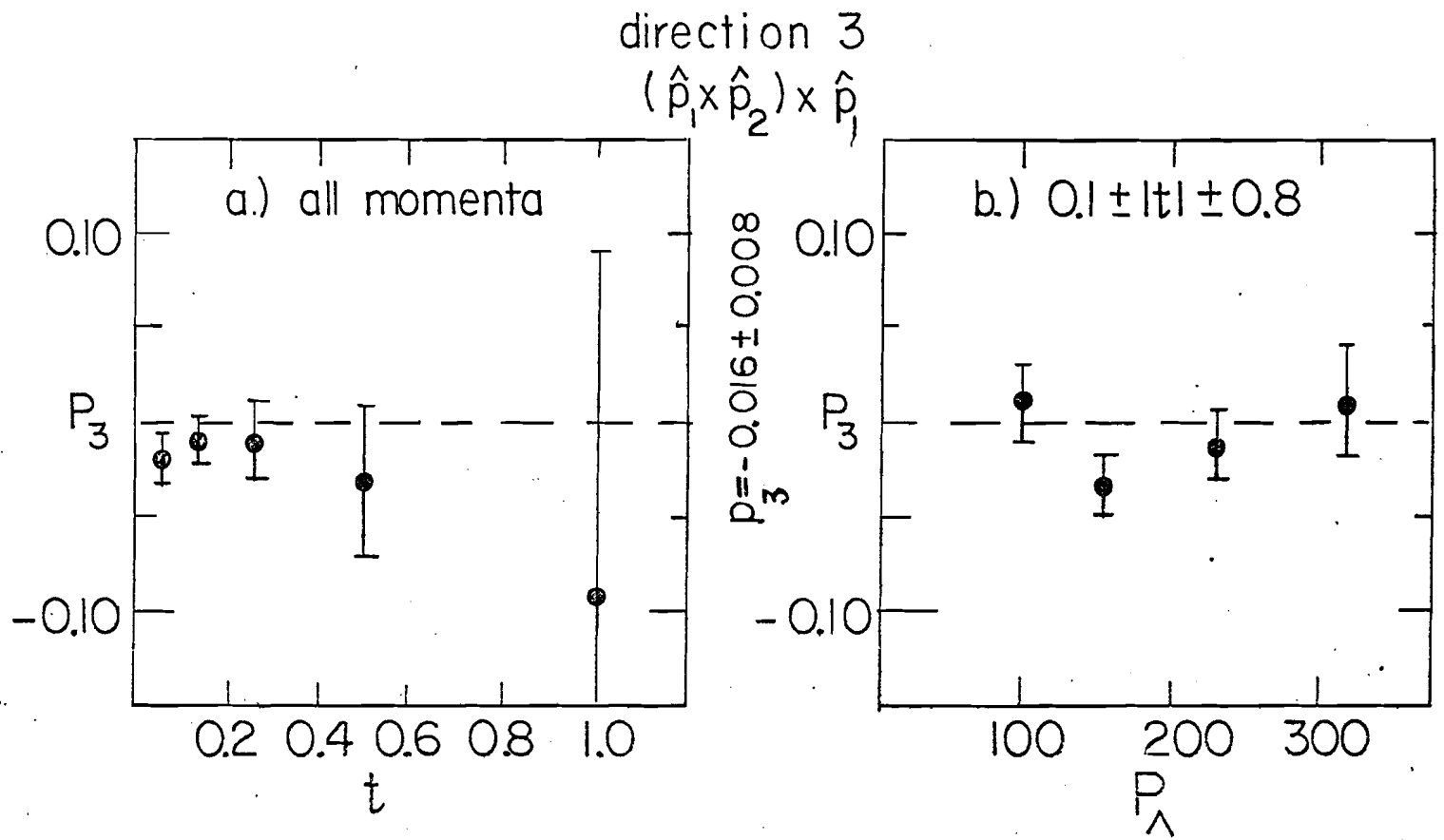
direction 3
$(\hat{p}_1 \times \hat{p}_2) \times \hat{p}_1$
a.) all momenta
b.) $0.1 \pm |t| \pm 0.8$
P_3
0.10
-0.10
0.2 0.4 0.6 0.8 1.0
t
100 200 300
P_Λ
$p_3 = -0.016 \pm 0.008$

Fig. 5.3

Table 5.3
Λ Polarizations

Note: Bracketed numbers give [chi-squared for cos θ* fit/D. F.].

Direction 1 $(\hat{p}_1 \times \hat{p}_3)$

p_Λ \ t	0-.1	.1-.2	.2-.4	.4-.8
100	.0481±.0423 [16.5/20]	-.1370±.0513 [16.2/20]	-.1396±.0813 [22.1/20]	-.3247±.2192 [12.2/18]
160	-.0126±.0192 [29.0433]	-.0343±.0213 [24.8/20]	-.0183±.0298 [22.2/20]	-.0832±.0703 [20.6/20]
230	-.0377±.0202 [12.4/20]	-.0296±.0227 [31.1/20]	-.0053±.0311 [28.1/20]	-.0327±.0685 [14.7/20]
320	.0361±.0304 [20.1/20]	.0500±.0349 [12.1/20]	-.0619±.0471 [24.4/20]	.0325±.1080 [24.2/20]

Direction 2 $(\hat{p}_1)$

p_Λ \ t	0-.1	.1-.2	.2-.4	.4-.8
100	-.1556±.0825 [10.5/15]	.2433±.1034 [21.5/14]	-.3461±.1498 [10.5/13]	-.3896±.3629 [8.3/12]
160	-.0274±.0355 [22.3/15]	-.0278±.0403 [21.8/15]	-.0944±.0544 [11.4/15]	-.0320±.1332 [7.5/13]
230	.0048±.0371 [29.0/15]	-.0096±.0417 [23.8/15]	-.0165±.0570 [20.7/15]	.0334±.1308 [16.2/13]
320	.0774±.0563 [10.9/15]	.0903±.0654 [4.9/15]	.0284±.0852 [19.4/15]	-.1482±.1808 [15.1/13]

Direction 3 $[(\hat{p}_1 \times \hat{p}_3) \times \hat{p}_1]$

p_Λ \ t	0-.1	.1-.2	.2-.4	.4-.8
100	-.0416±.0393 [8.3/20]	-.0114±.0496 [25.6/20]	.0685±.0781 [23.9/20]	.1176±.2387 [10.3/16]
160	-..0195±.0188 [14.6/20]	-.0359±.0210 [22.3/20]	-.0272±.0291 [20.3/20]	-.0002±.0706 [24.3/20]
230	-.0127±.0201 [11.2/20]	.0023±.0227 [25.2/20]	-.0232±.0312 [14.1/20]	-.0459±.0679 [15.9/20]
320	-.0298±.0304 [23.2/20]	.0199±.0351 [11.2/20]	.0202±.0468 [23.5/20]	.0889±.1082 [16.5/20]

Table 5.3
(continued)

Combined Results

p_Λ < 200 GeV/c

Dir \ t	0-.1	.1-.2	.2-.4	.4-.8	>.8
1	-.0042±.0175	-.0493±.0196	-.0325±.0280	-.0695±.0668	-.18±.39
2	-.0474±.0376	.0080±.0376	-.1005±.0538	-.0743±.1250	.40±.43
3	-.0236±.0170	-.0321±.0193	-.0156±.0272	.0091±.0679	-.70±.3

p_Λ > 200 GeV/c

1	-.0197±.0168	-.0067±.0190	-.0232±.0260	-.0152±.0578	.10±.22
2	.0267±.0309	.0193±.0352	-.0026±.0474	-.0306±.0474	.05±.28
3	-.0179±.0168	.0076±.0190	-.0099±.0260	-.0580±.0575	.14±.22

All Momenta

Dir \ t	0-.1	.1-.2	.2-.4	.4-.8	>.8
1	-.0175±.0122	-.0267±.0138	-.0269±.0190	-.0532±.0437	.05±.19 [14.6/19]
2	-.0083±.0224	.0141±.0257	-.0454±.0355	-.0481±.0808	.14±.25 [26.2/1
3	-.0207±.0119	-.0121±.0136	-.0125±.0189	-.0300±.0439	-.09±.19 [12.8/18]

All t values

Dir \ p_Λ	0-120	120-200	200-280	280-400
1	-.0503±.0300	-.0235±.0127	-.0313±.0133	.0226±.0202
2	-.0232±.0624	.0402±.0236	-.0031±.0246	.0626±.0372
3	-.0148±.0284	-.0260±.0125	-.0107±.0133	-.0059±.0202

Direction 1 P =-.0179±.0080

Direction 2 P =-.0085±.0150

Direction 3 P =-.0165±.0080

Λp elastic scattering

Fig. 5.4

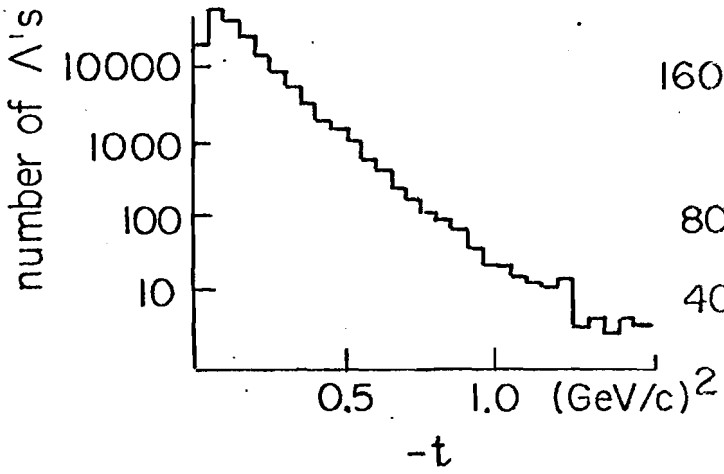

Fig. 5.5

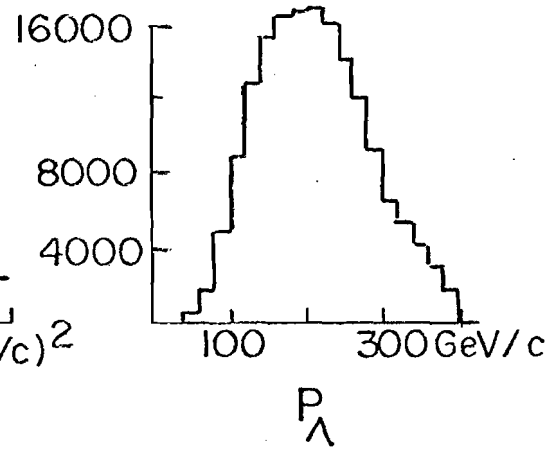

162813 events

Fig. 5.6

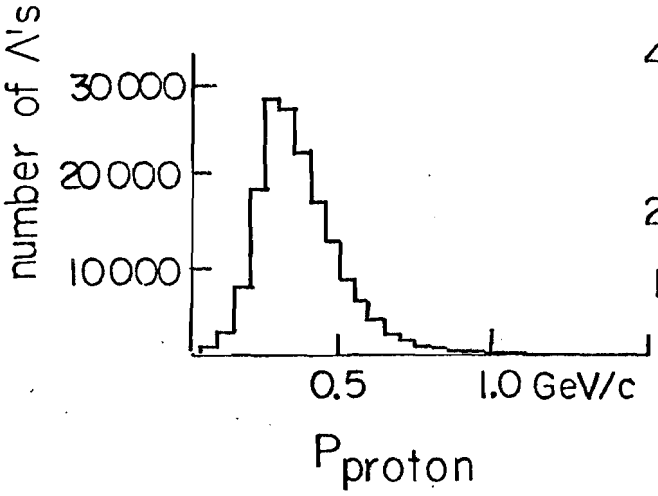

Fig. 5.7

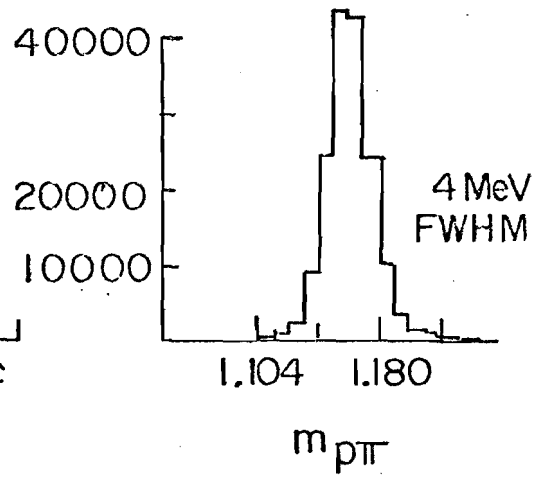

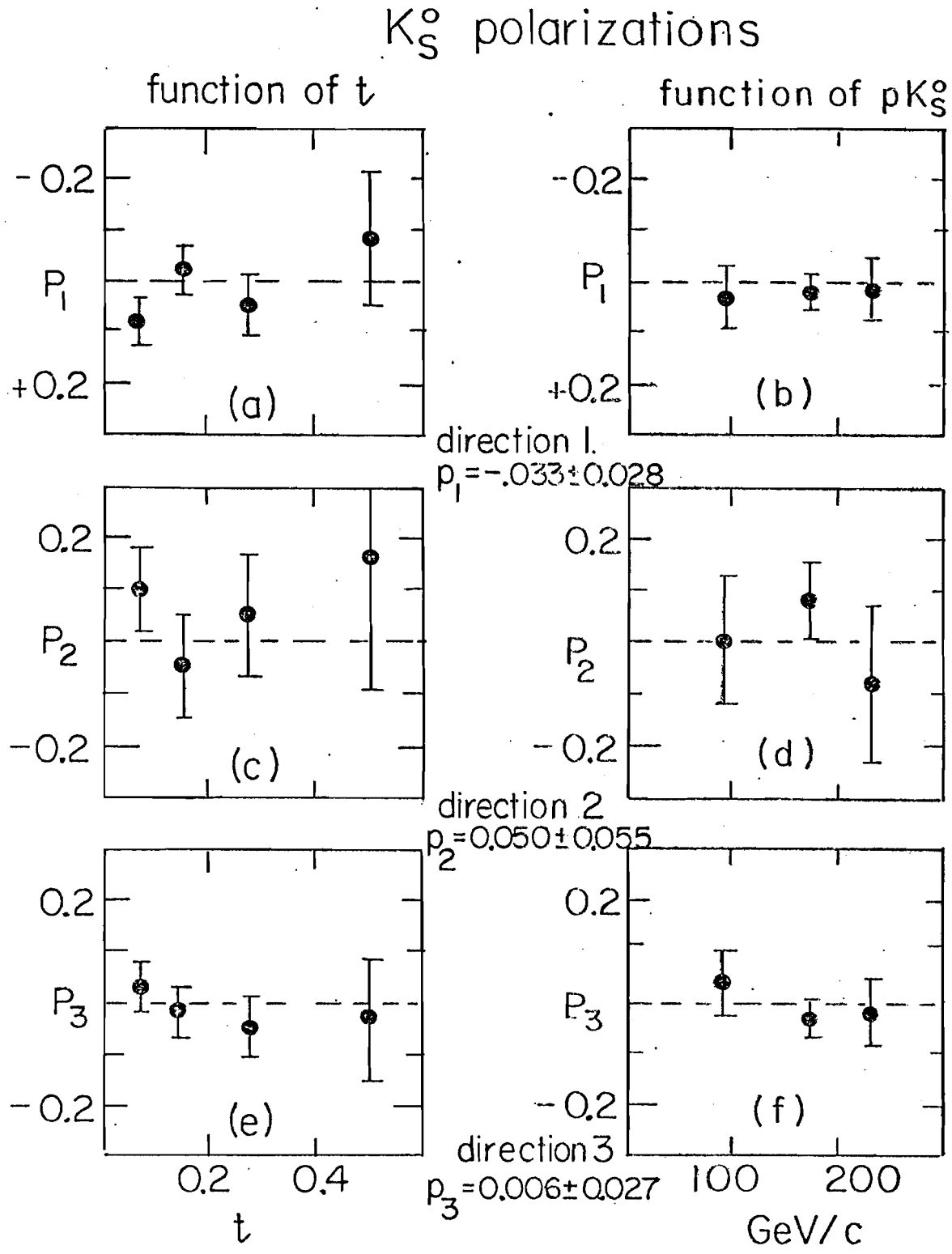
K_S^o polarizations
function of t
function of pK_S^o
-0.2
P_1
+0.2
(a)
(b)
direction 1.
p_1=-.033±0.028
0.2
P_2
-0.2
(c)
(d)
direction 2
p_2=0.050±0.055
0.2
P_3
-0.2
(e)
(f)
direction 3
p_3=0.006±0.027
0.2
0.4
t
100
200
GeV/c

Fig.5.8

gave an additional measurement of any apparatus or software biases. The K_S "polarization" must be zero since it is spinless. Measured values of the K_S "polarizations" with respect to the three axes are shown in Figure 5.8. All of these measurements are consistent with zero at a level of 10%. For instance, the measured polarization P_1 for $p_K \leq 120$ GeV/c in the t-interval $0.1 \leq |t| \leq 0.4$ $(\text{GeV/c})^2$ is $P_1 = +0.01 \pm 0.09$. Distributions of t, scattered K_S momentum, recoil proton momentum, and the K invariant mass are shown for the K_S-p scattering data in Figures 5.9 - 5.12, respectively. The K_S sample was found to have a significant contamination of lambdas at high momenta. This contamination of lambdas was eliminated by making a cut in cos θ and allowing only events with

$$\cos \theta^* < 0.$$

Numerical results for the K_S "polarizations", their errors, and the χ^2 for the cos θ^* fits are given in Table 5.4.

The neutral beam contained a small sample of antilambdas. A total of 1367 antilambda-p elastic scatters was detected. Polarization measurements with respect to the three axes are presented in Figures 5.13(a) - 5.13(f). None of the points is significantly different from zero. Distributions of t, antilambda momentum, recoil proton momentum, and antilambda reconstructed mass are given in Figures 5.14 - 5.17, respectively. Numerical results for the antilambda polarizations, their errors, and the χ^2 for the cos θ^* fits are given in Table 5.5.

$K_s^o p$ elastic scattering

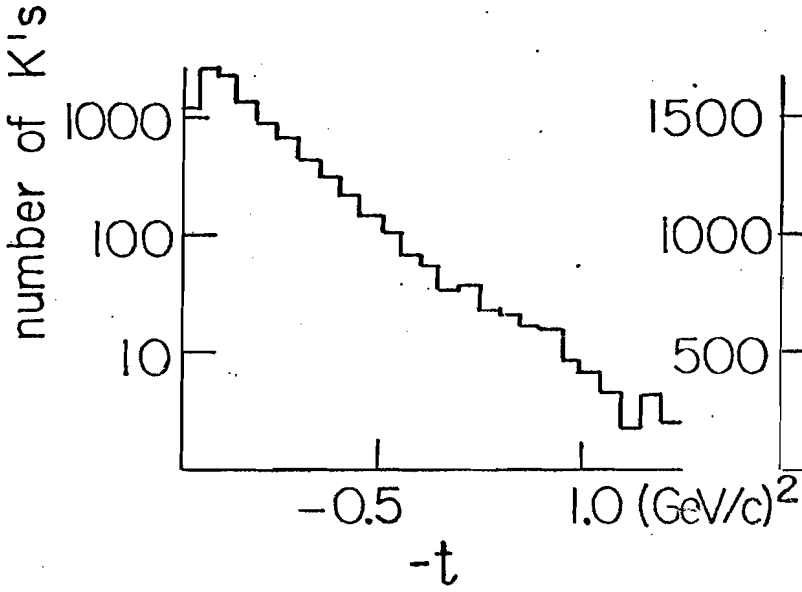

Fig. 5.9

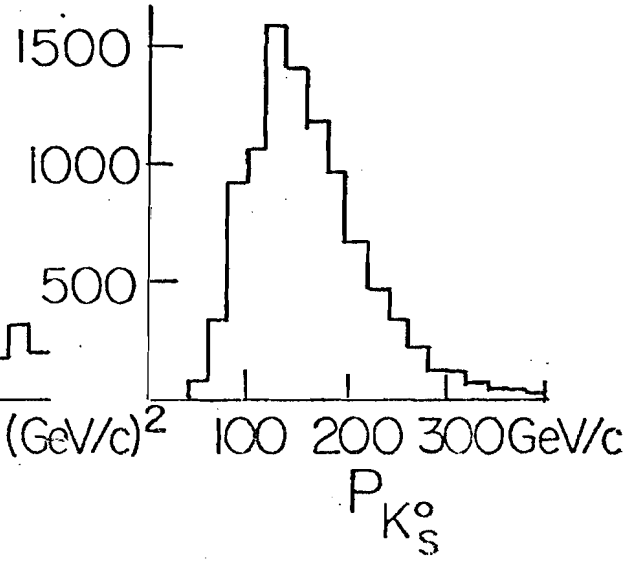

Fig. 5.10

9694 events

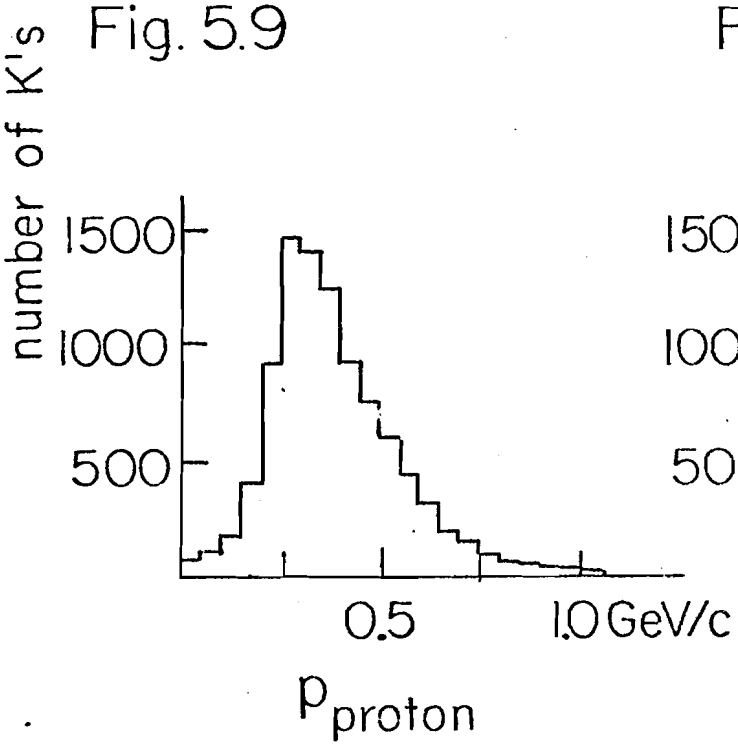

Fig. 5.11

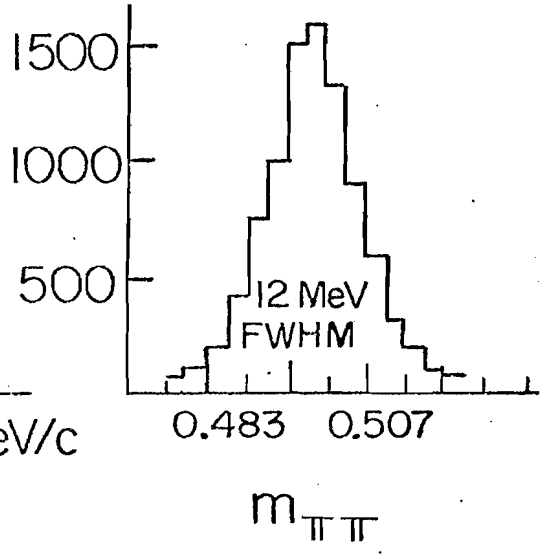

Fig. 5.12

Table 5.4
K_S^0 Polarizations

Note: Bracketed numbers give [chi-squared for cos θ* fit/D. F.].

$p_K < 120$

Dir \ t	0-.1	.1-.2	.2-.4	.4-.8
1	.1171±.0974	-.1001±.1133	.1983±.1492	-.42±.27
	[16.6/20]	[9.8/20]	[21.5/20]	[2.0/ 2]
2	.0034±.1885	-.1536±.2400	.1621±.240	
	[17.2/11]	[13.4/11]	[14.7/11]	
3	-.0053±.0949	-.0142±.1032	-.1285±.133	.39±.26
	[14.0/20]	[51.0/20]	[10/17]	

$120 < p_K < 200$

Dir \ t	0-.1	.1-.2	.2-.4	.4-.8
1	.0284±.0566	.0066±.0608	.0207±.0764	.0803±1570
	[25.2/20]	[21.8/20]	[15.3/20]	[5.7/18]
2	.1667±.0964	-.0783±.1315	.0349±.1500	.1605±.2750
	[9.1/11]	[36.5/11]	[8.4/11]	[8.7/11]
3	.0086±.0559	-.0136±.0620	-.0944±.0760	-.1139±.1361
	[31.6/20]	[18.9/20]	[13.9/20]	[9.5/17]

$200 < p_K < 280$

Dir \ t	0-.1	.1-.2	.2-.4	.4-.8
1	.2059±.1080	-.0368±.1198	.0513±.1477	.0513±.2360
	[14.1/19]	[21.6/19]	[16.0/16]	[3.7/3]
2	-.4647±.2880	.1216±.2200	-.0667±.3400	
	[11.5/10]	[4.7/10]	[4.3/10]	
3	.0688±.1039	-.0075±.1151	-.1707±.1407	-.1308±.2460
	[23.2/20]	[19.1/20]	[7.7/13]	[2.3/3]

$280 < p_K < 400$

Dir \ t	0-.1	.1-.2	.2-.4	.4-.8
1	.2151±.2700	.044±.283	-.16±.40	
2	.410±.34			
3	.517±.289		.459±.41	

Combine p_K

Dir \ t	0-.1	.1-.2	.2-.4	.4-.8
1	.081±.044	-.019±.048	.051±.061	-.079±.131
2	.099±.080	-.047±.102	.052±.119	.161±.269
3	.028±.043	-.013±.048	-.052±.059	-.030±.108

Combine t

Dir \ p_K	0-120	120-200	200-280
1	.031±.064	.022±.035	.016±.068
2	.004±.126	.077±.067	-.081±.154
3	.040±.060	-.029±.035	-.020±.065

Combined Results

Direction 1 P = .033 ± .028
Direction 2 P = .050 ± .055
Direction 3 P = -.006 ± .027

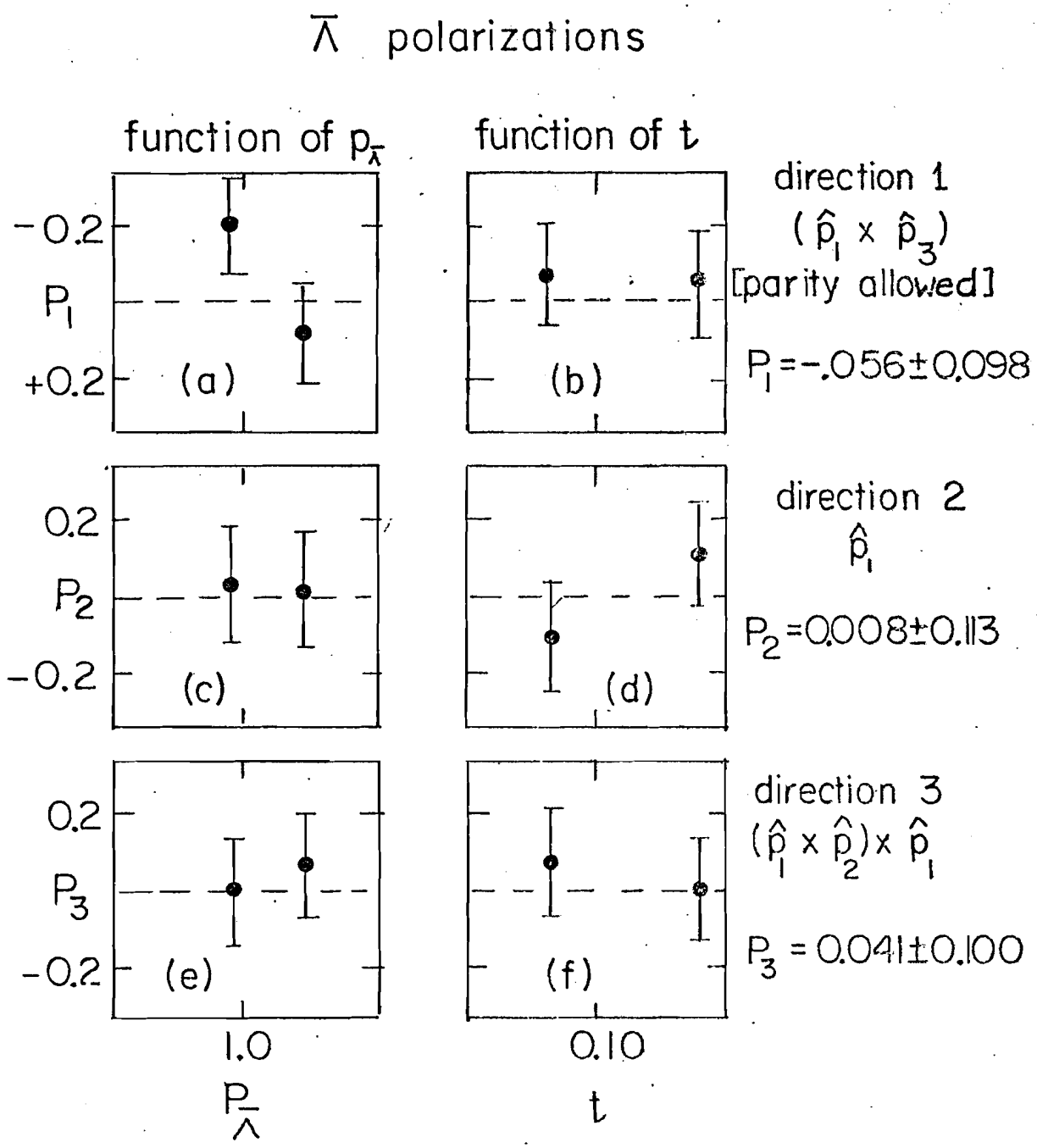
$\bar{\Lambda}$ polarizations
function of $p_{\bar{\Lambda}}$
function of t
direction 1
$(\hat{p}_1 \times \hat{p}_3)$
[parity allowed]
$P_1 = -.056 \pm 0.098$
direction 2
$\hat{p}_1$
$P_2 = 0.008 \pm 0.113$
direction 3
$(\hat{p}_1 \times \hat{p}_2) \times \hat{p}_1$
$P_3 = 0.041 \pm 0.100$
-0.2
P_1
+0.2
0.2
P_2
-0.2
0.2
P_3
-0.2
(a)
(b)
(c)
(d)
(e)
(f)
1.0
$P_{\bar{\Lambda}}$
0.10
t

Fig. 5.13

$\bar{\Lambda}p$ elastic scattering

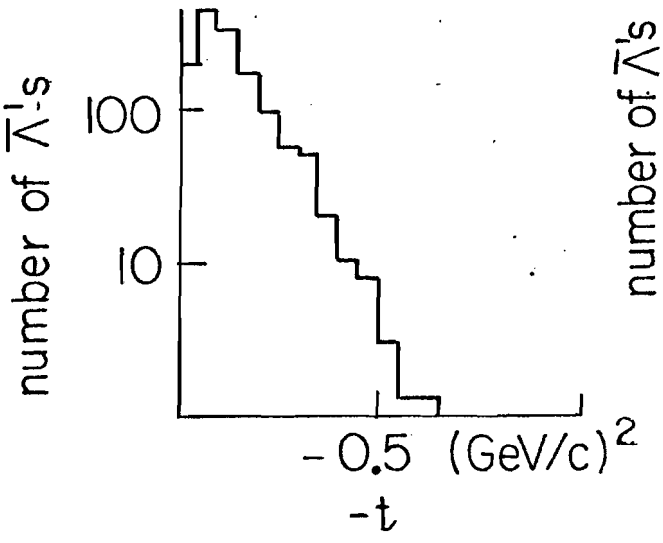

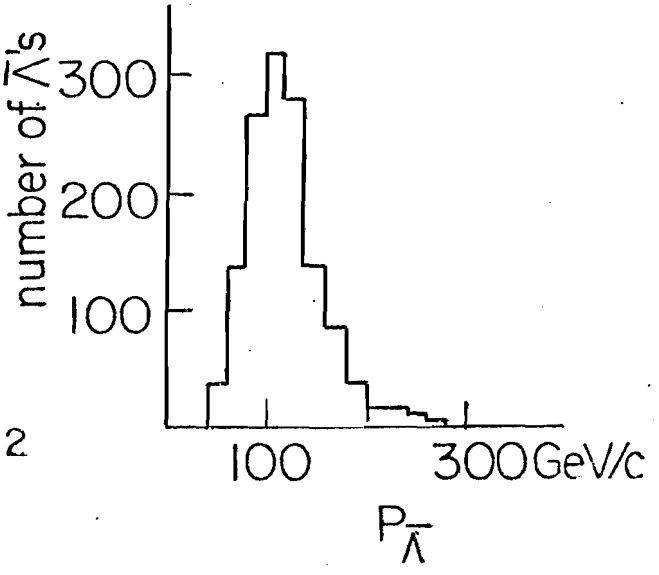

1367 events

Fig. 5.14

Fig. 5.15

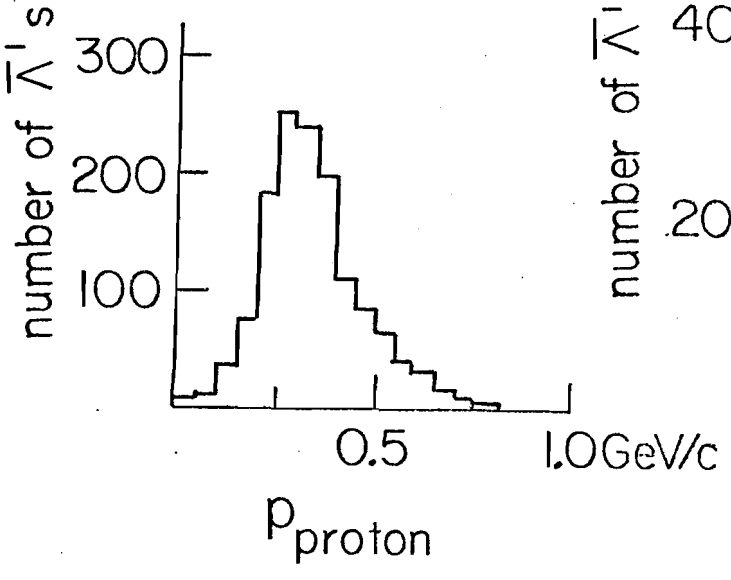

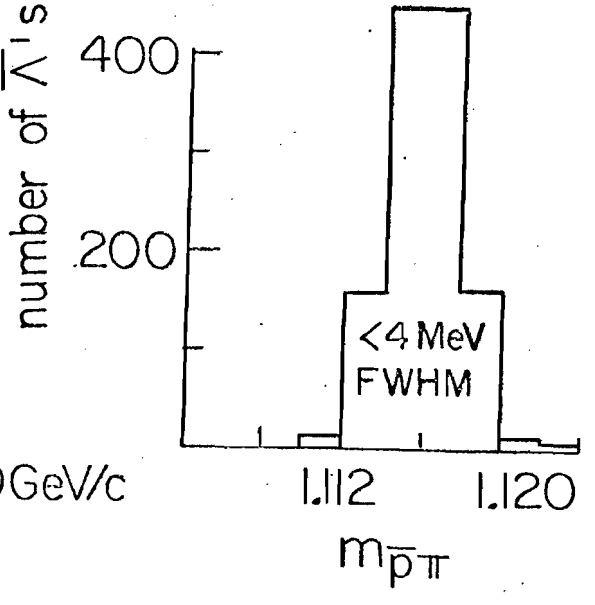

Fig. 5.16

Fig. 5.17

Table 5.5
$\bar{\Lambda}$ Polarizations

Note: Bracketed numbers give [chi-squared for cos θ* fit/D. F.].

Function of $p_{\bar{\Lambda}}$ ($\bar{t}$ = .117)

Dir \ $p_{\bar{\Lambda}}$	0-120 (95)	120-200 (145)	>200 (230)
1	.2019±.1413 [32.9/40]	-.0779±.1357 [23.8/42]	-.23±.43
2	-.0331±.1651 [40.8/33]	-.0145±.1539 [23.3/37]	
3	-.0056±.1507 [32.1/41]	-.0683±.1337 [30.5/41]	

Function of t ($\overline{p_{\bar{\Lambda}}}$ =119 GeV/c)

Dir \ t	0-.1 (.06)	.1-.4 (.18)
1	.0618±.1376	.0509±.1394
2	.1128±.1563	-.1057±.1621
3	-.0753±.1369	-.0011±.1464

Combined Results

Direction 1 P = .0564 ± .0978
Direction 2 P = -.0076 ± .1125
Direction 3 P = -.0406 ± .1000

Table 5.6
Data Comparisons; Bias Checks
χ^2 given is that testing the hypothesis that the data subsets being compared are equivalent.

Nature of the Comparison	N (D.F.)	χ^2
Arm 1 vs. Arm 2 (Recoil proton in C1,C2 or C3,C4)	16	10.39
300 GeV vs. 400 GeV inc. protons	16	18.41
Avis(+) vs. Avis(-) (Arms combined)	16	10.37
Avis(+) vs. Avis(-) (Arm 1 only)	15	18.76
Avis(+) Arm 2 vs. Avis(-) Arm 1	15	17.29
Avis(+) vs. Avis(-) (Arm 2 only)	15	13.92
Avis(+) Arm 1 vs. Avis(-) Arm 2	16	11.26
Avis(+) vs. Avis(-) Each Arm Contributing Independently	46	44.51
Events Scattered Up vs. Events Scattered Down	15	6.04

5.2 CORRECTIONS TO THE DATA

As was mentioned in Chapter 4, the unscattered lambdas showed a bias in the y-direction. This bias is shown in Figure 4.4(b). Combining all data points in this figure gives a signal of -0.02 ± 0.005 at an average Λ momentum of 200 GeV/c. The correction to the data was computed assuming that the size of the bias scaled linearly with the lambda momentum. Since the normal to the scattering plane reversed for right-scattered Λ's relative to left-scattered Λ's, the sign of the correction reversed for one set of data relative to the other. In fact, the correction would be zero if there were equal numbers of right and left-scattered Λ's. The ratio of left-scattered Λ's to right-scattered Λ's in the data sample was 0.588:1.00, however, so the net correction to the parity allowed component of the lambda polarization was taken to be

$$-0.000024\ p_{inc}$$

where $p_{\Lambda inc}$ was the incident Λ momentum in GeV/c. This number also includes an azimuthal correction of 0.94 which corrects for the fact that the normal to the scattering plane is not always exactly parallel to the y-axis. The net correction at 200 GeV/c, for instance, was +0.0048. The only data affected by this correction were the parity-allowed lambda polarizations.

5.3 BIAS CHECKS

The chamber fits and the cos θ^* fits revealed no significant biases in any of the data which was processed. In fact, the data appeared to be remarkably clean. The possibility remained, however, that there were small biases in the data caused by asymmetries in the physical dimensions or in the detection efficiencies of the experimental apparatus. Several features of the apparatus were useful for checking the elastic scattering data for biases of this type. The recoil protons were detected in MWPC's which were located on both sides of the liquid hydrogen target. The spectrometer magnet M2 was run at both polarities. The incident proton beam was directed onto the production target T at momenta of 300 GeV/c and 400 GeV/c. All of these provided natural divisions for the lambda-p elastic scattering data.

A χ^2-test was used to check the various divisions of the data sample for systematic biases. The events in each subdivision of the data (e.g. M2(+) data vs. M2(-) data) were binned in momentum and in t. The weighted average of the polarization measurements in corresponding bins (e.g. [M2(+) p <120, t<0.1] and [M2(-) p <120, t<0.1]) was calculated, and a contribution to the overall χ^2 was computed which was given by:

$$\chi^2_i = [([\alpha P]_i - \overline{\alpha P_i})/\Delta(\alpha P)_i]^2 \qquad (5.1)$$

where $[\alpha P]_i$ was the individual measurement, $\overline{\alpha P_i}$ was the

weighted average, and $\Delta(\alpha P)_i$ was the error associated with $[\alpha P]_i$. The overall χ^2 was given by $\chi^2 = \sum_i \chi^2_i$. The number of degrees of freedom was given by the total number of bins used in the comparisons minus the number of weighted averages which were computed. The results for various divisions of the data are given in Table 5.6. No significant biases were uncovered.

Another possible origin of a bias in the data was the spectrometer magnet M2. It was discovered that there were small variations with time in the value of the field integral in M2 of order 1% or less which would cause small errors in the momentum of the decay products of the scattered particle. To check the effect of this possible bias, identical sets of elastic scattering data were analyzed with the proper value of the field integral in M2, and with a value different from the correct value by 1%. The calculated polarizations were not affected significantly by this change, indicating that the calculated polarizations were not biased by the uncertainties in the field integral.

Finally, it was conceivable that the polarization calculation was dependent upon the cuts which were made on events by the acceptance program. To check this, identical sets of events were analyzed with the standard acceptance program and with a modified acceptance program which had all of its cuts tightened by 20%, thus reducing the accepted fiducial volumes by 20% in each dimension. The calculated

polarizations were insensitive to this change in the fiducial volumes.

CHAPTER 6

CONCLUSIONS

The lambda polarization for lambda-p elastic scattering has been measured in the region:

$$0 < |t| < 1.5 \ (\mathrm{GeV/c})^2$$

$$60 < p_\Lambda < 400 \ \mathrm{GeV/c}$$

A total of 162,813 events was observed. This was the first high statistics polarization measurement of a high energy elastic scattering polarization of two nonidentical baryons. The lambda polarization is nonzero and negative at the lowest energies accessible to the experiment ($p_\Lambda = 100$ GeV/c). As the energy increases, the polarization decreases steadily and is consistent with zero through most of the energy region studied. This behavior is in general agreement with theoretical expectations and with experimental results for other scattering processes (including pp elastic scattering). The magnitude of the polarization is surprizingly large, however, at the lowest momenta which were examined.

Two parity violating components of the lambda elastic scattering polarization were also measured. The results were consistent with zero through the entire energy region studied.

A sample of 13,365 K_S-p elastic scatters was observed and processed by the polarization programs. The results were consistent with zero, as expected for a spinless particle.

A sample of 1367 antilambda-p elastic scatters was also observed and analyzed. The polarization was consistent with zero over the momentum interval of $60 < p < 250$ GeV/c.

The transversity representation gives the clearest physical picture of the amplitude structure of the polarizarion P. In this representation, the polarization is given by

$$P \frac{d\sigma}{dt} = 1/2\ \mathrm{Re}[(G_{++++} + G_{----})(G_{++++}^* - G_{----}^*)] + 1/2\ \mathrm{Re}[(G_{+-+-} + G_{-+-+})(G_{+-+-}^* - G_{-+-+}^*)]$$

The polarization is identically zero at $t=0$, because of relations (2.50) and (2.51) which are a result of angular momentum conservation. The data away from $t=0$ is shown in Figure 5.1(f). The behavior of the polarization is not surprising. The magnitude of P decreases steadily as the energy increases. In fact, the value of P is consistent with zero over most of the lambda momentum region investigated. In this region we see that

$$1/2\ \mathrm{Re}[(G_{++++} + G_{----})(G_{++++}^* - G_{----}^*) +$$

$$(G_{+-+-} + G_{-+-+})(G_{+-+-}{}^{*} - G_{-+-+}{}^{*})] = 0$$

This relation provides evidence in favor of the hypothesis that spin dependent forces vanish as the energy of the interaction increases. One possibility is that, as the energy rises, $G_{++++} \longrightarrow G_{----}$ and $G_{+-+-} \longrightarrow G_{-+-+}$.

The existence of polarizations in Λ-p elastic scattering of -0.22 ± 0.06 at 110 GeV or even -0.08 ± 0.03 at 140 GeV (see Figure 5.1(g)) at an average value $t = -0.2(\mathrm{GeV}/c)^2$ is quite unexpected and remains difficult to understand. One would expect Λ-p polarization to differ only slightly from the p-p elastic polarizations which are shown in Figure 6.1. The observed Λ-p polarizations are an order of magnitude larger, however. Several possible explanations for this difference can be mentioned:

1. The presence of the strange quark in the Λ breaks SU_3 symmetry in a strongly spin dependent way.

2. Some cancellation of amplitudes suppresses the spin flip amplitude in p-p elastic scattering, but allows it to be large in the case of Λ-p.

3. The experimental result may be incorrect due to a statistical fluctuation or to some undetected systematic error.

In any case the effect is sufficiently interesting that confirmation should be sought. The experiment should be

p-p Polarizations at $t = -0.3\ (\mathrm{GeV}/c)^2$

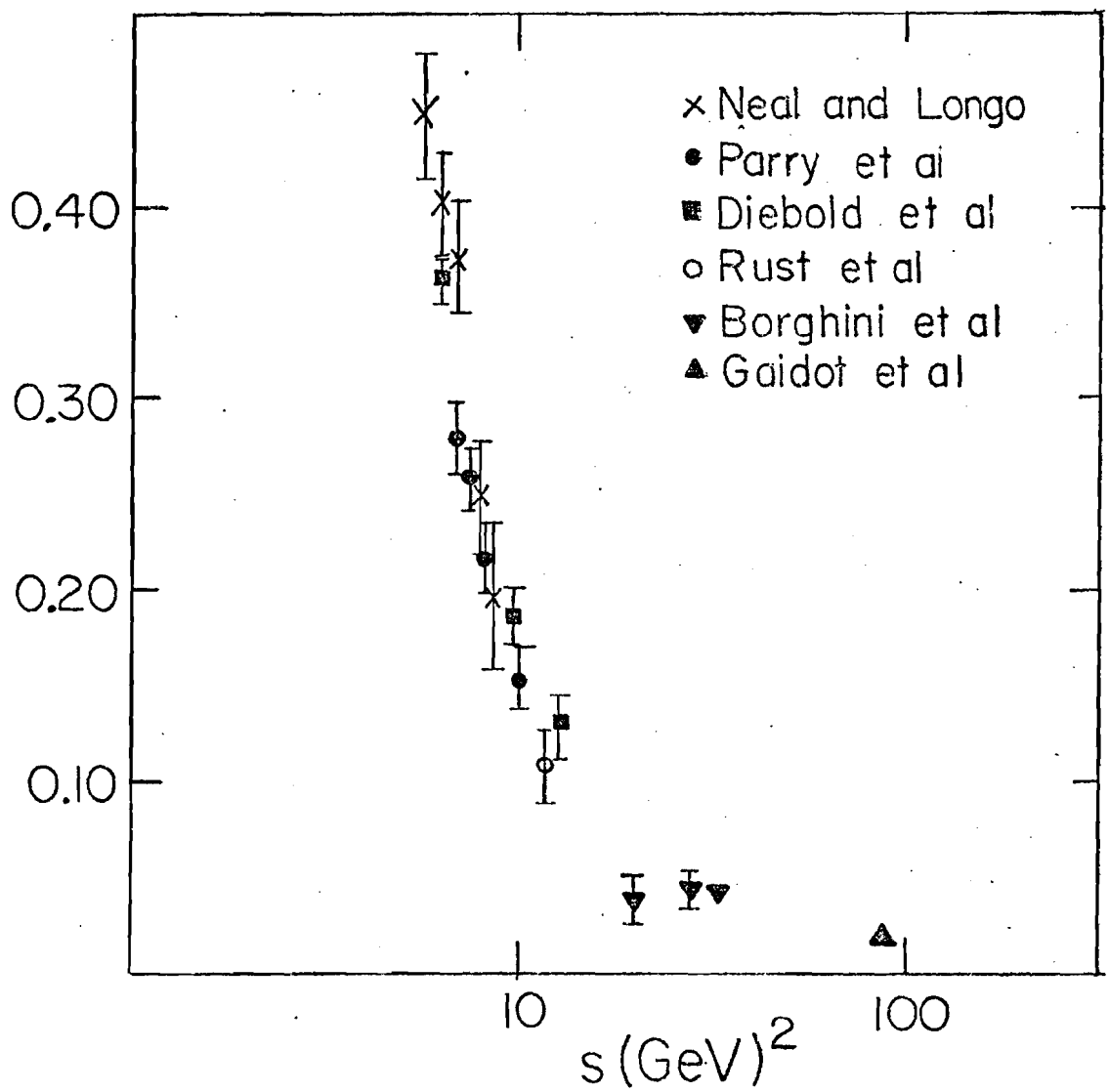

Fig. 6.1

repeated with an apparatus optimized for the lower energies which were observed in this experiment. Another possibility is to use a beam of polarized lambdas and measure the assymetry in the angular distribution in a plane perpendicular to the polarization of the incident beam.

It is also tempting to make a comparison of the elastic polarization data with the inclusive lambda polarization data [40] which is shown in Figure 6.2. The inclusive data shows a significant, non-zero polarization which is a function of p_t (or t), but not of the lambda momentum. On the other hand, the elastic scattering data suggests a polarization which depends upon the lambda momentum. This type of comparison is of rather limited value, however, because the two reactions involved,

$$p + Be \rightarrow \Lambda + X$$

and

$$\Lambda + p \rightarrow \Lambda + p$$

are quite different. The first reaction is dominated by K* exchange and is subject only to parity conservation constraints, while the second is dominated by Pomeron and exchange and is subject to both parity conservation and time reversal invariance. In addition, the nature of the mechanism which is responsible for the polarization in inclusive production probably differs from that in elastic scattering because of the regions probed in the two interactions. If we take $\hbar c/p_t$ to be a naive measure of the impact parameter b in the two reactions, we see that, for

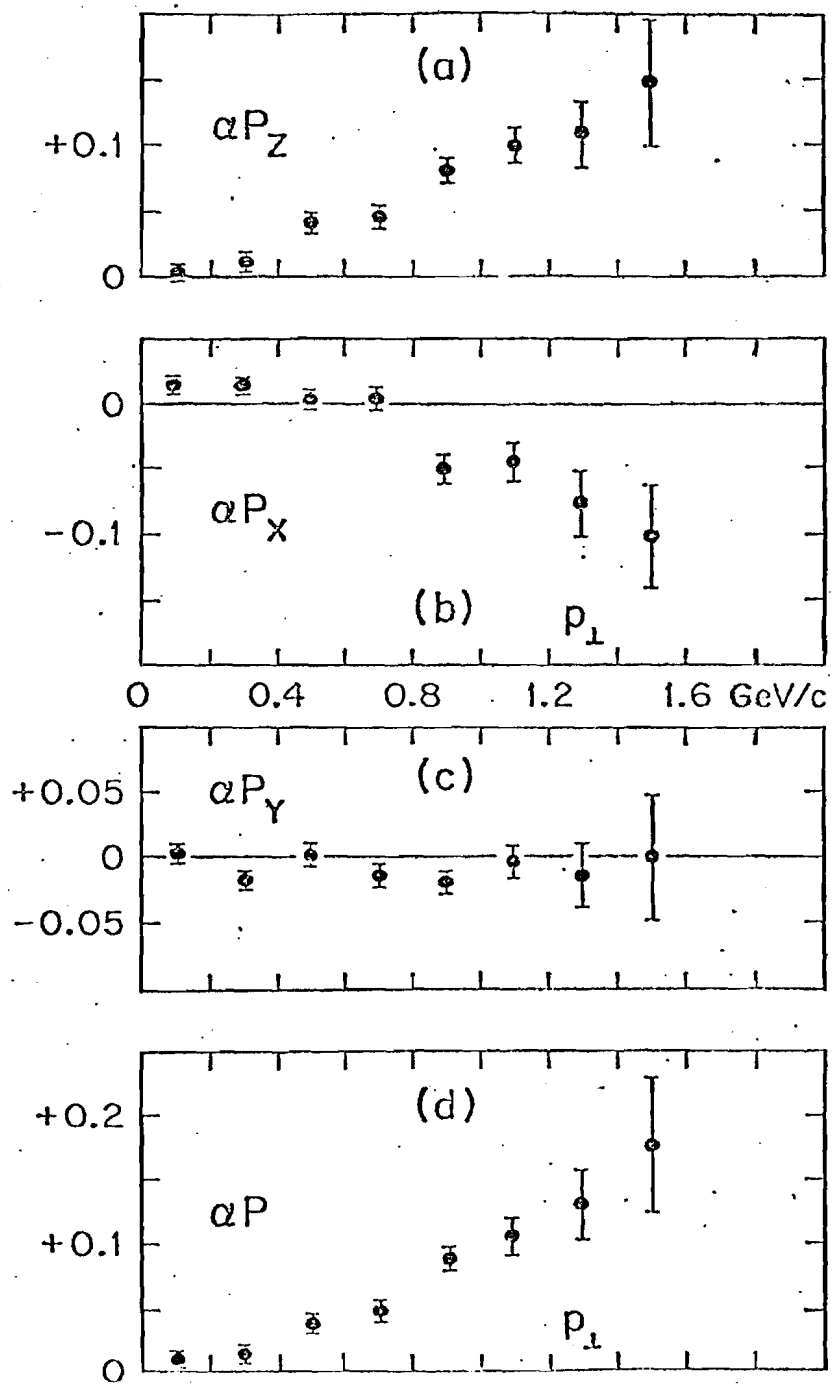

Fig. 6.2

elastic scattering with $|t| \approx .2$ $(\mathrm{GeV/c})^2$, $b \approx 0.5$ fermi. Thus the interaction tends to be somewhat peripheral. In inclusive production, however, substantial polarizations occur only at much larger values of p_t, leading to values of $b \approx 0.1$ fermi. In addition, a strange quark appears in the final state which was not present initially. This suggests that this polarization arises from some type of constituent interaction. Still, the fact that both reactions exhibit nonzero polarizations of the Λ in the final state, suggests very strongly that spin dependent forces are important at energies much higher than other evidence of scaling behavior seems to suggest.

APPENDIX A

REASONS FOR EVENT REJECTION

A.1 REJECTION BY THE TRACK RECONSTRUCTION PROGRAM

The input to this stage of the analysis was the raw data tapes. Potential events could be rejected by the track reconstruction program for reasons listed below. Parenthesized numbers show the percent of events eliminated by each cut for a typical data tape. Each test assumes that all preceding tests were passed by the event.

1. No wire hits for the event (0.4%).

2. The on-line program's event buffer had overflowed. Occasionally so many wires were hit in one event that the storage space alotted to wire hits by the on-line monitor program was filled before all of the information for that event could be read out (0.01%).

3. Chamber number out of range. This happened when the event claimed to have wire hits in a nonexistent chamber (0.0%).

4. No detectable bend in M2 of one or both tracks. This implied infinite momentum (0.0%).

5. Both tracks bent the same direction by M2 (0.4%).

6. Too many points in one chamber plane. A maximum of 8 wire hits from any chamber plane was processed on any event (0.0%).

7. No visible opening angle. If the two tracks coincided in both views upstream of M2, the event was rejected (26%).

8. Two y planes of C5, C10, C11, C12 have no hits (17%).

9. More than two possible tracks in the y-view (7.6%).

10. No two y plane readings in C5, C10, C11, C12 have exactly two hits each (10.5%).

11. Can't find two tracks with 3 points each on them in the y-view (3.8%).

12. Only one track in the y-view and only one point in C7 (the U-V chamber) (4.8%).

13. Only one point on a track upstream of M2 in the x-view (1.7%).

14. Can't find two tracks downstream of M2 in the x-view (3.3%).

15. Can't match the two tracks in the two views (0.4%).

16. Tracks do not point to a common vertex (<0.1%).

17. Bad chi-squared for track straightness and skewness fit (0.1%).

A.2 REJECTION BY THE ELASTIC SCATTERING PROGRAM

Input for this stage of the analysis was data tapes containing events which passed all cuts in the first stage of the analysis. Potential events could be rejected by the elastic scattering reconstruction program for reasons which follow. Parenthesized numbers give the number of events cut in a typical data tape. Each test assumes that the event passed all previous tests.

1. Improper hit topology in the recoil arms (discussed in section 4.2) (35%).

2. Improper target or collimator pointing of the reconstructed incident particle (35%).

3. Negative z component of the recoil proton momentum. No kinematically allowed lambda-p elastic scatter could result in an angle between the lambda and proton tracks of greater than 90 degrees in the lab (<0.5%).

4. Recoil proton track fails to intersect the hydrogen target (and thus the neutral beam).

5. Recoil proton track fails to intersect the track of the scattered particle. (This was decided using a chi-squared test.) (5%; includes preceding test)

6. Scattered particle decay vertex not within the decay volume (1.5%).

A.3 REJECTION BY THE POLARIZATION PROGRAM

Input for this stage of the analysis was events passed by the first two stages of the analysis. Elastic scattering events could be rejected by the polarization program for a number of reasons. Most of these reasons arose from the cuts made on the data by the acceptance program (described in section 4.3) as a result of the fact that the allowed fiducial volumes were made slightly smaller than the real experimental apertures. Event rejection occured for reasons which follow. Parenthesized numbers give the number of events cut. Each test assumes that the event passed all

preceding tests.

1. Tracks too close together in C5 (see section 4.4).

2. Tracks too close together in C10 (see section 4.4) (28%; includes preceding test).

3. A particle missed C5 (0.0%).

4. A particle missed C7 (0.01%).

5. A particle missed C10 (0.08%).

6. A particle fails to pass through the aperture of M2. This was checked at the bending plane, midway through M2, and at the downstream face of M2 (1.2%).

7. A particle missed C11 (0.5%).

8. A particle missed C12 (0.3%).

9. Both particles missed C13 (1.7%).

The following reasons for event rejection were consistency checks:

10. Momentum of the incident particle is larger than the momentum of the incident proton beam (0.0%).

11. Unphysical value of t for the scatter (0.0%).

APPENDIX B

THE MAXIMUM LIKELIHOOD METHOD

The likelihood that the lambda decay i is part of a polarized distribution relative to the direction s is

$$L_i(P) = (1 + \alpha P \cos[\theta_i^*]) / \int_{acc} (1 + \alpha P \cos[\theta^*]) d \cos \theta^*$$

where $\cos \theta_i^* = \hat{p}_i \cdot \hat{s}$, $\hat{p}_i$ is the decay proton direction in the lamoda rest frame, and $\int_{acc}$ is the integral over the acceptance region in $\cos \theta^*$ for each event. The likelihood function for the set of events [i] is $L(P) = \prod_i L_i(P)$ or $\ln[L(P)] = \sum_i \ln[L_i(P)]$, and the most probable polarization occurs when L(P) is maximum.

In order to find the acceptance region in $\cos \theta^*$ for each event, the program generated a series of fake events identical to the accepted real event except that they were assigned new values of $\cos \theta^*$ at intervals of 0.1 covering the entire interval -1. to +1. These fake events were run through the same acceptance program that examined the real event. Edges in the acceptance for the event were found by interpolation to ± 0.002 in $\cos \theta^*$.

Using these measured acceptance edges, the integral over the acceptance for each event was calculated and stored in a convenient expansion, avoiding the necessity of generating a large table of L(P) for different P. This was done in the following manner:

$$\text{Define} \quad A_i = \int_{acc_i} d \cos \theta^*$$

$$B_i = \int_{acc_i} \cos \theta^* \, d \cos \theta^*$$

$$C_i = B_i / A_i$$

$$\text{Then } \ln[L(P)] = \sum_i \ln[(1 + \alpha P \cos \theta^*)/(A_i + \alpha P B_i)]$$

$$= \sum_i [\ln[(1 + \alpha P \cos \theta^*)/(1 + \alpha P C_i)] - \ln A_i]$$

$$= \sum_i [\ln(1 + \alpha P \cos \theta^*) - \ln(1 + \alpha P C_i)] - \sum_i \ln A_i$$

Using the expansion

$$\ln(1 + x) = x - 1/2\, x^2 + 1/3\, x^3 - 1/4\, x^4 + \ldots$$

we see that

$$\ln[L(P)] = S_\emptyset + \sum_{I=0}^{\infty} (-\alpha P)^I S(I)/I$$

where

$$S_\emptyset = -\sum_i \ln A_i = \text{constant}$$

and

$$S(I) = \sum_i ([\cos \theta^*]^I - C_i^I).$$

The program used the acceptance region that it calculated for each event and cos θ^* for each real event to generate the first eight of the constants S(I) for each event. As the real events were processed, the program simply kept track of the sums of the values for these S(I). This gave ln[L(P)] when all of the events had been processed. The program maximized ln[L(P))] by finding the value of P for which the derivative of ln[L(P)] was zero

using Newton's Method. The errors in P were determined by finding the values of P where

$$\ln[L(P)] = \ln[L_{max}] - 1/2.$$

APPENDIX C

THE MINIMUM CHI-SQUARED METHOD

The first step in the chi-squared method was to generate fake events identical to the accepted real event except having new values of cos θ^* generated randomly over the interval -1 to +1. A series of these events was processed by the acceptance program which examined the real events until ten were accepted. This resulted in a sample of ten fake events with values of cos θ^* generated randomly over the acceptance region in cos θ^* for each corresponding real event. The resulting distribution of fake events was then parametrized as a function of the polarization P to avoid the necessity of generating a large table of Monte Carlo event distributions for different P. This resulted in a function which could be used, together with the distribution of real events, to generate a chi-squared as a function of P which was given by the following:

$$\chi^2(P) = \sum_I [N_{real}(I) - N_{mc}(I,P)]^2/N_{real}(I)$$

where I is a bin in cos θ^*.

The generated distribution of Monte Carlo events was parametrized in the following manner:

A Monte Carlo distribution is generated based on the real events. The distribution of the real events can be written

$$dN(\cos\theta^*,x)=A(\cos\theta^*,x)(1+\alpha P\cos\theta^*)d\cos\theta^*$$

where x represents parameters of the event (phi*, vertex position, momentum) other than $\cos\theta^*$. $A(\cos\theta^*,x)$ is the acceptance and $(1+\alpha P\cos\theta^*)$ is the physics polarization factor. If for each event we generate a Monte Carlo event with the same parameters x, but with a new $\cos\theta^*$, we can obtain the same distribution for the Monte Carlo as for the real events if we weight the Monte Carlo event properly. If we assign the Monte Carlo event the weight W, then

$$dN_{mc}(\cos\theta^*,x) = dN_{real}(\cos\theta^*,x)\ W$$

and we want $dN_{mc} = dN_{real}$, so

$$W= [A(\cos\theta^*,x)(1+\alpha P\cos\theta^*_{mc})d\cos\theta^*]/$$
$$[A(\cos\theta^*,x)(1+\alpha P\cos\theta^*_{real})d\cos\theta^*]$$

or

$$W = (1+\alpha P\cos\theta^*_{mc})/(1+\alpha P\cos\theta^*_{real})$$

Thus we generate a Monte Carlo which tests <u>only</u> the $\cos\theta^*$ distribution and uses the real event distribution to provide the acceptance and the distribution in other non-essential parameters. The weight W corresponds to the fact that we started with a distribution biased in $\cos\theta^*$ by physics (the polarization).

For each real event the polarization program generated <u>ten</u> events at random over the cos θ^* acceptance region, retaining the other parameters of the event. These "Monte Carlo" events were then binned in cos θ^* and were weighted by W. The weighting function W was determined in the following manner:

$$W_{i,mc} = (1 + \alpha P \cos \theta^*_{mc})/(1 + \alpha P \cos \theta^*_i)$$

where i is the real event index and mc is the index for the Monte Carlo events corresponding to each real event. This can be expanded as follows:

$$W_{i,mc} = (1 + \alpha P \cos \theta^*_{mc})[1 - \alpha P \cos \theta^*_i + (\alpha P \cos \theta^*_i)^2 - (\alpha P \cos \theta^*_i)^3 + \ldots]$$

$$= 1 + \alpha P(\cos \theta^*_{mc} - \cos \theta^*_i) - (\alpha P)^2 \cos \theta^*_i (\cos \theta^*_{mc} - \cos \theta^*_i) + (\alpha P)^3 [\cos \theta^*_i]^2 (\cos \theta^*_{mc} - \cos \theta^*_i) - \ldots$$

If we define, for each bin I in cos θ^*,

$$C1(I) = \sum_i \left(\sum_{mc} 1 \right)$$

$$C2(I) = \sum_i \left(\sum_{mc} [\cos \theta^*_{mc} - \cos \theta^*_i] \right)$$

$$C3(I) = \sum_i \left(\sum_{mc} \cos \theta^*_i [\cos \theta^*_{mc} - \cos \theta^*_i] \right)$$

$$C4(I) = \sum_i \left(\sum_{mc} (\cos \theta^*_i)^2 [\cos \theta^*_{mc} - \cos \theta^*_i] \right)$$

where the sum in each bin I is over the Monte Carlo events falling in that bin, we see that

$$W(I,P) = C1(I) + C2(I)\alpha P - C3(I)(\alpha P)^2 + C4(I)(\alpha P)^3$$

Thus the weight to apply to the Monte Carlo events falling into each bin I of the cos θ^*_{mc} distribution is calculated

as a function of P merely by keeping running totals in each $\cos \theta^*_{mc}$ bin of the appropriate constants C1, C2, C3, and C4. This allows us to generate a Monte Carlo distribution of events as a function of P: $N'_{mc}(I,P)$. If we normalize $N'(I,P)$ so that the total number of events is the same as the total number of real events we obtain $N_{mc}(I,P)$, but this normalization is trivial:

$$N_{mc}(I,P) = 1/10\ N'_{mc}(I,P).$$

From this we obtain $\chi^2(P)$ from the following:

$$\chi^2(P) = \sum_I (N_{real}(I) - N_{mc}(I,P))^2/N_{real}(I)$$

and, since N_{mc} is a function of the polarization via the weights W, the polarization can be determined by minimizing chi-squared. This was done by finding the point at which the derivative of chi-squared with respect to P was equal to zero using Newton's Method. The polarization error is the change in the polarization to have

$$\chi^2 = \chi^2_{min} + 1.$$

FOOTNOTES AND REFERENCES

1. Landolt-Börnstein Compilations, Numerical Data and Functional Relationships in Science and Technology, Group 1, Volume 7, (1973).

2. This is essentially Table 0.1.1 from ref. 1.

3. See, for instance
C. Bourrely, Nuclear Physics, B77 (1974) 386-396.
or ref. 4.

4. J. Soffer, Phys. Letters, 43B (1973) 514-516.

5. L. Wolfenstein, Phys. Rev., 85 (1952) 947.

6. L. Wolfenstein, Ann. Rev. Nucl. Phys., 6 (1956) 43.

7. M. Jacob and G. C. Wick, Ann. Phys., 7 (1959) 404.

8. For a convenient survey of properties of the $d^J_{\mu\lambda}(\theta)$ see Appendix A of
A. D. Martin and T. D. Spearman, Elementary Particle Theory, North-Holland Publ., (1970).

9. J. T. Donohue, Talk Presented at the Argonne 1974 Summer Study on HEP with Polarized Beams, ANL/HEP 75-02.

10. More general relations between the Wolfenstein and helicity formalisms are given in the following: Suh Urk Chung, Spin Formalisms, Lectures Given at the Academic Training Programme of CERN 1969, 1970, CERN 71-8.

11. M. Davier, Proc. Inst. on Part. Phys. at SLAC, SLAC-179 Vol. 1 (1974) 187-288.

12. J. P. Ader, C. Meyers, Ph. Salin, Nucl. Phys., B82 (1974) 237.

13. G. L. Kane and A. Seidl, Rev. Mod. Phys., 48 (1976) 309.

14. G. C. Fox and C. Quigg, Ann. Rev. Nuc. Sci., 23 (1973) 219.

15. J. Soffer and D. Wray, Talk Presented at Argonne 1974 Summer Study on HEP with Polarized Beams, ANL/HEP 75-02.

16. See, for instance S. Gasiorowicz, Elementary Particle Physics, John Wiley and Sons, 1966, page 94.

17. M. L. Goldberger and K. M. Watson, Collision Theory, John Wiley and Sons, 1966.

18. If we designate the normalized number of events observed with the beam and target spins in the four orientations up-up, up-down, down-up, and down-down by $N_{\uparrow\uparrow}$, $N_{\uparrow\downarrow}$, $N_{\downarrow\uparrow}$, and $N_{\downarrow\downarrow}$ respectively then
$C_{nn} = [N_{\uparrow\uparrow} - N_{\uparrow\downarrow} - N_{\downarrow\uparrow} + N_{\downarrow\downarrow}]/[P_B P_T \ N_{ij}]$
where P_B and P_T are the beam and target polarizations. If the interaction is oblivious to the relative orientation of the initial spins, then $C_{nn} = 0$. See also Ref. 19.

19. H. A. Neal, "Recent Dev. in the Study of Spin Effects in Nucleon-Nucleon Interactions at High Energies", AIP Symposium on HEP with Polarized Beams and Targets, Argonne, August 23-27, 1976.

20. H. Harari, Phys. Rev. Lett., 26 (1971), 1400.

21. M. Ross, F. S. Henyey, G. L. Kane, Nucl. Phys., B23 (1970) 269.

22. D. P. Roy, High Energy Phenomenology, ed. J. Tran Than Van, Paris (1971) 309.

23. All hyperon data referred to in this section except for reference 24 is bubble chamber data.

24. S. Gjesdal, G. Presser, P. Steffen, J. Steinberger, F. Vannucci, H. Wahl, K. Kleinknecht, V. Luth, G. Zech, Phys. Lett, 40B (1972) 152.

25. D. Bassano, C. Y. Chang, M. Goldberg, T. Kikuchi, J. Leitner, Phys. Rev., 160 (1967) 1239.

26. G. R. Charlton, J. Badier, E. Barrelet, J. R. Hubbard, A. Leveque, C. Lovedec, I. Makarovisch, L. Moscoso, J. Pernegr, D. Revel, Phys. Lett., 32B (1970) 720.

27. K. J. Anderson, N. M. Gelfand, J. Keren, T. H. Tan, Phys. Rev., D11 (1975) 473.

28. G. Alexander, O. Benary, U. Karshon, U. Maor, Nucl. Phys., B10 (1969) 554.

29. If we write the transition matrix for hyperon decay as

$$M = s + p\,(\vec{\sigma} \cdot \hat{p})$$

where s and p are the parity changing and the parity conserving amplitudes, respectively, $\vec{\sigma}$ is the Pauli spin operator, and $\hat{p}$ is a unit vector in the direction of the decay baryon in the hyperon rest frame; then α is defined by

$$\alpha = 2\,\mathrm{Re}(s^*p)/(|s|^2 + |p|^2).$$

30. G. Giacomelli, Phys. Reports, 23 (1976) 123.

31. Preliminary results for pp polarization at NAL energies give a polarization at $|t| = +.3\,(\mathrm{GeV/c})^2$ consistent with zero with errors of a few percent.

32. J. Pumplin and G. L. Kane, Phys. Rev., D11 (1975) 1183.

33. C. B. Chiu, Ann. Rev. Nuc. Sci., 22 (1972) 255.

34. P. Skubic, PhD. Thesis, University of Michigan (to be published).

35. R. A. Fisher, Statistical Methods for Research Workers, 14th edition, Hafner Publishing Co. (1970).

36. A. Gaidot et al (29 authors), Phys. Lett., 57B (1975) 389.

37. A. Gaidot et al (29 authors), Phys, Lett, 61B (1976) 103.

38. R. M. Delaney and J. L. Gammel, Talk Presented at ANL Summer Study on HEP with Polarized Beams, ANL/HEP 75-02.

39. J. D. Jackson, Rev. Mod. Phys. 42 (1970) 12.

40. G. Bunce, T. Devlin, B. Edelman, R. T. Edwards, R. Handler, K. Heller, R. March, P. Martin, J. Norem, O. Overseth, L. Pondrom, L. Schachinger, M. Sheaff, P. Skubic, P. Yamin, Phys. Rev. Lett., 36 (1976) 1113.

41. A more detailed description of components (1), (2), (4), (6), and (7) may be found in Ref. (34).

42. A. Kotanski, Acta Physica Polonica, 30 (1966) 629.

43. See, for instance
A. Bialas, B. E. Y. Svenson, CERN Preprint TH633 (1965).

44. Note that the sign of P_z depends upon the polarity of M1.

45. P. Martin, PhD. Thesis, University of Wisconsin (to be published).

46. For pp scattering $f_5=-f_6$ and these formulas reduce to formulas given in Reference 9.

47. This formula appears also in Reference 13, except that they use $\aleph_5=f_{-+++}$. In our notation $f_6=-\aleph_5$.

48. O. Overseth and R. Roth, Phys. Rev. Lett. 19 (1967) 391.

Brian Scott Edelman

1951	Born September 2 in Decatur, Illinois.
1968	Graduated from Shasta Union High School, Redding, California.
1972	B.S. in Physics/Mathematics, University of Nevada, Reno, Nevada.
1975	M.S. in Physics, Rutgers University, New Brunswick, New Jersey.
1977	Ph. D. in Physics.